EINDHOVEN UNIVERSITY OF TECHNOLOGY

Solid state electrolytes for all-solid-state 3D lithium-ion batteries

Citation for published version (APA):
Kokal, I. (2012). *Solid state electrolytes for all-solid-state 3D lithium-ion batteries*. [Phd Thesis 1 (Research TU/e / Graduation TU/e), Chemical Engineering and Chemistry]. Technische Universiteit Eindhoven. https://doi.org/10.6100/IR738959

DOI:
10.6100/IR738959

Document status and date:
Published: 01/01/2012

Document Version:
Publisher's PDF, also known as Version of Record (includes final page, issue and volume numbers)

Please check the document version of this publication:

• A submitted manuscript is the version of the article upon submission and before peer-review. There can be important differences between the submitted version and the official published version of record. People interested in the research are advised to contact the author for the final version of the publication, or visit the DOI to the publisher's website.
• The final author version and the galley proof are versions of the publication after peer review.
• The final published version features the final layout of the paper including the volume, issue and page numbers.

Link to publication

General rights
Copyright and moral rights for the publications made accessible in the public portal are retained by the authors and/or other copyright owners and it is a condition of accessing publications that users recognise and abide by the legal requirements associated with these rights.

• Users may download and print one copy of any publication from the public portal for the purpose of private study or research.
• You may not further distribute the material or use it for any profit-making activity or commercial gain
• You may freely distribute the URL identifying the publication in the public portal.

If the publication is distributed under the terms of Article 25fa of the Dutch Copyright Act, indicated by the "Taverne" license above, please follow below link for the End User Agreement:

www.tue.nl/taverne

Take down policy
If you believe that this document breaches copyright please contact us at:

openaccess@tue.nl

providing details and we will investigate your claim.

Download date: 04. Oct. 2023

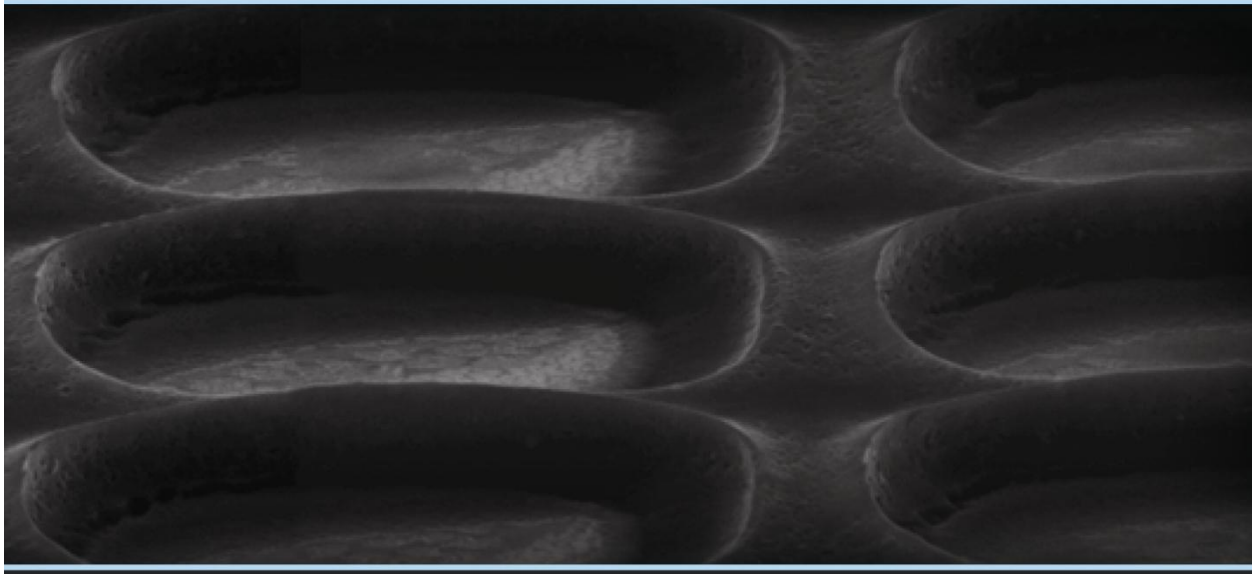

Solid State Electrolytes for All-Solid-State 3D Lithium-ion Batteries

Ilkin Kokal

Solid State Electrolytes for All-Solid-State 3D Lithium-ion Batteries

PROEFSCHRIFT

ter verkrijging van de graad van doctor aan de
Technische Universiteit Eindhoven, op gezag van de
rector magnificus, prof.dr.ir. C.J. van Duijn, voor een
commissie aangewezen door het College voor
Promoties in het openbaar te verdedigen
op dinsdag 6 november 2012 om 16.00 uur

door

Ilkin Kokal

geboren te Balıkesir, Turkije

Dit proefschrift is goedgekeurd door de promotor:

prof.dr. P.H.L. Notten

Copromotor:

dr. H.T.J.M. Hintzen

A catalogue record is available from the Eindhoven University of Technology Library

ISBN:978-90-386-3270-4

Cover design by Atike Dicle Pekel Duhbaci, Atike Design, Eindhoven
Printing: TU/e Printservice

This work has been carried out within STW Project Nr: 07796 "Second Generation of Integrated Batteries"

Enabling new technology

To mum and dad,

To Idil,

To my lovely Tuba…

Table of Contents

1. Introduction

1.1 Batteries 1

1.2 Lithium-ion batteries 3

1.3 All-solid-solid-state lithium-ion batteries 5

1.4 Scope of this thesis 6

1.5 References 8

2. Solid Lithium Ion conductors: Review

2.1 Introduction 10

2.2 Perovskite-type lithium-ion conductors 11

2.3 Garnet-type lithium-ion conductors 17

2.4 NASICON-related lithium-ion conductors 21

2.5 LISICON-type and thio-LISICON lithium-ion conductors 24

2.6 LiPON and related systems 26

2.7 Summary 28

2.8 References 30

3. $Li_{0.5}La_{0.5}Ti_3O_xN_y\square_{3-(x+y)}$: Synthesis, Structure and Lithium-Ion conductivity Properties

3.1 Introduction 36

3.2 Experimental method 36

3.3 Results and discussion 38

3.4 Conclusions 44

3.5 References 46

4. Sol-Gel Synthesis and Lithium Ion Conductivity of $Li_7La_3Zr_2O_{12}$ with Garnet-related Type Structure

4.1 Introduction 48

4.2 Experimental method 49

4.3 Results and discussion 50

4.4 Conclusions 59

4.5 References 60

5. Sol-Gel Synthesis and Lithium Ion Conduction Properties of $Li_5La_3Ta_2O_{12}$ and $Li_5BaLa_2Ta_2O_{12}$
5.1 Introduction 62
5.2 Experimental method 63
5.3 Results and discussion 64
5.4 Conclusions 72
5.5 References 74
6. Preparation and Characterization of 3D Ordered Macroporous $Li_5La_3Ta_2O_{12}$ by Colloidal Crystal Templating for All-Solid-State Lithium-ion Batteries
6.1 Introduction 78
6.2 Experimental method 79
6.3 Results and discussion 81
6.4 Conclusions 86
6.5 References 88
7. 3D Patterning of Lithium Lanthanum Titanium Oxide by Soft Lithography
7.1 Introduction 90
7.2 Experimental method 91
7.3 Results and discussion 93
7.4 Conclusions 103
7.5 References 105

Summary 107
Curriculum Vitae 112
List of publications 113
Acknowledgements 114

Chapter 1.

Introduction

1.1. Batteries

Portable devices have been widely used since the discovery of electricity as energy carrier and batteries are considered as the most promising power supply for portable applications so far. Batteries can store electricity in the form of chemical energy. The electrochemical energy is created by electrochemical reduction and oxidation reactions, taking place at individual electrodes in the battery. Batteries are composed of several electrochemical cells that are connected in series and/or parallel to deliver the necessary voltage and capacity. There are two types of batteries: primary and secondary batteries. In primary batteries, the chemical energy cannot be restored once it has been converted to electrical energy, while in secondary batteries, the electrochemical processes are reversible. Secondary batteries are being recharged by an external electrical energy source.

The building blocks of a rechargeable battery are the positive electrode, negative electrode, electrolyte and current collectors. The positive and negative electrodes are internally connected via an ionically conductive material called electrolyte and externally to current collectors. Several battery types were investigated so far and a few of them are commercially available. Figure 1.1 shows a comparison of the various rechargeable batteries with other commercially available rechargeable cells in terms of volumetric and gravimetric energy densities. Today, the lead-acid batteries are being used in almost every vehicle because of their high power and low cost, but energy density is relatively low due to its heavy weight and large volume. For low power electronic devices, Ni-Cd batteries are most suitable. But nowadays, they are being replaced with more environmental friendly Ni-M-H batteries which exhibit a cell voltage of 1.2 V. The lithium cells exhibit a cell voltage of 2.5-4.2 V depending on the choice of the electrode materials. As shown in figure 1.1, lithium ion batteries in various existing battery technologies are supplying the highest energy density which is the

amount of the energy scaled to its mass or volume. In addition to their high energy density, lithium ion batteries are offering flexible light weight design and longer cycle life than comparable battery technologies. This explains why they are receiving much attention from a both fundamental and applied point of view.

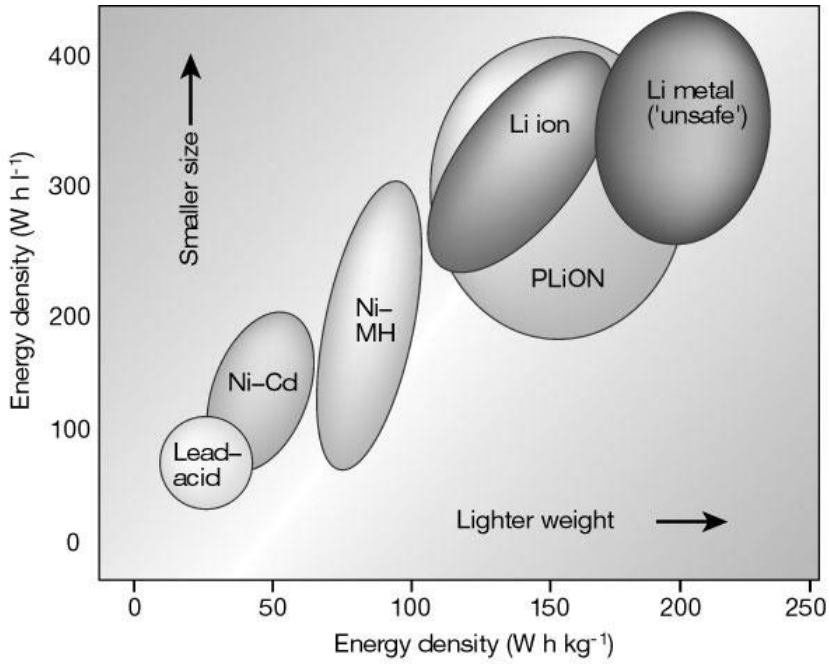

Figure 1.1. Energy density per unit of mass and volume plotted for various rechargeable battery types [1].

1.2. Lithium-ion batteries

The usage of rechargeable Li-ion batteries is rapidly expanding in every part of our daily life. They are intensively being used in large scale mobile applications, such as hybrid cars and also portable applications, such as mobile phones, notebooks, tablet PCs. The conventional lithium ion batteries are composed of carbon-based negative electrode, a lithiated transition metal oxide positive electrode and a separator which is an electrolyte containing dissociated lithium salt in an organic liquids. The Electrolyte enables lithium ion transfer between the two electrodes. The mechanism for electricity

storage in lithium ion batteries is based on the transport of lithium between the cathode and anode, and vice versa. A typical example of a lithium-ion battery with a $LiCoO_2$ positive electrode and graphite negative electrode is shown in Figure 1.. This battery is operating by the following reversible electrochemical reactions:

$$LiCoO_2 \underset{\text{Discharge}}{\overset{\text{Charge}}{\rightleftharpoons}} Li_{1-n}CoO_2 + n\,Li^+ + n\,e^- \qquad \textbf{1.1}$$

$$n\,Li^+ + n\,e^- + C_6 \underset{\text{Discharge}}{\overset{\text{Charge}}{\rightleftharpoons}} Li_nC_6 \qquad \textbf{1.2}$$

this results in an overall reaction of

$$LiCoO_2 + C_6 \underset{\text{Discharge}}{\overset{\text{Charge}}{\rightleftharpoons}} Li_nC_6 + Li_{1-n}CoO_2 \qquad \textbf{1.3}$$

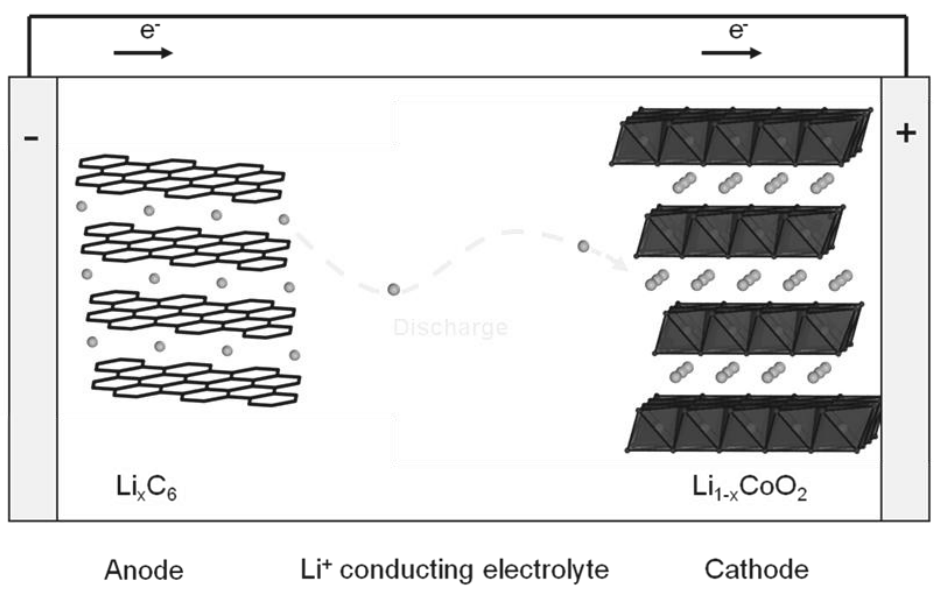

Figure 1.2. Schematic representation of Li-ion electrochemical cell under operating (discharging) conditions. When charging this battery all process will take place in reverse direction.

Lithium ion batteries are predominantly used among the various existing battery technologies due to their high energy density. However, the conventional rechargeable batteries contain hazardous and flammable organic liquid electrolytes, making them potentially unsafe [2]. For this reason, replacement of the liquid electrolyte with a safer and stable solid electrolyte is necessary to improve the safety by preventing the risk of liquid electrolyte leakage and improving the thermal stability and cycle life. Research efforts are directed toward finding suitable solid electrolytes for lithium ion batteries with high lithium ion conductivity as well as high electrochemical stability with commonly used intercalation materials for battery applications.

1.3. All-solid-state lithium-ion batteries

Solid-state lithium ion batteries have been extensively studied in the previous decades. They supply significant advantages with minor disadvantages compared to those using liquid electrolytes such as resistance to shocks and vibrations, absence of self-discharge, better cycle life and possibility for miniaturization and integration. However, solid electrolytes are bringing some disadvantages such as the fact that the ionic conductivity of the currently available solid electrolytes is usually significantly lower than that of the liquid electrolytes, and they have poor contact with the solid electrodes. Those issues are resulting in a high internal resistance of the electrochemical cell which causes a high voltage drop and, consequently low current densities of solid-state batteries. The problems with the high internal resistance can be reduced by using an electrolyte in the form of a thin film [3]. This was the first reason for the use of thin film techniques in battery technology, yet it needs sophisticated fabrication steps. Another promising approach is to design and integrate the battery materials in a 3D configuration, it can be employed not only to enlarge the contact area between the solid electrolyte and electrode materials but also to increase the volumetric energy density. Significant increase in the interfacial area between the electrode and electrolyte can be achieved by

3D configuration which may reduce the interfacial kinetic overpotential and the distance that ions have to be transported [4]. So far, some of the 3D structures such as the honeycomb type, integrated array structure and 3-dimensionally ordered macraporous structure (3DOM) [5-8] have been proposed and reported to overcome the interfacial problem between the electrode and electrolyte.

1.4. Scope of this thesis

This thesis is mainly focusing on the various aspects of novel synthesis, characterization and ionic conductivity properties of well-known high lithium ion conductors with perovskite ($Li_{3x}La_{0.66-x}TiO_3$) and garnet ($Li_{5+x}La_3M_2O_{12}$ (M=Ta(x=0), Zr(x=2)) type of structures to prepare state-of-the-art solid electrolyte materials for 3-dimensional Li-ion batteries. Novel synthesis methods (sol-gel synthesis) and new compounds (new perovskite-type oxynitrides) were investigated and reported where some of those were found promising candidates for new types of 3D all-solid-state batteries due to suitable synthesis conditions with adequate properties. Investigations of those compounds enable us to design novel electrolyte systems with three dimensionally ordered structures by colloidal crystal templating and micro-molding with the intention to enhance the performance of the all-solid-state batteries by increasing the interfacial area between solid electrolyte and solid electrode to minimize the internal resistance. All of the above mentioned topics have important contributions on better understanding of the design and preparation of 3D integrated all-solid-state lithium ion batteries by crystal templating or micro-molding.

Chapter 2 will give a review of reported studies on solid lithium ion conductor materials to provide detailed information in this field. In this review, potential solid electrolyte materials for lithium ion batteries will be highlighted and the structure property relationship will be discussed in detail.

Chapter 3 describes the synthesis and characterization of new perovskite-type oxynitride solid solutions of $Li_{0.5}La_{0.5}TiO_xN_y$ by thermal ammonolysis of oxide precursor starting with both sol-gel and solid-state prepared precursors. The systematic investigation on the influence of nitrogen incorporation on the lithium ion conductivity measured by AC impedance spectroscopy is reported.

Chapter 4 explains the sol-gel synthesis and lithium ion conductivity of $Li_7La_3Zr_2O_{12}$ with garnet -related type structure. Our research revealed a novel low temperature cubic garnet-related phase in the Li-La-Zr-O system and we have reported the ionic conductivity of $Li_7La_3Zr_2O_{12}$ with tetragonal garnet-related phase.

Chapter 5 studies the sol-gel synthesis and lithium ion conductivity of $Li_5La_3Ta_2O_{12}$ (LLTO) and $Li_6BaLa_2Ta_2O_{12}$ (LLBTO) with garnet-type structure. The electrochemical properties of the above mentioned compounds were tested by AC impedance spectroscopy.

Chapter 6 describes the preparation of 3 dimensionally ordered macro-porous (3DOM) garnet $Li_5La_3Ta_2O_{12}$ (LLTO) structures by colloidal crystal templating. The effect of precursor solution and the Polystyrene (PS) spheres used for the template preparation on the morphology macro-porous electrolyte membrane is discussed.

Chapter 7 reports the investigations of nano-structured patterned thin films of $Li_{0.35}La_{0.55}TiO_3$ which were fabricated by micro-molding the sol-gel precursor solution with a relief-patterned polymer mould on a Si substrate. The patterns solidified before removing the mould and the solidified patterned precursor film was pyrolized at 973 K for 30 minutes in air atmosphere. The phase and elemental composition as well as morphology of the LLT patterns were determined by XRD, SEM – EDAX and AFM measurements.

A concluding summary will give an overview of the main results as well as some suggestions and discussions for continuation of this research project.

1.5. References

[1] J.M. Tarascon, M.Armandi, Nature **2001**, 33, 411.

[2] L. Baggetto, R.A.H. Niessen, F. Roozeboom, P.H.L. Notten, Adv. Funct. Mater. **2008**, 18, 1057.

[3] A. Levasseur, M. Menetrier, R. Dormoy, G. Meunier, Mater. Sci. Eng. B, **1989**, 3, 5.

[4] J.W. Long, B. Dunn, D.R. Rolison and H.S. White, Chem. Rev. **2004**, 104, 4463.

[5] M. Kotobuku, Y. Suzuki, H. Munakata, K. Kanamura, Y. Sato, K. Yamamoto, T. Yoshida, J. Electrochem. Soc. **2010**, 157, A493.

[6] M. Kotobuki, T. Sugiura, J. Sugaya, H. Munakata, K. Kanamura, Electrochemistry **2010**, 78, 273.

[7] K. Kanamura, N. Akutagawa, K. Dokko, J. Power Sources **2005**, 146, 86.

[8] P.H.L. Notten, F. Roozeboom, R.A.H. Niessen, L. Baggetto, Adv. Mater. **2007**, 19, 4564.

Chapter 2.

Solid Lithium Ion Conductors: Review

Abstract

A wide range of lithium ion conductors are summarized and the structure and composition relationship will be discussed in this review chapter. Several crystal systems are highlighted with their advantages and drawbacks in terms of lithium ion conduction properties and some of them are recommended as being of particular interest.

2.1. Introduction

The conventional rechargeable batteries supply high energy and power densities in various electronic devices. However, they contain hazardous and flammable organic liquid electrolytes, making them potentially unsafe [1-3]. Unlike liquid electrolytes, the use of solid electrolytes in a next generation lithium ion batteries may provide numerous advantages, such as preventing electrolyte leakage, improving thermal and mechanical stability, no self discharge, and longer cycle life as well as the possibility of miniaturization and integration. Thus, the development of new solid inorganic electrolytes for application in all-solid-state lithium ion batteries is currently one of the key issues in this technology [4,5]. The past few decades, research efforts are directed towards finding suitable solid electrolytes for lithium ion batteries with high lithium ion conductivity as well as high electrochemical stability in contact with commonly used intercalation electrode materials for battery applications [6].

Solid-state lithium ion conductors have been under intense investigation focusing on a wide range of chemical compositions and crystal structures, such as Li_4SiO_4, Li_2SO_4, $Li_{14}ZnGe_4O_{16}$ (NASICON), $Li_{1+x}Ti_{2-x}M_x(PO_4)_3$ (LISICON) (M = Al, Sc, Y, La), Li–β–alumina, perovskite-type $Li_{0.34}La_{0.5}TiO_{2.98}$ and garnet-related $Li_5La_3M_2O_{12}$ (M = Ta, Nb), $Li_{10}GeP_2S_{12}$. Figure 2.1 shows an Arrhenius plot of the ionic conductivities of the most important lithium solid electrolytes. Some of the reported ionic conductivities are in between 10^{-2} and 10^{-7} S/cm at room temperature [7-18]. In this review chapter, we present an overview in the current state-of-the-art knowledge of inorganic solid lithium ion conductors by focusing on the relationship between the structure and materials properties in order to better understand the lithium ion mobility in inorganic solids. Moreover, the advantages and drawbacks of the discussed compounds are highlighted.

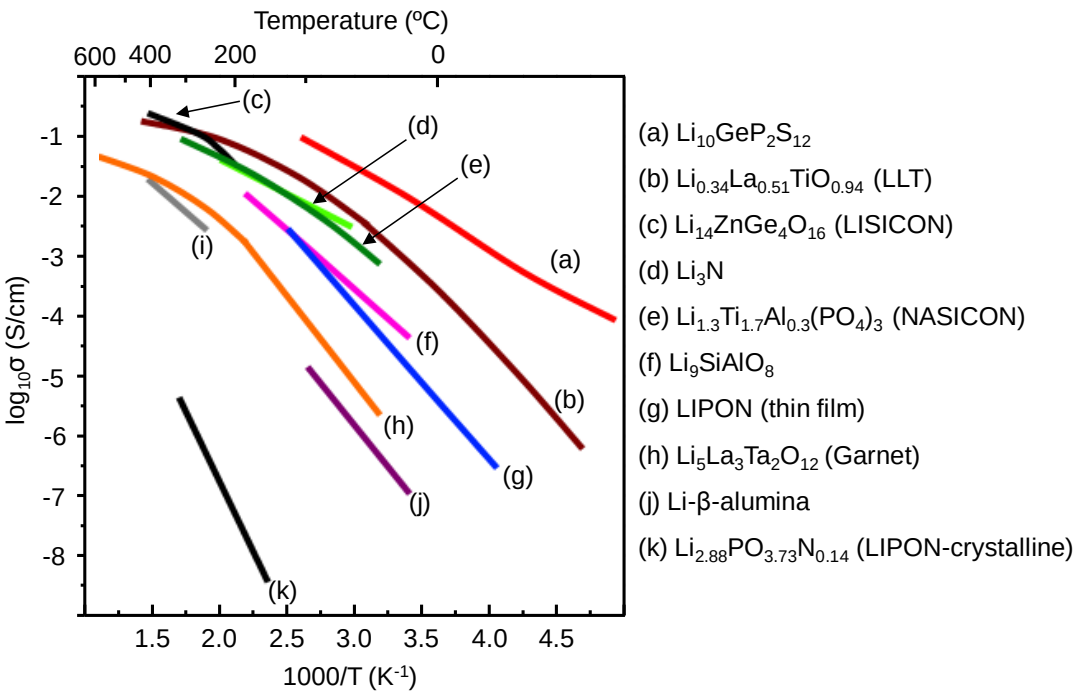

Figure 2.1. Arrhenius plots for the ionic conductivities of selected solid-state lithium ion conductors [3, 18].

2.2. Perovskite-type Lithium ion conductors

Perovskites, ABX_3 with generally cubic crystal symmetry, have been extensively studied due to their functional properties, e.g. electronic, magnetic, ferroelectric, ion conducting and optical properties [19-21]. The structure of perovskite is often depicted by corner-shared BX_6 octahedra enclosing 12 coordinated A-site ions as shown in Figure 2.2. Perovskites have different modifications, some have regular octahedra which are corner-shared in a straight line, but some others have also distorted structures accompanied by the distortion and tilting of the BX_6 octahedra and cation displacements [22,23]. Their properties can easily be tuned due to the simple structure which tolerates various kinds of chemical substitution on A, B and X sites [24].

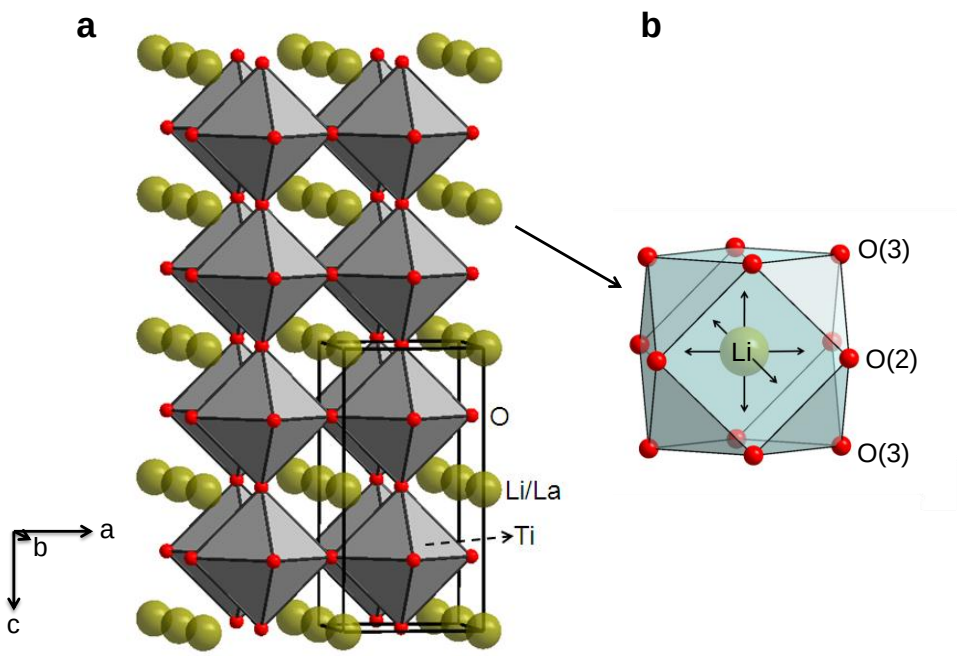

Figure 2.2. Crystal structure of tetragonal (*P*4/*mmm*) $Li_{3x}La_{3/2-x}TiO_3$ **(a)**. Lithium, lanthanum and vacancies are distributed at the A-sites. Schematic representation of 3D mobility of lithium ions in the perovskite structure **(b)**.

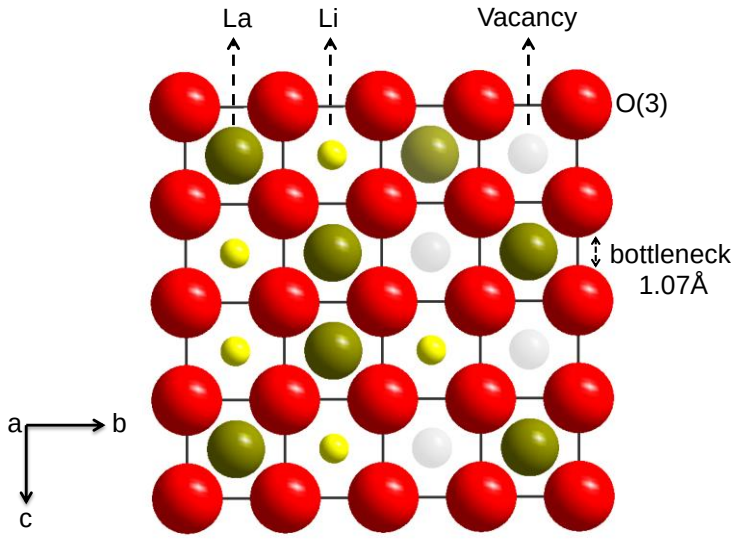

Figure 2.3. Schematic representation of the bottleneck for lithium ion conduction in the perovskite structure $Li_{3x}La_{3/2-x}TiO_3$ and vacancy are surrounded by 12 oxygen ions. [39].

Latie and Belous et al. have reported the first lithium ion conducting perovskite by hetero-valent substitution of La^{3+} by Li^{+} cations in the A-site deficient perovskite $La_{2/3}TiO_3$ [25,26]. Since then, $La_{2/3-x}Li_{3x}TiO_3$ (with optimum x≈0.11) has stimulated a wide interest because of its high bulk lithium ion conductivity (10^{-3} S/cm). Numerous studies were performed on this compound to better understand the details of the crystal structure, the effect lithium ion concentration and synthesis method on lithium ion conductivity properties [27-34]. The solid solution of $La_{2/3-x}Li_{3x}TiO_3$ has turned out to be stable over a wide range of cation compositions on the A site ($0.03 < x < 0.167$) [28]. It is crystallizing with various crystal symmetries depending on the composition and synthesis method, such as cubic (*Pm*3*m*) [28], hexagonal (*R*3*c*) only for $Li_{0.5}La_{0.5}TiO_3$[35], tetragonal (*P*4/*mmm*) (Figure 2.2a) with an ordered distribution of La ions on the perovskite A-sites along the c-axis ($0.08<x<0.16$) [36], and orthorhombic (*Cmmm*) with lower lithium content ($x<0.06$) [37,38]. Cubic and tetragonal $La_{2/3-x}Li_{3x}TiO_3$ (x≈0.11) have shown higher lithium ion conductivities with respect to the other crystal structure modifications [38,36]. The high lithium ion conductivity in $La_{2/3-x}Li_{3x}TiO_3$ can be attributed to the presence of many equivalent sites which enable the lithium ions to move freely along A-site vacancies [28] which is affected by the charge carrier concentration, the degree of order on the A-site, and the bottleneck size (figure 2.3).

The ionic conductivity σ can be expressed as follows;

$$\sigma = |e| n \mu \qquad \textbf{2.1}$$

where e is the elementary charge, n is the concentration of the charge carriers and μ is the mobility of the mobile species. It can be assumed that all the lithium ions in the $La_{2/3-x}Li_{3x}TiO_3$ perovskite structure can move independently of each other through A-site vacancies and that all the available A-sites (the concentration $N= (N_{Li} + N_V)$ for conduction are energetically and symmetrically identical. Thus, the charge carrier

concentration is depending on the lithium ions ($N_{Li} = 3x/V_s$) and A-site vacancy ($N_V = (1/3-2x)/V_s$) concentration where V_s is the perovskite subcell volume. Therefore the ionic conductivity can be expressed as follows

$$\sigma = |e| N_{Li} N_V / N\mu = |e| \frac{(x - 6x^2)}{\left(\frac{1}{3} + x\right) V_s} \mu \qquad \textbf{2.2}$$

Variation of the ionic conductivity versus carrier (lithium/vacancy) concentration with dome shape dependency can be obtained from Equation 2.2 with a maximum at x = 0.075. Such a behavior is indeed also obtained for the experimental data shown in figure 2.4 [39], except with a maximum at around x≈0.1.

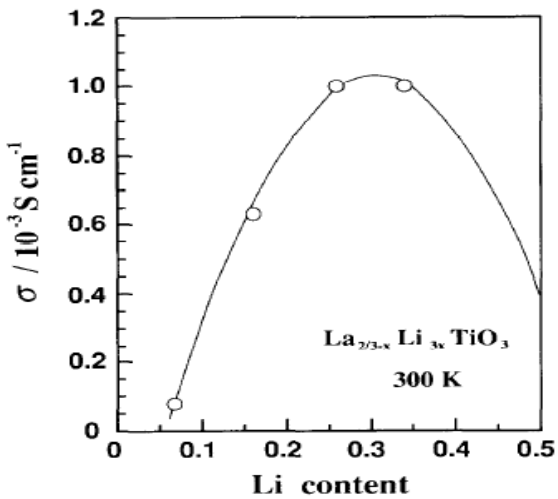

Figure 2.4. Variation of bulk lithium ion conductivity at 300K for $La_{2/3-x}Li_{3x}TiO_3$ as a function of lithium content [39].

The small discrepancy of the x values can be explained as follows. During our assumptions we have not taken into account the cooperative ionic motion in the A-site and the ordering of the A-site vacancies [40]. This difference can be attributed to the local distortion (tilting of TiO_6 octahedra) which decreases the bottle-neck size and slows down the lithium ion mobility. Thus the ionic conductivity is not only dependent

on the ratio of lithium-to-vacancy concentration but also the degree of ordering on the A-sites and the bottle neck size.

Secondly, the degree of ordering on the A-sites, which depends on the composition and synthesis temperature, is one of the determining factors for lithium ion conductivity. The cubic phase ($a=a_{perovskite}$) with disordered arrangements of lanthanum ions can be obtained by quenching from temperatures above 1150 °C. Whereas, the tetragonal phase ($a=a_{perovskite}$, $c=2a_{perovskite}$) with alternate arrangement of La-rich and poor layers along the c-axis can be obtained by annealing below 1150°C for $La_{2/3-x}Li_{3x}TiO_3$ ($x\approx0.11$) [28]. The degree of the ordered arrangements of La (S) can be defined as follows:

$$S=[R(\text{La-rich})-R(\text{La disordered})]/[1-R(\text{La-disordered})] \quad \textbf{2.3}$$

where R(La-rich) and R(La disordered) are the fractions of occupation ($0 < R < 1$) of A-sites by La ions in the La-rich layers of tetragonal form and in the (001) plane of the disordered cubic form, respectively [40]. The degree of the order (S) is varied by the diffusion of La ions between the La rich layer and La poor layers with temperature and since this is thermodynamically controlled, it is changing reversibly in the range of 600-1150°C [28, 40]. These results showed that parameter S is varying at different annealing temperatures and annealing time as shown in figure 2.5a.

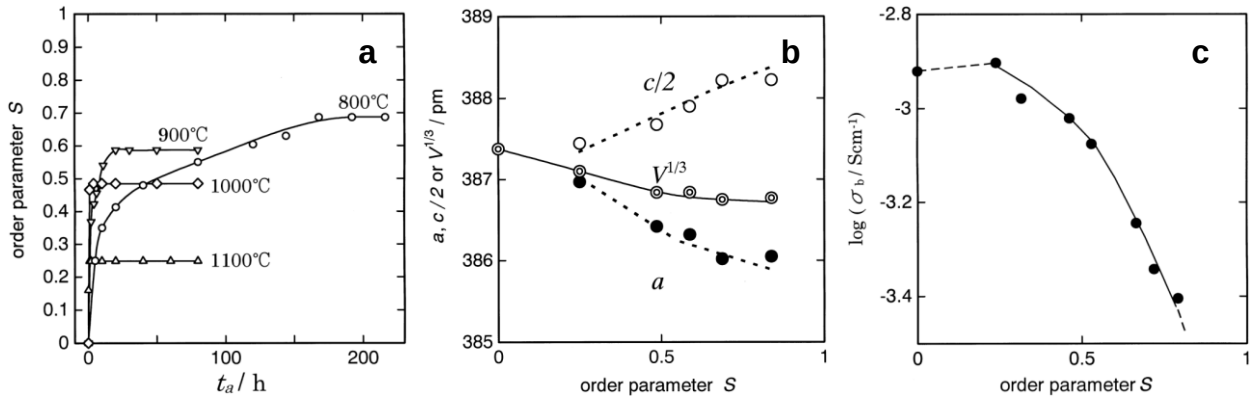

Figure 2.5. Variations of the order parameter (S) with annealing time (t_a) when the quenched $La_{2/3-x}Li_{3x}TiO_3$ (x = 0.11) sample (S = 0) was annealed at 800, 900, 1000 and 1100 °C **(a)**. Lattice parameters (a, c/2 and $V^{1/3}$) of the subcell for $La_{2/3-x}Li_{3x}TiO_3$ (x = 0.11) as a function of S**(b)**. Bulk ionic conductivity at 25°C for $La_{2/3-x}Li_{3x}TiO_3$ (x = 0.11) as a function of S **(c)** [40].

Figure 2.5b presents the lattice parameters of the subcell a, c/2 and $V^{1/3}$ as a function of the S parameter. The tetragonal distortion of the subcell is observed for S≥0.2 and the contraction of the subcell is increasing with an increasing distortion. In addition to these, the bulk ionic conductivity at 25 °C is decreasing as the order parameter is increasing from S ≈ 0.2 (figure 2.5c). Based on those results it is clear that the ordering of La ions causes contraction in the sub-lattice and simultaneously influences the migration pathways and as a consequence the ionic conductivity.

Another factor determining of the lithium ion conductivity in those compounds is the smallest cross-sectional area of the conduction channel also called bottleneck (figure 2.3) which is located in the space, surrounded by two adjacent A-sites and 4 oxygens. The bottle-neck size is the predominant factor for the ionic conduction [41-43] and it is dependent on the perovskite lattice parameter (a_p or V_s) as well as the structural distortions such as the tilt of the octahedra. Figure 2.6 shows the lithium ion conductivity and activation energies at 300K versus perovskite parameter, a_p of $Ln_{2/3-x}Li_{3x}TiO_3$ (Ln=La, Pr, Nd, Sm). It is clearly seen that as the ionic radius of Ln increases, the ionic conductivity increases.

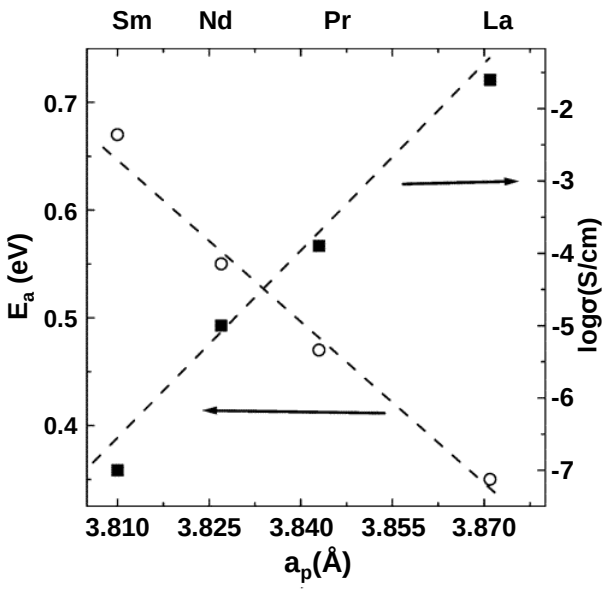

Figure 2.6. Variation of the ionic conductivity (■) and the activation energy (○) as a function of a perovskite lattice parameter for $La_{2/3-x}Li_{3x}TiO_{3\pm\delta}$ (Ln=La, Pr, Nd, Sm and x≈0.11) [43].

In summary, the highest ionic conductivity of about $1x10^{-3}$ S/cm can be achieved in the A-site deficient perovskite type $La_{2/3-x}Li_{3x}TiO_3$ when x ≈ 0.11. The ionic conductivity strongly depends on the size of the "bottleneck", concentration of the carrier (lithium and vacancy) concentration and the order/disorder. Although LLT is exhibiting high a lithium ion conductivity, it is not favorable as an electrolyte material for all-solid-state batteries due to its low electrochemical stability in direct contact with elemental lithium inducing titanium readily to be reduced from of Ti^{4+} to Ti^{3+} with lithium insertion.

2.3. Garnet-type lithium ion conductors

The garnet type compounds have been of significant attention in the field of materials science, due to their favourable magnetic, optical and electrical properties [44-47]. The ideal garnet-type structure crystallizes in cubic symmetry with a space group of *Ia*-3*d* (No.230). The general structural formula for an oxide garnet can be represented as $C_3A_2D_3O_{12}$ where the cations are coordinating the oxygen atoms by forming

dodecahedrons (C-site), octahedrons (A-site), and tetrahedrons (D-site), respectively. Kasper reported the first lithium-containing garnet compound series $Ln_3Te_2Li_3O_{12}$ (Ln=Lanthanides) with the ideal garnet stoichometry, 8 cations per formula unit, where Li fully occupies the tetrahedral sites [48]. These materials are showing, however, poor lithium ion conductivity (10^{-8} S/cm) [49]. Recently, Weppner et al. [16] discovered that the lithium rich garnet-related compounds, which are deviating from the ideal garnet stoichometry by having 8 or more cations per formula unit, have shown a high potential as ionic conductors for solid-state lithium ion batteries due to their high lithium ion conductivity with a very high decomposition voltage (6V versus Li). Examples of such Li conductors are $Li_5La_3Ta_2O_{12}$ (10^{-6} S/cm) and $Li_5La_3Nb_2O_{12}$ (10^{-6} S/cm) [16]. Those compounds can easily be deduced from $Ln_3Te_2Li_3O_{12}$ (Ln = lanthanide) with the regular $(dodecahedral)_3(octahedral)_2(tetrahedral)_3O_{12}$ composition by replacing each Te(VI) by Ta(V) or Nb (V) plus one Li(I) ion on the interstitial site. The structure of the highly conductive lithium ion garnets $Li_5La_3Ta_2O_{12}$, shown in figure 2.7a, reveals that lithium statistically occupies both tetrahedral and additional interstitial octahedral sites. This suggests that interstitial sites are necessary for the observed high lithium ion mobility due to the formation of interconnected sites (figure 2.7b) for lithium ion migration mechanism [50]. Since the total ionic conductivity of $Li_5La_3Ta_2O_{12}$ (10^{-6} S/cm) is almost two orders of magnitude lower than that of the bulk ionic conductivity ($7x10^{-5}$ S/cm), investigations were done to reduce the grain boundary resistance as well as further improvement in the ionic conductivity.

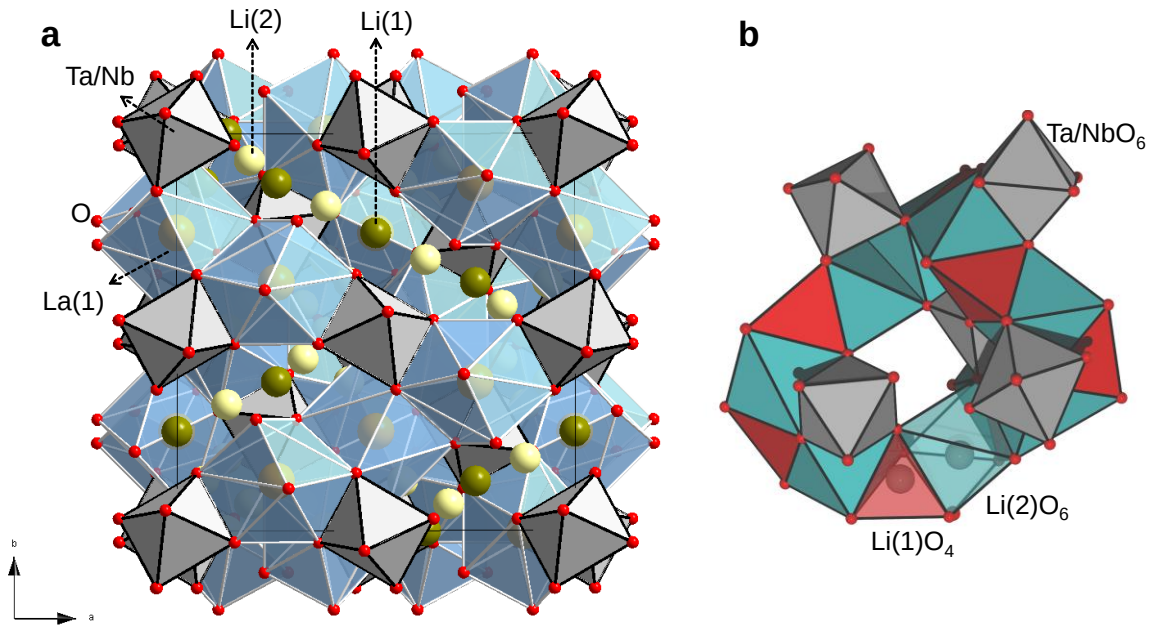

Figure 2.7. Crystal structure of $Li_5La_3M_2O_{12}$ (M=Nb/Ta) **(a).** Details of 3D Lithium ion migration path-way in $Li_5La_3M_2O_{12}$ (M=Nb/T a) **(b)**.

Systematic investigations were performed in which trivalent La in $Li_5La_3M_2O_{12}$ (M = Nb, Ta) was replaced by divalent alkaline earth and additional lithium ions for charge compensation. Series of compounds with the general formula $Li_6ALa_2M_2O_{12}$ (A = Ca, Sr, Ba; M = Nb, Ta) were synthesized among which $Li_6BaLa_2Ta_2O_{12}$ is exhibiting the highest total ion conductivity of 4×10^{-5} S/cm at 24°C (figure 2.8) with very low grain boundary resistance [17,18,-51]. The high bulk lithium ion conductivity in $Li_6BaLa_2Ta_2O_{12}$ can be explained by an increase in lattice parameters and substitution of Ba on the La sites which may modify the connectivity of the network and the number of accessible vacancies [51].

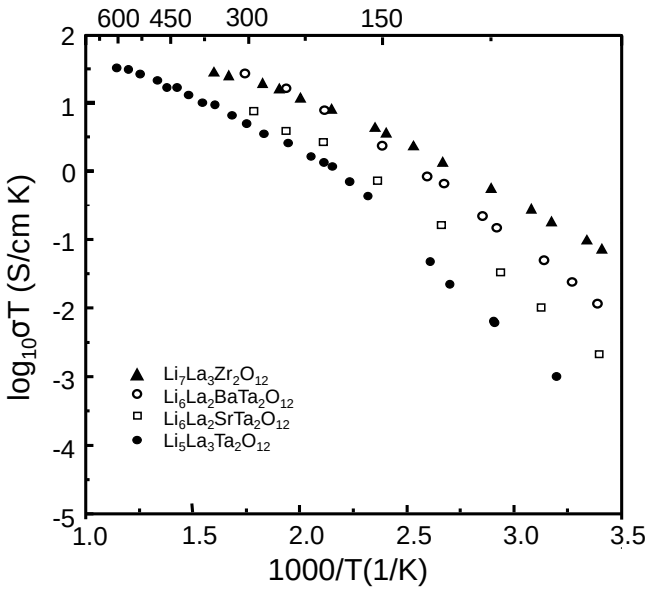

Figure 2.8. Comparison of total (bulk + grain boundry) lithium ion conductivities of garnet-type solid-state conductors reported in literature [49-51].

Besides Nb and Ta garnet-type fast lithium ion conductors, $Li_7La_3Zr_2O_{12}$ (Zr phases) was also found to have high lithium ion conductivity which has garnet related type structure with low temperature tetragonal (figure 2.9, $I4_1/acd$) [52] and high temperature cubic (*Ia-3d*) [53] modifications. Cubic $Li_7La_3Zr_2O_{12}$ was reported as one of the fastest lithium ion conductor in the garnet system, having bulk (10^{-4} S/cm) and total (5×10^{-4} S/cm) ionic conductivities [53] whereas the tetragonal modification shows a two orders of magnitude lower ionic conductivity [52]. Thus, the cubic phase of $Li_7La_3Zr_2O_{12}$ is preferred although the preparation of the cubic phase requires a high temperature annealing (>1250°C) and multiple grinding steps. Many groups have attempted different techniques, such as low temperature preparation by sol-gel synthesis [54] or the addition of Al for stabilization of the cubic phase at lower temperatures [55-57] to overcome this problem. The above-mentioned garnet compounds are promising as electrolyte materials for all-solid-state lithium ion batteries. Most importantly, these materials are electrochemically stable against metallic lithium, moisture, air and

common electrode materials, such as $LiCoO_2$ and $LiMnO_2$ [58]. Cubic $Li_7La_3Zr_2O_{12}$ and $Li_6BaLa_2Ta_2O_{12}$ took special attention among the others due to their high lithium ion conductivity.

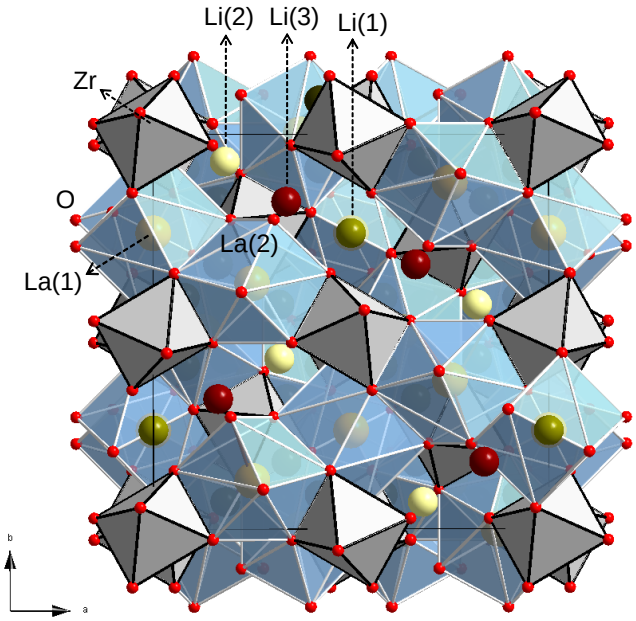

Figure 2.9. Crystal structure of tetragonal $Li_7La_3Zr_2O_{12}$ ($I4_1/acd$)

2.4. NASICON-related Lithium ion conductors

The crystal structure of ($NaM_2^{IV}(PO_4)_3$ (M=Ge, Ti and Zr), *Na S*uper *I*onic *Con*ductor also denoted as NASICON, was first identified in 1968 and crystallizes in the rhombohedral space group *R*-3*c* [59]. The NASICON structure is built up by $[M_2(PO_4)_3]^-$ units, in which MO_6 octahedra are connected to PO_4 tetrahedra by sharing oxygens as shown in figure 2.10. This linkage generates 3D interconnected channels with partially occupied sites for sodium cations which results in fast sodium ion conduction [60].

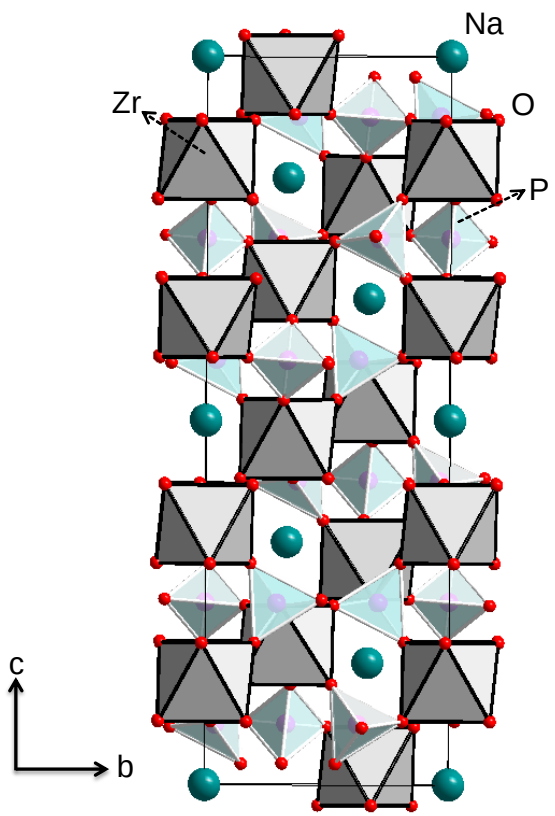

Figure 2.10. Crystal structure of $NaZr_2(PO_4)_3$. The solid box indicates the unit cell

Subsequently, Hong reported the introduction of the lithium ions into the NASICON-type structure by Na^+/Li^+ exchange [61]. Since then, there is an extensive research for better solid-state lithium ion conductors with NASICON-type structure and its lithium ion conductivity properties [62-64]. $LiTi^{IV}_2(PO_4)_3$ exhibits the highest lithium ion conductivity of $\sigma \approx 10^{-5}$ S/cm at 25°C in the compound series $LiM^{IV}_2(PO_4)_3$ (M=Ge, Ti, Zr, Hf) inspite of its relatively lower cell volume than some of those. (Figure 2.11) [13-66].

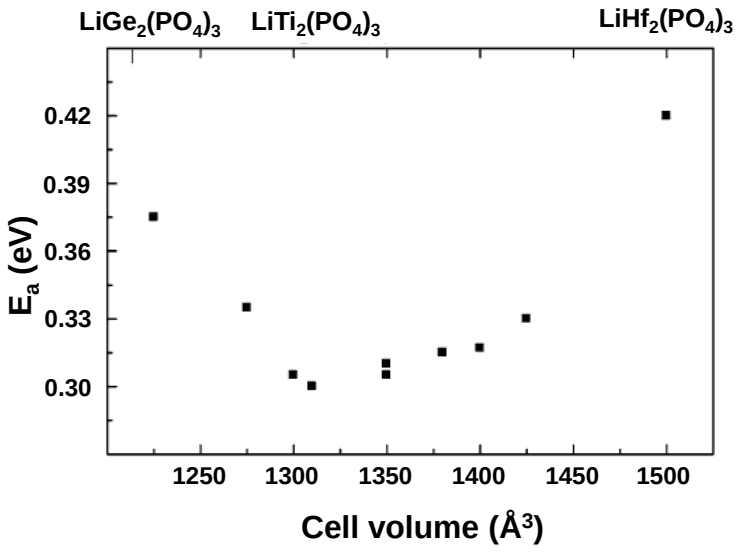

Figure 2.11. Relationship between the activation energy for Li ion conductivity and the cell volume of the NASICON-type compounds.[11]

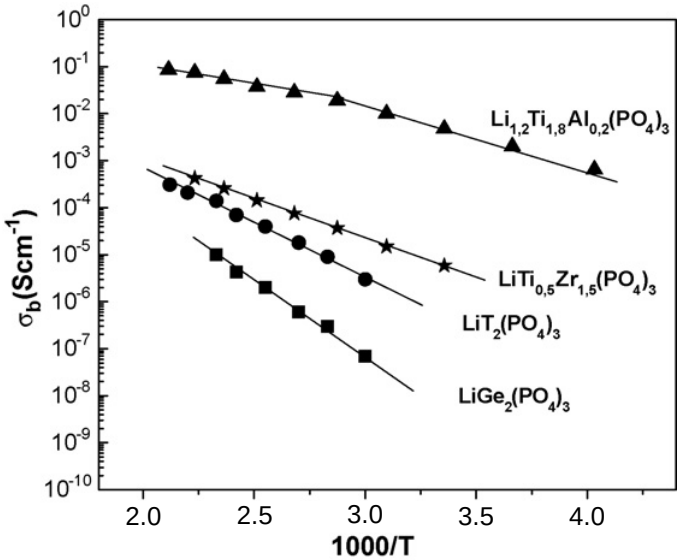

Figure 2.12. Arrhenius plot of the ionic conductivity of various solid lithium ion conductors with NASICON structure [67].

The partial substitution of Ti^{4+} (0.60 Å) in $LiTi^{IV}_2(PO_4)_3$ by trivalent cations (Al, Cr, Ga, Fe, Sc, In, Lu, Y or La) was also investigated and it was found that substitution of Al^{3+} (0.53 Å) which has the smallest anionic radius of the studied elements, has improved the lithium ion conductivity due to the increased in carrier concentration, decrease in the porosity and increase in M-O bond strength, simultaneously weakening the Li-O bond strength [66]. Among all NASICON-related compounds, $Li_{1.3}Al_{0.3}Ti_{1.7}(PO_4)_3$ showed the highest lithium ion conductivity of $\sigma \approx 3x10^{-3}$ S/cm as shown in Figure 2.12 [66]. Those results show that the ionic conductivity in NASICON-related compounds is not only related to cell volume consideration but also carrier concentration, the density of the material and the chemical environment of lithium.

In conclusion, NASICON-related lithium ion conductors are very promising with high lithium ion conductivity but Ti containing NASICON compounds are electrochemically unstable with respect to the metallic lithium due to the reduction of Ti^{4+} to Ti^{3+} and accompanying of lithium insertion similar to that found for the $Li_{3x}La_{3/2-x}TiO_3$ perovskites.

2.5. LISICON-type and thio-LISICON Li ion conductors

The first LISICON (*Li*thium *S*uper *I*onic *Con*ductor) compound reported is $Li_{3.5}Zn_{0.25}GeO_4$ which is a member of the solid solutions of $Li_{2+2x}Zn_{1-x}GeO_4$ ($-0.36 < x < 0.87$) [10, 68, 69]. The solid solutions are based on stoichiometric and fully ordered Li_2ZnGeO_4, which is iso-structural with γ-Li_3PO_4 and can be derived by the double substitution of P^{5+} and Li^+ by Ge^{4+} and Zn^{2+}, respectively.

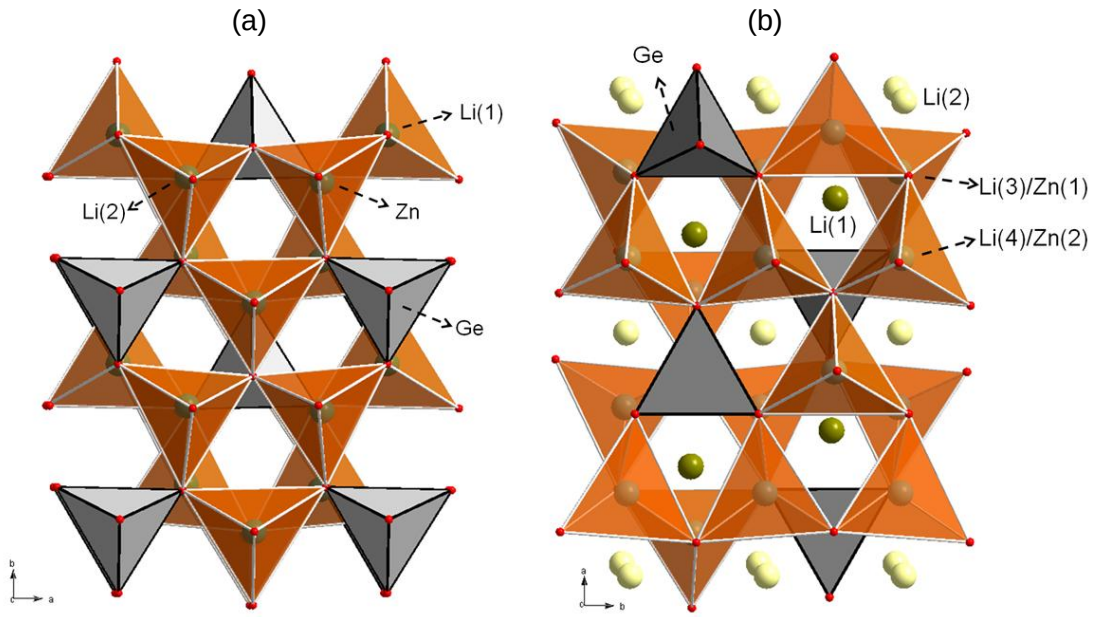

Figure 2.13. Crystal structures of Li_2ZnGeO_4 **(a)** and $Li_{3.5}Zn_{0.25}GeO_4$ (LISICON) **(b)**. The remaining lithium occupies the interstitial sites within the rigid network of LISICON.

The Li-rich solid solutions, including $Li_{3.5}Zn_{0.25}GeO_4$, is crystallizing in the *Pnma* orthorombic space group as shown in figure 2.13 and a LISICON network is formed by elements of $[Li_{2+x}Zn_{1-x}GeO_4]^{x-}$ and the remaining x amount of lithium (Li_x). Lithium ions are statistically distributed among two sets of inequivalent octahedral sites, 4c (Li1) and 4a (Li2), which are located in the interstitial sites within the rigid network. Each 4c site is connected to two 4a positions, and vice versa. The bottleneck size between these connected sites is large enough to fulfill the geometrical conditions for fast lithium ion transport in two dimensions [70]. The Zn rich compounds ($x < 0$) contain vacant Li^+ in the tetrahedral sites [71].

The highest lithium ion conductivity measured is 0.12 S/cm at 300 °C (figure 2.1) but only $1x10^{-7}$ S\cm at room temperature can be reached with $Li_{3.5}Zn_{0.25}GeO_4$ stoichiometry ($x \approx 0.75$) [72]. The ionic conductivity tends to reduce in time at low temperature in LISICON compounds. This can be explained due to the occurrence of phase segregation that appears to be driven by the formation of Li_4GeO_4, which is trapping the mobile

lithium ions by the immobile sub lattice at lower temperatures [72,73]. Re-annealing the samples to restore the conductivity to its original properties of $Li_{2+2x}Zn_{1-x}GeO_4$ compounds was unsuccessful to find extensive application in lithium ion batteries due to the aging problem and the low ionic conductivity at room temperature. A wide variety of materials have then been synthesized within the LISICON family, with its framework being related to the γ-Li_3PO_4 structure and are formed by GeO_4, SiO_4, PO_4, ZnO_4 or VO_4 tetrahedra. From those possible compounds, $Li_{3.6}Ge_{0.6}V_{0.4}O_4$ showed the highest room temperature conductivity around $4x10^{-5}$ S/cm among the others [74], whereas $Li_{3.4}Si_{0.4}V_{0.6}O_4$ was found to be stable in contact with lithium even above 180 °C. It has a slightly lower ionic conductivity $1x10^{-5}$ S/cm at room temperature than germanium analogues [75,76].

Lithium ion conducting sulfide compounds (thio-LISICON) $Li_{4-x}M_{1-y}M'_yS_4$ (M=Si, Ge and M=P, Al, Zn, Ga) have a structure similar to γ-Li_3PO_4 structure, and have also been investigated [77]. $Li_{3.25}Ge_{0.25}P_{0.75}S_4$ showed the highest lithium ion conductivity ($2.17X10^{-3}$ S/cm) at room temperature [78] and the high lithium ion conductivity in sulfides can be explained due to the larger bottle neck-size and more polarizable sulfide ions compared to oxygen ions. This makes the conducting moieties more mobile in the crystal structure [79].

2.6. LiPON and related systems

In crystalline γ-Li_3PO_4, as in LISICON, each O^{2-} ion is bonded to four network cations (three lithium and one phosphorous) [80], however, the ionic conductivity of γ-Li_3PO_4 is very low, because all the Li-ions form part of the network and there are no other lithium vacancies. As a result crystalline γ-Li_3PO_4 has a very low mobility of $\sigma = 4.2x10^{-18}$ S/cm at 25 °C [81]. Wang et al. also prepared polycrystalline $Li_{2.88}PO_{3.73}N_{0.14}$ which can be considered as lithium ion deficient γ-Li_3PO_4. By creating vacancies on the lithium position, the lithium ion conductivity can be enhanced by 5 orders of magnitude at 25

°C (σ = 1.4x10^{-13} S/cm) [81] (figure 2.1). In addition to the bulk crystalline material properties, more significant changes were obtained during the amorphous thin film studies. The thin film form of Li_3PO_4 and related compounds has extensively been studied before and showed high lithium ion conductivity at room temperature (≈ 10^{-8} S/cm) as well as good mechanical and electrochemical stability [82-87]. Bates et al. first reported the LiPON as an amorphous thin film form by sputter deposition of Li_3PO_4 in N_2 atmosphere. It can be considered as a lithium ion deficient Li_3PO_4 with a chemical composition $Li_xPO_yN_z$ where x=2y+3z-5 [87,88]. The solid solution with a composition $Li_{2.9}PO_{3.3}N_{0.46}$ where the nitrogen is incorporated into the structure, exhibits a 40 times higher lithium ion conductivity σ = 3.3 x 10^{-6} S/cm at 25 °C (figure 2.1) than the Li_3PO_4 deposited in a mixture of argon and oxygen atmosphere [89]. The increase in ionic conductivity is supposed to be related to the formation of cross-linked and more covalent P-N bonds which replaces P-O bonds, making it a more reticulated anionic network [90]. Various structural investigations suggested that the structures consist of doubly coordinated nitrogen (N_d) P-N=P and triply coordinated nitrogen (N_t) P-N<$^{P}_{P}$ units. Hu et al. reported that the ionic conductivity increases with the N_t content of thin films because N_t structural units provide a higher cross-linking density of glass network of LiPON [91]. Many groups have investigated the influence of deposition parameters on the chemical composition as well as the lithium ion conductivity. In general, it has been found that the ionic conductivity strongly depends on the compositional parameters and the compositional parameters strongly depend on the target size and density, and the geometric parameters of the deposition [92].

2.7. Summary

Inorganic solid lithium ion conductors provide advantages compared to liquid electrolytes, such as safety and durability due to their mechanical, thermal and electrochemical stability. The solid-state lithium ion conductors also enable miniaturization, especially by using thin-film deposition techniques.

Perovskite type $La_{2/3-x}Li_{3x}TiO_3$ with x ≈ 0.11 and NASICON-related lithium ion conductors, $Li_{1.3}Al_{0.3}Ti_{1.7}(PO_4)_3$,are very promising because of their high lithium ion conductivity of $1x10^{-3}$ S/cm and $3x10^{-3}$ S/cm at room temperature, respectively, but those compounds are not favorable as an electrolyte material for all-solid-state batteries due to their low stability in direct contact with elemental lithium, where titanium readily undergoes a reduction of Ti^{4+} to Ti^{3+} with lithium insertion. Garnet-related compounds, especially cubic-$Li_7La_3Zr_2O_{12}$ and $Li_6BaLa_2Ta_2O_{12}$ draw special attention due to their high lithium ion conductivity (≈10^{-4} S/cm) and chemical stability against electrode materials. However, the ionic conductivities are not as high as those of liquid electrolytes (10^{-2} S/cm). At 300 °C, $Li_{3.5}Zn_{0.25}GeO_4$ with LISICON-related structure has a high lithium ion conductivity, 0.12 S/cm, but it is showing only $1x10^{-7}$ S/cm at room temperature which makes these materials only suitable for high temperature battery applications. On the contrary, sulfides with LISICON-related structure, $Li_{3.25}Ge_{0.25}P_{0.75}S_4$ (thio LISICON), show very high room temperature lithium ion conductivity of $2.17x10^{-3}$ S/cm. The increase in lithium ion conductivity can be explained due to the larger and more polarizable sulfide ions substituted over oxygen ions which make the conduction species more mobile in the crystal structure. Recently, Kamaya et al. reported a new sulfide based solid electrolyte ($Li_{10}GeP_2S_{12}$) with new structure. It exhibits an exceptionally high ionic conductivity of 0.12 S/cm at room temperature (figure 2.1) and electrochemical stability against electrode material [7]. Besides the above-mentioned crystalline compounds, amorphous LiPON (thin film form) also combines a good

lithium ion conductivity of $3.3x10^{-6}$ S/cm and high stability against metallic lithium ion. The ease of thin film deposition of this compound is very important and it facilitates the fabrication of micro-batteries in both 2D and 3D architecture which can increase energy and power density.

In summary, the investigations and the results showed that the ionic conductivity is mostly influenced by bottle neck-size, charge carrier concentration and polarizability of the anions. In the most structure types, the ionic conductivity is increasing as the bottleneck size increase, except for the NASICON where the partial substitution of Ti^{4+} (0.60 Å) by trivalent cation Al^{3+} (0.53 Å) and Li^{+} substitution has increased the ionic conductivity. But non-isovalent substitution in NASICON also increases the carrier concentration. As mentioned above, another influencing factor is the charge carrier concentration, especially in the perovskite and garnet-related compounds; it is affecting the connectivity of the network and the number of accessible vacancies. As can be seen in the sulfides, the chemical environment of lithium ion is also important for the mobility of these species.

2.8. References

[1] P.H.L. Notten, F. Roozeboom, R.A.H. Niessen, L. Baggetto, Adv. Mater. **2007**, 19, 4564.

[2] L. Bagetto, R.A.H. Niessen, F. Roozeboom, P.H.L. Notten, Adv. Funct. Mater. **2008**, 19, 1057.

[3] V. Thangadurai, W. Weppner, Ionics **2006**, 12, 81.

[4] B.Scrosati, Electrochemical Acta. **2000**, 45, 2461.

[5] A.G. Ritchie, J. Power Sources **2004**, 136, 285.

[6] S. Stramare, V. Thangadurai, W. Weppner, Chem. Mater. **2003**, 15, 3974.

[7] N. Kamaya, K. Homma, Y. Yamakawa, M. Hirayama, R. Kanno, M. Yonemura, T. Kamiyama, Y. Kato, S. Hama, K. Kawamoto, A. Mitsui, Nature Materials **2011**, 10, 682.

[8] A. R. J. West, Appl. Electrochem. **1973**, 3, 327.

[9] A. Kvist, A.Lunden, Z. Naturforsch. **1965**, 20a, 235.

[10] H. Y.-P. Hong, Mater. Res. Bull. **1978**, 13, 117.

[11] H. Aono, H. Imanaka, G. Y. Adachi, Acc. Chem. Res. **1994**, 27, 265.

[12] G. Y. Adachi, N. Imanaka, H. Aono, Adv. Mater. **1996**, 8, 127.

[13] H. Aono, E. Sugimoto, Y. Sadaoka, N. Imanaka, G. Adachi, J. Electrochem. Soc. **1989**, 136, L590.

[14] G. C. Farrington, B. S. Dunn, J. L. Briant, Solid State Ionics **1981**, 3–4, 405.

[15] M. Itoh, Y. Inaguma, W. Jung, L. Chen, T. Nakamura, Solid State Ionics **1994**, 70, 203.

[16] V. Thangadurai, H. Kaack, W. Weppner, J. Am. Ceram. Soc. **2003**, 86, 437.

[17] V. Thangadurai, W. Weppner, Adv. Funct. Mater. **2005**, 15, 107.

[18] V. Thangadurai, W. Weppner, J. Am. Ceram. Soc. **2005**, 88, 411.

[19] F. S. Galasso, 'Structure properties and preparation of perovskite-type compounds" Pergamon Press **1969.**

[20] A.S. Bhalla, R. Guo, R. Roy, R. Mater Res. Innovat. **2000**, 4,3.

[21] V. Thangadurai, W. Weppner, J. Electrochem Soc. **2001**, 148, A1294.

[22] M. Glazer, Acta Crystallogr. A **1975**, 31, 756.

[23] M. Glazer, Acta Crystallogr. B **1972**, 28, 3384.

[24] L. Sebastian, J. Gopalakrishnan, J. Mater. Chem. **2003**, 13, 433.

[25] L. Latie , G. Villeneuve, D. Conte, G. L. Flem, J. Solid State Chem. **1984,** 51, 293.

[26]A. G. Belous, G. N. Novitsukaya, S. V. Polyanetsukaya, Y.I. Gornikov, Izv. Akad. Russ. J. Inorg. Chem **1987**, 32, 1956.

[27] H. Kawai, J. Kuwano, J.Electrochem. Soc. **1994**, 141, L78.

[28] Y. Harada, Y. Hirakoso, H. Kawai, J. Kuwano, Solid State Ionics **1999**, 121, 245.

[29] T. Katsumata, Y. Matsui, Y. Inaguma, M. Itoh, Solid State Ionics **1996**, 86-88, 165.

[30] Y. Inaguma, M. Itoh, Solid State Ionics **1996**, 86-88, 257.

[31] S. Kunugi, Y. Inaguma, M. Itoh, Solid State Ionics **1999**, 122, 35.

[32] J. Ibarra, A. Varez, C. Leon, J. Santamaria, L.M. Torres-Martinez, J. Sanz, Solid State Ionics **2000**, 134, 219.

[33] C.W.Ban, G. M. Choi, Solid State Ionic **2001**, 140, 285.

[34] H.X. Geng, A. Mei, C. Dong, Y.H. Lin, C.W. Nan, J. Alloys and Comp. **2009**, 481, 555.

[35] J. A. Alonso, J. Sanz, J. Santamaría, C. León, A. Várez, M. T. Fernández-Díaz, Angew.Chem Int. Ed. **2000**, 39, 619.

[36] Y. Inaguma, C. Liguan, M. Itoh, T. Nakamura, T. Uchida, H. Ikuto, M. Wakihara, Solid St. Comm. **1993**, 86, 689.

[37] J. Sanz, J. A. Alonso, A. Varez, M. T. Fernández-Díaz, J. Chem. Soc., Dalton Trans. **2002**, 7, 1406.

[38] Y. Inaguma, T. Katsumata, M. Itoh, Y. Morii, J. Solid State Chem. **2002**, 166, 67.

[39] Y. Inaguma, L. Chen, M. Itoh, T. Nakamura, Solid State Ionics **1994**, 70/71, 196.

[40] Y.Harada, T. Ishigaki, H. Kawai, J. Kuwano, Solid State Ionics **1998**, 108, 407.

[41] Y. Inaguma, L. Chen, M. Itoh, T. Nakamura, Solid State Ionics **1994**, 70-71, 196.

[42] Y. Inaguma , J. Yu, Y.J. Shan, M. Itoh, T. Nakamura, J. Electrochem. Soc., **1995**, 142, L8.

[43] M. Itoh, Y. Inaguma, W. H. Jung, L. Chen, T. Nakamura, **1994**, 70/71, 203.

[44] G. C. Lau, T. Klimczuk, F. Ronning, T. M. McQueen, R.J. Cava, Phys. Review B **2009**, B80, 21441.

[45] F. J. Kahn, P.S. Pershan, Physical Review **1969**, 186, 891.

[46] E. E. Anderson, J. Appl. Physics **1959**, 4, 299.

[47] J. Nicolas, Microwave Ferrites, in: E.P. Wohlfarth (ed.), Ferromagnetic Materials, vol. 1, North-Holland, Amstedam **1982**, 243.

[48] H.M. Kasper, Inorg. Chem. **1968**, 8, 1000.

[49] M.P.O'Callaghan, D.R. Lynham, E.J. Cussen, G. Z. Chen, Chem. Matter. **2006**, 18, 4681.

[50] E.J. Cussen, Chem. Commun., **2006**, 412-413.

[51] R. Murugan, V. Thangadurai, W. Weppner, Appl. Phys. **2008**, A91, 615.

[52] J. Awaka, N. Kijima, H. Hayakawa, J. Akimoto, J. Solid State Chem. **2009**, 182, 2046.

[53] R. Murugan, V. Thangadurai, W. Weppner, Angew. Chem.. Int. Ed. **2007**, 46, 7778.

[54] I. Kokal, M. Somer, P.H.L. Notten, H.T. Hintzen, Solid State Ionics **2011**, 185, 42.

[55] Y. Shimonishi, A. Toda, T. Zhang, A. Hirano, N. Imanishi, O. Yamamoto, Y. Taked, Solid State Ionics **2011**, 183, 48.

[56] C.A. Geiger, E. Alekseev, B. Lazic, M. Fisch, T. Armbruster, R. Langner, M. Fechtelkord, N. Kim, T. Pettke, W. Weppner, Inorg. Chem., **2011**, 50, 1089.

[57] S. Kumazaki, Y. Iriyama, K.-H. Kim, R. Murugan, K. Tanabe, K. Yammato, T. Hirayama, Z. Ogumi, Electrochem. Commun. **2011**, 13, 5, 506

[58] V. Thangadurai, W. Weppner, J. Power Sources **2005**, 142, 339.

[59] L.O. Hagman, P. Kierkegaard, Acta. Chem.Scand. **1968**, 22, 1822.

[60] J. B. Goodenough, H. Y.-P. Hong and J. A. Kafalas, Mater. Res. Bull., **1976**, 11, 203

[61] H. Y.-P. Hong, Mater. Res. Bull., **1976**, 11, 173.

[62] B. ETaylor, A. D. English, T. Berzins, Mater. Res. Bull. **1977**, 12, 171.

[63] M. Barj, H. Perthuis, Ph. Colomban, Solid State Ionics **1983**, 9-10, 845.

[64] D. Petit, P. Colomban, G. Collin and J. P. Boilot, Mater. Res. Bull. **1986,** 21, 365.

[65] H. Aono, E. Sugimoto, Y. Sadaoka, N. Imanaka and G. Adachi, J. Electrochem. Soc. **1990**, 137, 1023.

[66] H. Aono, E. Sugimoto, Y. Sadaoka, N. Imanaka and G. Adachi, Solid State Ionics **1991**, 47, 257.

[67] K. Arbi, J.M. Rojo, J.Sanz, J. Eur. Ceram. Soc. **2007**, 27, 4215.

[68] P.G. Bruce, A.R. West, Mat. Res. Bull. **1980**, 15, 117.

[69] E. Plattner, H. Vollenkle, Monatsh. Chem. **1979**, 110, 693.

[70] I. Abrahams, P.G. Bruce, W.I.F. David and A.R. West, Acta Crystallogr. Sect. B **1989**, 45, 457.

[71] I. Abrahams, P.G. Bruce, J. Solid State Chem. **1988**, 75, 390.

[72] P.G. Bruce, A.R. West, J. Solid State Chem. **1982** 44, 354.

[73] P.G. Bruce, A.R. West, J. Solid State Chem. **1984,** 53, 430.

[74] J. Kuwano, A.R. West, Mat. Res. Bull. **1980**, 15, 1661.

[75] A. Khorassani, A. R. West, J. Solid State Chem. **1984**, 53, 369.

[76] J. Yamaki, H. Ohtsuka, T. Shodai, Solid State Ionics **1996**,86-88, 1279.

[77] M. Murayama, R. Kanno, Y. Kawamoto, T. Kamiyama, Solid State Ionics **2002**, 154, 789.

[78] R. Kanno, M. Murayama Journal of Electrochem. Soc. **2001**, 148, A742.

[79] R. Kanno, T. Hata, Y. Kawamoto, M. Irie Solid State Ionics **2000**, 130, 97.

[80] J. Zemann, Acta Cryst. **1960**, B13, 863.

[81] B. Wang, B.C. Chakoumakos, B.C. Sales, B.S. Kwak, J.B. Bates J. Solid State Chem. **1995**, 115, 313.

[82] J. B. Bates, G.R. Gruzalski, N.J. Dudney, C.F. Luck, X. Yu, Solid State Ionics **1994**, 70-71, 619.

[83] C.H. Choi, W.I. Cho, B.W. Cho, H.S. Kim, Y.S Yoon, Y.S Tak, Electrochem. Solid State Lett. **2002**, 1, A14.

[84] X. Yu, J. B. Bates, G.E. Jellison, F.X. Hart J. Electrochem. Soc. **1997**, 2, 254.

[85] Z. Hu, D. Li, K. Xie, Bull. Mater. Sci. **2008**, 31, 681.

[86] J.F.M. Oudenhoven, F. Labohm, M. Mulder, R.A.H. Niessen, F. M. Mulder, P.H.L. Notten, Adv. Mater. **2011**, 23, 4103.

[87] J.B. Bates, N.J. Dudney, B. Neudecker, A. Ueda, C.D. Evans, Solid State Ionics, **2000**, 135, 33.

[88] Y.A.Du, N.A.W. Holzwarth Physical Review B **2010**, B81, 184106-1.

[89] J.B. Bates, N.J. Dudney, G.R. Gruzalski, R.A. Zuhr, A. Choudhury, C.F. Luck, J. Power Sources **1993**, 43-44, 103.

[90] F. Munoz, A. Duran, L. Pascual, L. Montagne, B. Revel, A.C.M. Rodrigues, Solid State Ionics **2008**, 179, 574.

[91] Z. Hu, K. Xie, D. Wei, N. Ullah, J. Mater. Sci. **2011**, 46, 7588.

[92] Y. Hamon, A. Douard, F. Sabary, C. Marcel, P. Viinatier, B. Pecquenard, A. Levasseur

Solid State Ionics, **2006**, 177, 257.

Chapter 3.

$Li_{0.5}La_{0.5}TiO_xN_y\square_{3-(x+y)}$: Synthesis, Structure and Lithium Ion Conductivity Properties

Abstract

Starting from one of the best solid-state lithium ion conductors, $Li_{0.5}La_{0.5}TiO_3$ with high ionic conductivity (≈10^{-5}S/cm), new perovskite-type oxynitride solid solutions have been synthesized by thermal ammonolysis at 1223K of $Li_{0.5}La_{0.5}TiO_3$ precursor prepared by a solid-state reaction method. The chemical composition and structural properties of the resulting oxynitrides have been investigated by elemental analysis, thermal gravimetric analysis, x-ray photoelectron spectroscopy (XPS) and x-ray powder diffraction (XRPD). The influence of nitrogen incorporation on lithium ion conductivity was analyzed by AC Impedance Spectroscopy.

3.1. Introduction

The studies of lithium ion conducting materials are very important for the development of solid-state lithium secondary batteries [1]. In the past few years, with the investigation of the high ionic conductivity in lithium lanthanum titanate by Inagamu et al. [2], lithium containing solid oxides with perovskite type structure has attracted extensive interest. Since the perovskite type structure (ABO_3) can tolerate substitutions on both A and B sites partially and completely with different valance states, $La_{2/3-x}Li_{3x}TiO_3$, $Ln_{½}Li_{½}TiO_3$ (Ln = La, Pr, Nd, Sm) [3], $Li_{1/3-x}Li_{3x}MO_3$ (M = Ta, Nb) [4] were systematically investigated and reported as high lithium ionic conductors with conductivities in between 10^{-3}-10^{-7} S/cm. In addition to these cationic substitutions, crystallographic and electronic structures of perovskite can also be changed by anionic substitution which is also a well established method. Due to the similarity of the anionic radii of F^- and N^{3-} to O^{2-}, oxynitrides and oxyflurides are considered to be the most suitable mixed anion systems [5]. So far, research on the lithium ionic conductivity has been focused on modifications of the cation composition in these compounds. Modifications of the anion composition are not investigated extensively. Accordingly, we have synthesized and characterized the first oxynitride of lithium lanthanum titanium with perovskite structure.

3.2. Experimental Method

3.2.1. Synthesis

Precursor material, $Li_{0.5}La_{0.5}TiO_3$, was prepared by a conventional solid-state reaction technique. Reagents of Li_2CO_3 (Alfa 99.9% in purity), La_2O_3 (Alfa 99.9% purity, heated overnight at 1000°C in air atmosphere) and TiO_2 (Sigma Aldrich 99.9% purity) were mixed in a molar ratio of 1.1:1:2. Due to the evaporation of lithium, 10 % excess was used to obtain the desired composition. The mixture was annealed at 1073 K for 6 hours

and subsequently at 1473 K for 12 hours in air atmosphere with several intermittent grindings until single phase $Li_{0.5}La_{0.5}TiO_3$ was obtained. Polycrystalline oxynitride powder samples were prepared by thermal ammonolysis of synthesized precursor $Li_{0.5}La_{0.5}TiO_3$ with flowing ammonia (500 ml/min) for 1, 5 and 10 hours at 1223 K. In addition to the conventional solid-state reaction technique, polycrystalline oxynitride powder samples were also obtained by thermal ammonolysis of oxide precursor which was prepared by a modified Pechini sol-gel process as described elsewhere [6].

3.2.2. X-ray Powder Diffraction

The phase formation of the precursor and phase formation of resulting oxynitride were identified by XRPD analysis with a Bruker Enduar D4 diffractometer using CuKα radiation at room temperature in the 2 theta range from 5° to 90° with a step size of 0.01°. Structural refinements of the resulting compounds were performed with FullProf software [7].

3.2.3. Elemental Analysis

The molar ratio of the metals (Li, La, Ti) in the precursor and oxynitride compounds was determined by inductive coupled plasma – optical emission spectroscopy (ICP-OES). The samples were dissolved in concentrated HCl solution in a sealed pyrex glass tube at 150°C for 6 hours.

3.2.4. Thermal Analysis by Oxidation of the Oxynitride Compounds

To determine the nitrogen content, thermo gravimetric analysis (TGA) was performed by using Mettler Toledo TGA/SDTA 851. The thermo gravimetric effects were investigated in Al_2O_3 crucibles from room temperature up to 1273 K with a heating rate of 5 K/min in air.

3.2.5. XPS Analysis

X-ray photoelectron spectroscopy (XPS) measurements were performed with a VG CLAM II hemispherical analyzer with a channeltron detector. Powders were pressed into 2 mm thick pellets and placed onto Al sample holders by using double-sided conductive carbon tape. The spectra have been recorded using a Mg-$K_{\alpha 1}$ (1253.6eV) X-ray source under ultrahigh vacuum ($1x10^{-9}$ mbar) at room temperature. The XPS binding energy was calibrated to the binding energy of carbon 1s (285.0 eV). XPS Casa software with Shirley background correction was used to fit the XPS spectra.

3.2.6. Lithium Ion Conductivity

Lithium ion conductivities were analyzed with AC Impedance Spectroscopy. Measurements of the ionic conductivity were conducted in an argon glove-box using a Li/PP(LES)/specimen/PP(LES)/Li cell, where Li and PP(LES) represent metallic lithium electrodes and a thin sheet of porous polypropylene film (PP) absorbing lithium electrolyte solution (LES: 1M $LiClO_4$ in ethylene carbonate). The PP(LES) was used not only to filter the electronic conductivity of the specimen but also to prevent it from coming into contact with lithium which may cause the reduction of Ti^{+4} to Ti^{+3} [8]. Ionic conductivities of the samples were measured within the frequency range from 100 Hz to 1 MHz at room temperature, using a potentiostat with frequency response analyzer (Ivium Stat).

3.3. Results and discussion

3.3.1. Chemical Composition, Phase Analysis and Crystal Structure

The chemical composition of the compounds was determined by ICP-OES and thermo-gravimetric analysis. TGA measurements were performed by heating the oxynitride samples in air to determine the nitrogen content in the compounds from the amount of

weight gain when 2/3 N^{3-} is replaced by O^{2-}. Figure 3.1 shows that weight gain increases for longer reaction time during ammonolysis. Significant oxidation started above 673K, it ends at 923 K and subsequently loses weight upon further heating. This can be ascribed to the release of nitrogen retained in the lattice [9]. Based on the calculations from the final weight gain in TGA combined with ICP-OES analysis for the cations, the nitrogen content for the compounds were calculated and the results are presented in Table 3.1.

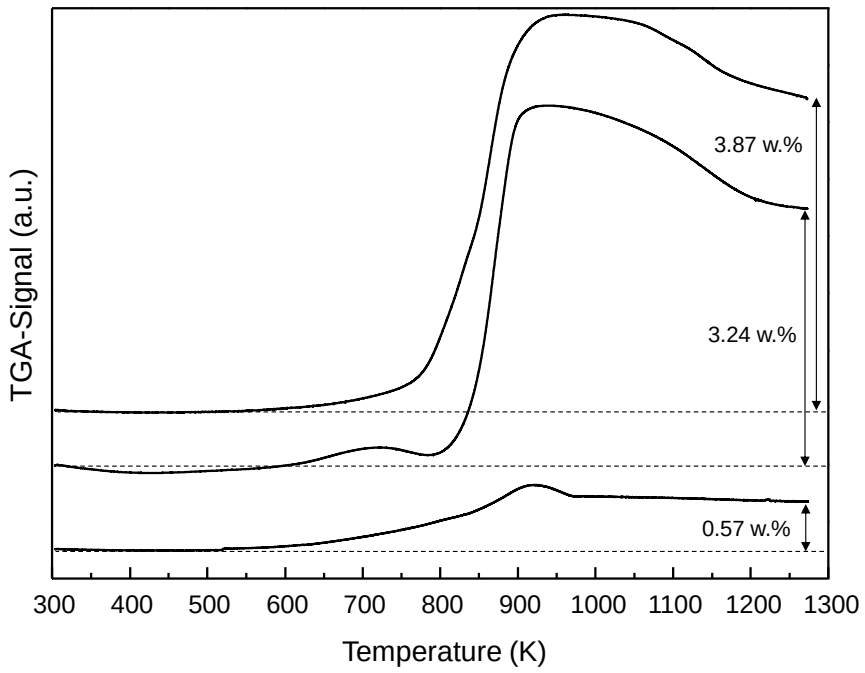

Figure 3.1. Oxidation of 1, 5 and 10 hours heated Oxynitride samples measured by TGA in air with heating rate 5 K min^{-1}.

Reaction Time	Composition of Oxynitride	Weight Gain (TGA)
1 hour	$Li_{0.48(1)}La_{0.51(1)}TiO_{2.85}N_{0.10}\square_{0.05}$	0.57%
5 hours	$Li_{0.47(2)}La_{0.51(1)}TiO_{2.20}N_{0.53}\square_{0.27}$	3.24%
10 hours	$Li_{0.43(1)}La_{0.50(1)}TiO_{2.09}N_{0.58}\square_{0.32}$	3.87%

Table 3.1. Compositions of oxynitrides after thermal ammonolysis at 1223K.

The thermal ammonolysis of $Li_{0.5}La_{0.5}TiO_3$ precursor for 1 hour yields an oxynitride with perovskite structure and a minor impurity phase, which was identified as lithium inserted TiO_2 (Figure 3.2). The crystal symmetry and cell parameters were determined by Rietveld methods using FullProf software [7]. The new oxynitride with low nitrogen content is isotypic to that of the oxide precursor and crystallizes in the P4/mmm space group with a slightly larger unit cell (a= 3.874(3) Å and c= 7.747(2) Å where a ≈ $a_{perovskite}$, and c ≈ 2·$a_{perovskite}$) due to the incorporation of larger N^{3-} anions in the O^{2-} sites.

Compound	Space Group	a (Å)	c (Å)	$a_{perovskite}$ (Å)	σ at 298K ($S \cdot cm^{-1}$)	Color
$Li_{0.5}La_{0.5}TiO_3$	*P*4/mmm	3.867(4)	7.746(2)	3.870	3.2 X10^{-5}	White
$Li_{0.48(1)}La_{0.51(1)}TiO_{2.85}N_{0.10}\square_{0.05}$	*P*4/mmm	3.874(3)	7.747(2)	3.873	1.8 X10^{-5}	Green
$Li_{0.47(2)}La_{0.51(1)}TiO_{2.20}N_{0.53}\square_{0.27}$	Pm-3m	3.924(2)	-	3.924(2)	3.4 X10^{-6}	Black
$Li_{0.43(1)}La_{0.50(1)}TiO_{2.09}N_{0.58}\square_{0.32}$	Pm-3m	3.926(4)	-	3.926(4)		Black
$LaTiO_2N$ [11]	Pm-3m	3.945(1)	-	3.945(1)		Brown
$La_{0.5}Ba_{0.5}TiO_{2.5}N_{0.5}$ [12]	Pm-3m	3.971(2)	-	3.971(2)		Pale Brown

Table 3.2. Structural characteristics and properties of various Lanthanum Titanium Oxynitrides

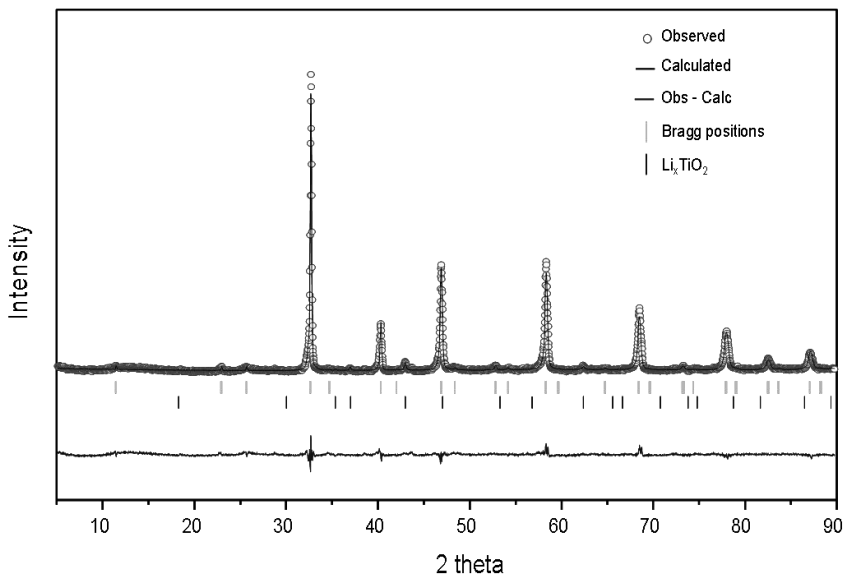

Figure 3.2. Refined X-ray Powder Diffraction pattern of $Li_{0.48}La_{0.51}TiO_{2.85}N_{0.10}\square_{0.05}$ including Li_xTiO_2 as minor phase.

Figure 3.3 presents the XRPD patterns of the compounds obtained after the thermal ammonolysis of $Li_{0.5}La_{0.5}TiO_3$ at 1223 K for 5 and 10 hours. The diffraction lines are showing the characteristics of the perovskite structure and can be indexed as pseudo-cubic. However, the new perovskite type oxynitride compound actually crystallizes in I-1(triclinic) space group and is isotypic to $LaTiO_2N$ which has been refined using neutron diffraction by Clarke et al. [10]. The splitting attributed to triclinic symmetry was observed in oxynitride prepared by a modified sol-gel Pechini process because better crystallinity was achieved from more reactive precursor material. Instead of refining all parameters of the solid solutions, verification of the linear evolution of the cell parameters and formation of solid solution can easily be done by using a cubic unit cell. In this sense, these XRPD results combined with the chemical analysis indicate that the new oxynitride compounds can also be presented as lithium substituted $LaTiO_2N$. Table 2 shows the experimental parameters for $LaTiO_2N$ and its substituted compounds. Since the size of the unit cell is also depending on the size of the cation in

the A-site and the anion in the O-sites, Li-substituted compounds have smaller lattice parameters than $LaTiO_2N$ and A-site substituted $LaTiO_2N$ (A=Ba) [12].

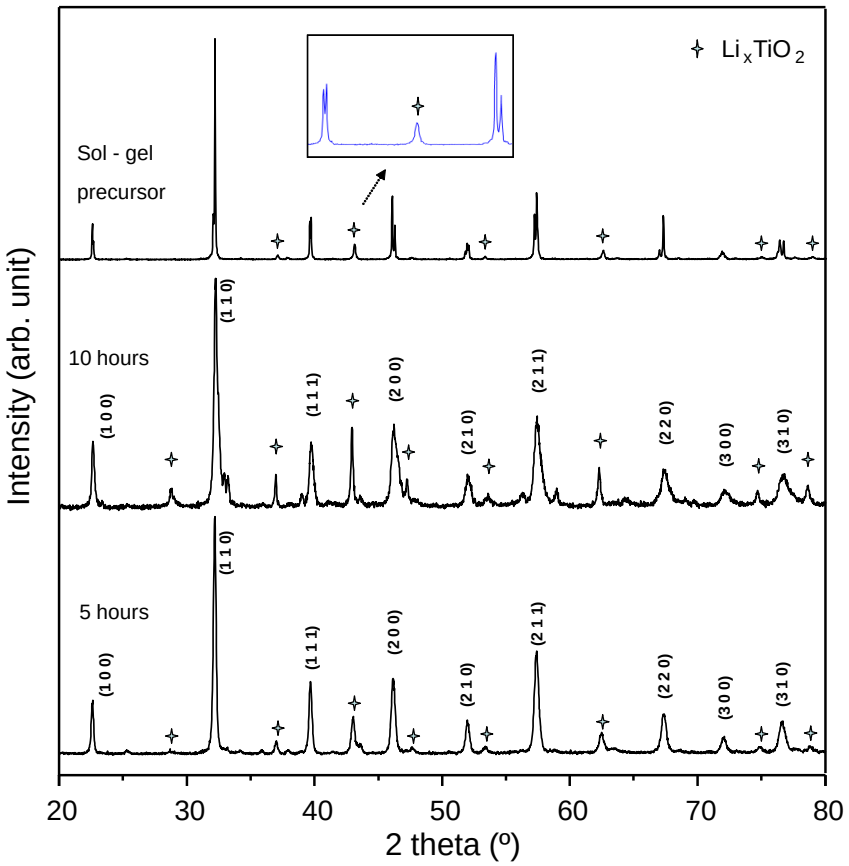

Figure 3.3. XRPD patterns of ammonolyzed samples for 5 and 10 hours, indexed as pseudo-cubic and oxynitride prepared from sol-gel processed precursor (5 hours ammonolysis time).

XPS analyses were conducted to qualitatively analyze titanium, oxygen and nitrogen. Figure 3.4 displays the XPS spectra of the Ti_{2p}, N_{1s} and O_{1s} signals. The peak around 458.4 eV was assigned to $Ti_{3p/2}$ and is characteristic for Ti^{4+}. But the peak width is increasing for higher nitrogen containing compounds. This can be explained by taking into account the change and distortion in the ideal TiO_6 coordination into $Ti(O,N,\square)_6$ and the contribution of Ti^{3+} centers in Li_xTiO_2 to the spectra. Since the amount of Li_xTiO_2 is increasing with reaction time, Ti^{3+} centers may also be expected to appear in the XPS spectra. Nitrogen and oxygen signals were observed at 396 and 533 eV, respectively, for

the oxynitride samples. In addition to these observations the intensity of the nitrogen peak is increasing with ammonolysis time. These results clearly indicate that anionic substitution occurs in the $Li_{0.5}La_{0.5}TiO_3$-system by thermal ammonolysis and its amount increases with reaction time.

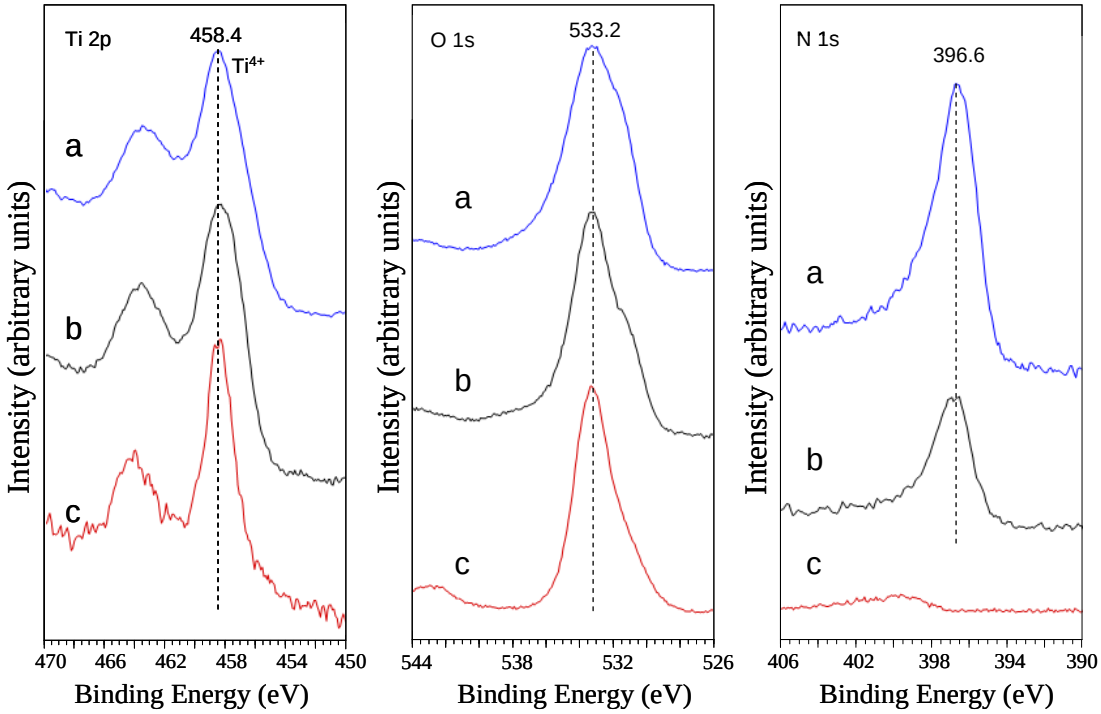

Figure 3.4. Ti_{2p}, O_{1s} and N_{1s} narrow scan XPS spectra for **(a)** $Li_{0.47}La_{0.51}TiO_{2.20}N_{0.53}\square_{0.27}$ **(b)** $Li_{0.48}La_{0.51}TiO_{2.85}N_{0.10}\square_{0.05}$ and **(c)** $La_{0.5}Li_{0.5}TiO_3$.

3.3.2. Lithium Ion Conductivity

AC impedance plots were recorded at room temperature for the poly-crystalline samples; $La_{0.5}Li_{0.5}TiO_3$, $Li_{0.48}La_{0.51}TiO_{2.85}N_{0.10}\square_{0.05}$ and $Li_{0.47}La_{0.51}TiO_{2.20}N_{0.53}\square_{0.27}$ in the frequency range 1 MHz to 100 Hz and typical Nyquist plots are shown in Figure 3.5. The ionic conductivities were calculated from the intersection of the semicircle with the real axis and the geometric shape of the samples (diameter and thickness of the pallet). The ionic conductivity of the $La_{0.5}Li_{0.5}TiO_3$ sample was measured to be 3.2×10^{-5} S/cm which is similar to previous studies [13]. The ionic conductivities of the oxynitride

compounds are somewhat lower: σ = 1.8 ×10^{-5} S/cm for $Li_{0.48}La_{0.51}TiO_{2.85}N_{0.10}\square_{0.05}$ and 3.4 ×10^{-6} S/cm for $Li_{0.47}La_{0.51}TiO_{2.20}N_{0.53}\square_{0.27}$.

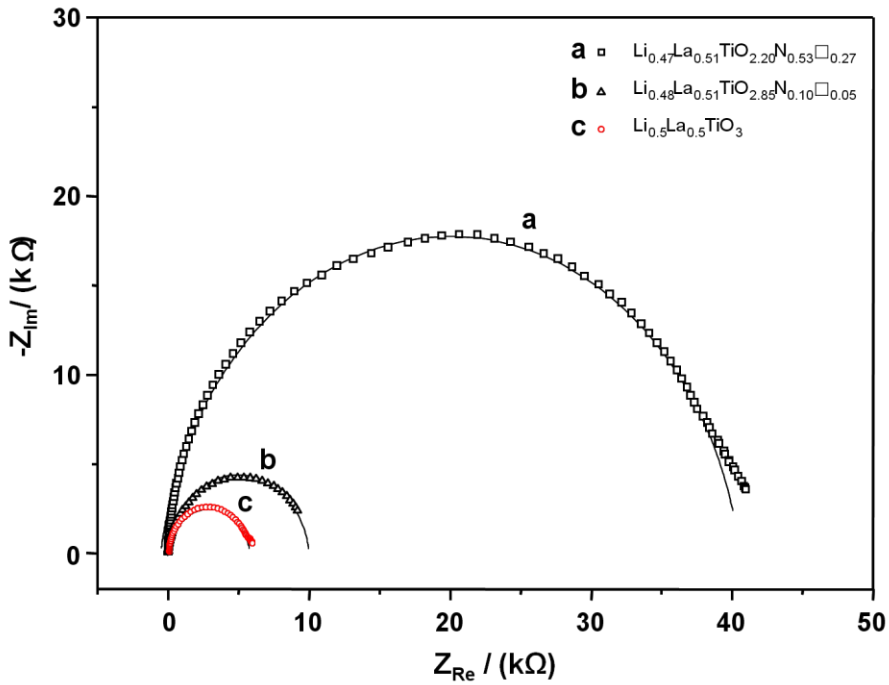

Figure 3.5. Complex impedance plots for the ionic conduction of $Li_{0.47}La_{0.51}TiO_{2.20}N_{0.53}\square_{0.27}$ **(a)**, $Li_{0.48}La_{0.51}TiO_{2.85}N_{0.10}\square_{0.05}$ **(b)** and $Li_{0.5}La_{0.5}TiO_3$ **(c)**

The lower ionic conductivity values might be related to the change in the crystal symmetry of the compound due to nitrogen substitution with oxygen and additional vacancies on the anionic sub-lattice.

3.4. Conclusions

Anionic substitution of nitrogen on the oxygen sites in $La_{0.5}Li_{0.5}TiO_3$ was achieved by thermal ammonolysis of $La_{0.5}Li_{0.5}TiO_3$ oxide precursor. XRPD measurements have shown that oxynitride compounds crystallize in perovskite type structure. The degree of substitution is the determining factor for the size of the unit cell, the number of anion vacancies and the crystal symmetry of the compounds. Nitrogen substitution with oxygen lowers the symmetry from tetragonal to triclinic due to the distortions in the octahedra and additional vacancies in the anion sites. Because of the symmetry changes,

the lithium ion conductivities of these compounds decrease with the increase in substitution of nitrogen by oxygen.

3.5. References

[1] P.H.L. Notten, F. Roozeboom, R.A.H. Niessen, L. Baggetto, Adv. Mater. **2007**, 19, 4564.

[2] M. Itoh, Y. Inaguma, W. Jung, L. Chen, T. Nakamura, Solid State Ionics **1994**, 70, 203.

[3] M. Nakayama, T. Usui, Y. Uchimoto, M. Wakihara, M. Yamamoto, J. Phys. Chem. B. **2005**, 109, 4135.

[4] Y. Inaguma, L. Chen, M. Itoh, T. Nakamura J, Solid State Ionics **1994**, 70, 196

[5] Y. Kim, P. M. Woodward J. Solid State Chem. **2007**, 180, 3224.

[6] M. Vijayakumar, Y. Inaguma, W. Mashiko, M. P. C. Lopez, C. Bohnke, Chem. Mater. **2004**, 16, 2719.

[7] J. Rodriguez-Carvajal, "FULLPROF", Laboratoire Le' on Brillouin (CEA-CNRS), France, **2006**.

[8] K.Y Yang, I Leu, K. Fung, M. Hon, M.Hsu, Y. Hsiao, M. Wang, J. Mater. Res. **2008**, 23, 1813.

[9] J.W.H Krevel, H.T Hintzen, R. Metselaar, L. Le Gendre, R. Marchard, Solid State Sciences. **2001**, 3, 49

[10] S. Clarke, B. Guinot, C Michie, M. Calmont, M Rosseinsky, Chem. Mater. **2002**, 14, 288.

[11] D. Logvinovich, A. Borger, M. Dobeli, S.G. Ebbinghaus, A. Reller, A. Weidenkaff, Progress in Solid State Chem. **2007**, 35, 281.

[12] F. Chevire, F. Tessier, R. Marchand, Eur. J. Chem. **2006**, 6, 1223.

[13] Y. Inaguma, L. Chen, M. Itoh, T. Nakamura, Solid State Ionics **1994**, 71, 196.

Chapter 4.

Sol-Gel Synthesis and Lithium Ion Conductivity of $Li_7La_3Zr_2O_{12}$ with Garnet-related Type Structure

Abstract

Lithium ion conducting garnet-related type $Li_7La_3Zr_2O_{12}$ (LLZO) nanopowders were prepared by the modified sol-gel Pechini method from stoichiometric mixtures of lithium carbonate, lanthanum oxide and zirconium ethoxide. The LLZO precursor powders were annealed at various temperatures between 923 and 1173 K for 5 hours in air atmosphere. The products were characterized by thermal analysis (TG/DTA) and X-ray powder diffraction (XRPD) to verify the transformation from precursor powder to crystalline garnet-related phase. XRPD analysis shows that the cubic phase of garnet-related type $Li_7La_3Zr_2O_{12}$ is formed at 978 K and the tetragonal garnet-related phase above 997 K. The morphology of the particles was investigated by Scanning Electron Microscopy (SEM). The lithium ionic conductivity of the tetragonal $Li_7La_3Zr_2O_{12}$ sample prepared by sol – gel synthesis is found to be 3.12×10^{-7} S/cm at 298K. The results of the ionic conductivities are in good agreement with those of the tetragonal LLZO synthesized by conventional solid-state synthesis method.

* The content of this chapter has been published as I.Kokal, M. Somer, P.H.L. Notten, H.T.J.M. Hintzen, Solid State Ionics, **2011**, 185, 42.

4.1. Introduction

Research on all-solid-state lithium ion batteries is of great interest because of their high energy density, high safety and low toxicity. Lithium-ion batteries are nowadays playing an important role in energy storage technologies and are mainly based on $LiCoO_2$ as cathode material, metallic lithium or graphite as anode material and LiPON as solid-state electrolyte [1-3]. The recent investigations on lithium ion conductors are extended to a wide range of compounds with different crystal structures types such as Li_4SiO_4, Li_2SO_4, $Li_{14}ZnGe_4O_{16}$, $Li_{1+x}Ti_{2-x}M_x(PO_4)_3$ (M = Al, Sc, Y, La), Li–β–alumina, $Li_{0.34}La_{0.5}TiO_{2.98}$ with perovskite structure and lately with garnet-related type $Li_5La_3M_2O_{12}$ (M = Nb, Ta) [4-11]. Some of the reported ionic conductivities for the above mentioned compounds are in between 10^{-3} and 10^{-7} S/cm.

Compounds having garnet-related type structure with the chemical formula $Li_5La_3M_2O_{12}$ (M = Nb, Ta) were first reported by Weppner et al. [12]. They crystallize in the cubic symmetry (space group *Ia*-3*d*) and exhibit high lithium conductivity (10^{-6} S/cm). To verify the role of the lithium content on lithium ionic conductivity, systematic investigations were performed in which trivalent La in $Li_5La_3M_2O_{12}$ (M = Nb, Ta) was replaced by divalent alkaline earth and additional lithium ions for charge compensation. Series of compounds with the general formula $Li_6ALa_2M_2O_{12}$ (A = Ca, Sr, Ba; M = Nb, Ta) were synthesized among which $Li_6BaLa_2Ta_2O_{12}$ is exhibiting the highest ionic conductivity of 4×10^{-5} S/cm at 297 K [13-15]. Beside Nb and Ta phases, $Li_7La_3Zr_2O_{12}$ with cubic garnet-related type structure was synthesized at 1500 K which is reported to be one of the best lithium ion conductors having a $\sigma_{bulk} \approx 10^{-4}$ S/cm at 300 K combined with good thermal and chemical stability against potential electrode materials. However, the details of the structure is not completely solved yet [16]. Awaka et al. succeeded in growing single crystals of $Li_7La_3Zr_2O_{12}$ at relatively low temperature of

1253 K and presented it as the first tetragonal garnet-related phase (space group $I4_1/acd$) [17].

In this chapter, we will report on a novel low-temperature cubic garnet-related phase and the known tetragonal garnet-related phase with the chemical composition $Li_7La_3Zr_2O_{12}$ synthesized by modified Pechini sol-gel processes at 973 and 1073 K, respectively. The ionic conductivity of the tetragonal $Li_7La_3Zr_2O_{12}$ compound is measured and compared with that from previous studies.

4.2. Experimental Method

4.2.1. Synthesis

Powders of Li_2CO_3 (Alfa, 99.9%), La_2O_3 (Alfa 99.9%, dried overnight at 1273K in air atmosphere), $Zr(OC_2H_5)_4$ (Sigma Aldrich 97%), citric acid as organic complexing agent, and ethylene glycol as organic solvent were used as starting materials with a molar ratio 7:3:4:28:14. We take into account the ratio (CM = [CA]/[[Metal]) of moles of complexing agent [CA] and cations [Metal] around 1 which defines the degree of chelation process. Li_2CO_3 and La_2O_3 were dissolved in dilute HNO_3 and $Zr(OC_2H_5)_4$ in absolute ethanol, respectively. Both solutions were mixed and subsequently highly concentrated citric acid and ethylene glycol were added. The obtained solution was stirred vigorously and heated to 323 K for 3 hours in air. Afterwards the solvent was slowly evaporated and concentrated at 373 K. Finally yellowish transparent gels were obtained, which were then dried and decomposed at 473 K for 24 hours in air to yield highly reactive brown precursor powders. The resultant product was ground well and calcined at temperatures between 923 and 1173 K for 5 hours in air atmosphere to obtain LLZO polycrystalline powders.

4.2.2. Characterization

Thermal analysis (TG/DTA) of the precursor powder was conducted by using a Mettler Toledo TGA/SDTA 851 instrument. The thermal effects were investigated in 70 μl Al_2O_3 crucibles from 300 to 1273 K with a heating rate of 5 K/min in flowing air atmosphere (50 ml/min). Structural characterization of resulting compounds was performed by X-ray powder diffraction (XRPD) analysis with a Bruker Enduar D4 diffractometer using CuKα radiation at room temperature in the 2 theta range from 5° to 90° with a step size of 0.01° and counting time per step of 1 second. Structural refinements of the resulting compounds were performed with FullProf software [18]. Morphology changes of the powder materials annealed at different temperatures were investigated by scanning electron microscopy using a Quanta 3D FEG instrument (FEI Company). Ionic conductivity measurements were performed from 290 to 353 K using a potentiostat with frequency response analyzer (Ivium Stat) operating at 100 mV constant potential within the frequency range of 100 Hz to 1 MHz in air atmosphere. The pellets with 0.1 cm thickness and area of 1.12 cm^2 were prepared by pressing the powder sample with sintering at 1173 K for 4 hours combined with a polishing process. Then, gold paste was painted on both sides of the pellets and cured at 923 K in air to form the ionically blocking electrodes.

4.3. Results and discussion

4.3.1. Thermal Analysis

Figure 4.1 presents the TG/DTA curves of the precursor powders dried at 473 K in flowing air atmosphere.

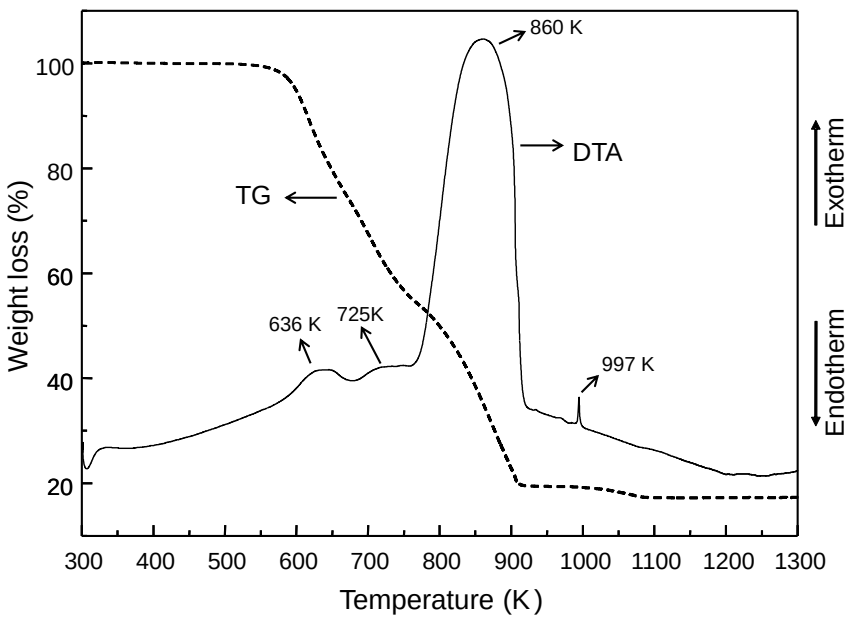

Figure 4.1. TG/DTA curves of the dried precursor obtained by sol-gel method.

Significant weight loss within two steps was observed between 600 and 900 K and four different exothermic effects were recorded at 636, 725, 860 and 997 K, respectively, in the DTA curve. Two weak and broad exothermic peaks at 636 and 725 K emerged during the first step of the weight loss which is approximately 40 % and can be ascribed to the degredation of the reactants The second weight loss starts in the range 750-950 K is accompanied by a strong exothermic peak about at 860 K and is due to the oxidation of residual organic compounds. There is no significant weight change after 900 K indicating that the transformation of the precursor to oxides starts above this temperature. The exothermic peak at 997 K is attributed to phase transition of cubic LLZO to tetragonal LLZO which is also verified by XRPD analyses.

4.3.2. X-ray Powder Diffraction

The XRPD patterns after calcination of LLZO precursor powder at different temperatures for 5 hours are shown in figure 4.2. The diffraction peaks of the LLZO precursor powder calcined at 923 K correspond to a mixture of $La_2Zr_2O_7$ (JCPDS 73-

0444) and Li_2CO_3 (JCPDS 83-1454). The results prove that the precursor is completely transformed to two different modifications of garnet-related type LLZO phases at ≥ 973K.

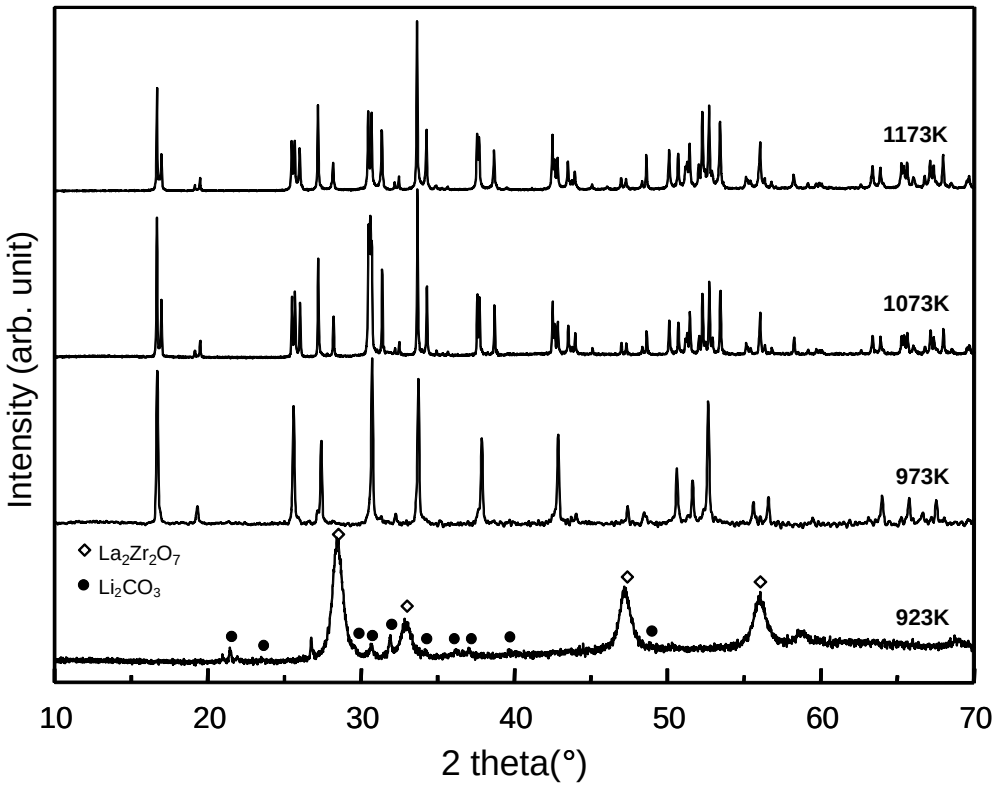

Figure 4.2. XRPD patterns of the LLZO precursors calcined at 923, 973, 1073 and 1173 K.

The XRPD patterns of the compounds calcined at 973 and 1073 K were indexed by using Fullprof software. The results of the calculation are presented in Table 4.1, the difference between the experimental and calculated data are illustrated and the R values as well as the significance of the fit are reported in Figure 4.3 and 4.4.

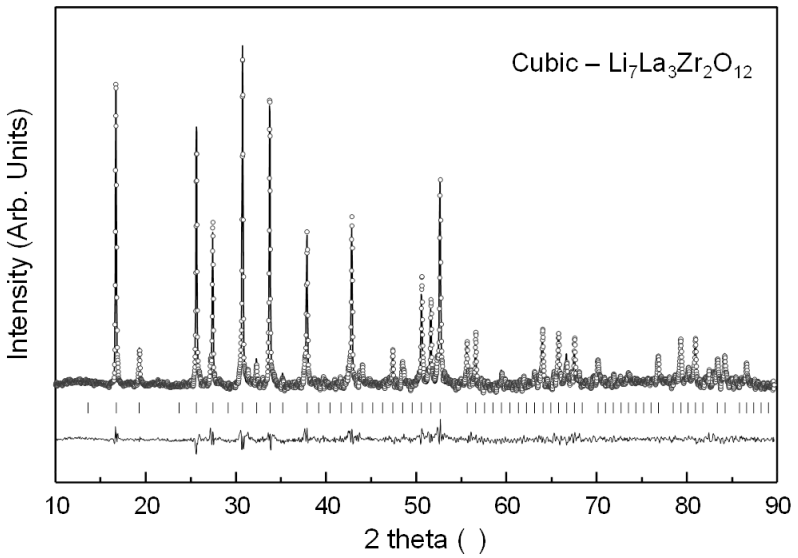

Figure 4.3. Observed (open circle), calculated (solid line), Bragg reflections (vertical lines) and difference (bottom) patterns for the calculated pattern from the x-ray powder diffraction data of cubic-$Li_7La_3Zr_2O_{12}$. (Rp = 0.13, wRp = 0.18 and X^2=3.73)

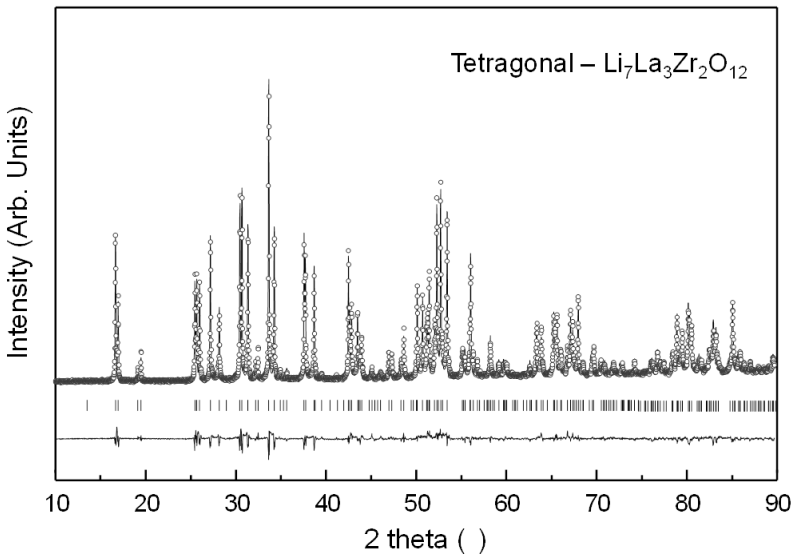

Figure 4.4. Observed (open circle), calculated (solid line), Bragg reflections (vertical lines) and difference (bottom) patterns for the calculated pattern from the x-ray powder diffraction data of tetragonal-$Li_7La_3Zr_2O_{12}$. (Rp = 0.09, wRp = 0.12 and X^2=4.56)

The XRPD pattern of the precursor material calcined at 973 K matches very well with that of the known cubic garnet-related phase $Li_5La_3Nb_2O_{12}$ (JCPDS card No. 84-1753). The lattice parameter is calculated to be a = 13.002Å (1). The crystal structure of the tetragonal garnet-related LLZO has been recently refined by Awaka et al. [17] using x-ray and neutron powder diffraction data is shown in Figure 4.5. The measured powder pattern for annealed sample at 1073 K harmonizes well with this tetragonal modification (space group $I4_1/acd$). The calculated lattice constants are a = 13.122Å (3) and c = 12.672Å (3) which are quite similar to the reported values (a = 13.134Å (4) and c = 12.663Å (8)) [17]. So, according to the XRPD analysis, there is a transition from cubic to tetragonal garnet-related phase which is also correlated by the exothermic peak at 997 K in the DTA. Further annealing of the precursor material at higher temperatures (from 1273 to 1500 K) was also studied but all attempts to synthesize the high temperature cubic garnet-related phase which was prepared by conventional solid-state route by Weppner et al. have failed yet [16]. The final product was identified as $La_2Zr_2O_7$ and the loss of lithium can be explained by the evaporation of the alkali metal at elevated temperatures.

Chemical Formula	$Li_7La_3Zr_2O_{12}$	$Li_7La_3Zr_2O_{12}$	$Li_7La_3Zr_2O_{12}$	$Li_7La_3Zr_2O_{12}$
Reaction Temperature	973 K	1073 K	1253 K	1500 K
Crystal System	Cubic	Tetragonal	Tetragonal	Cubic
Space Group	*Ia-3d*	$I4_1/acd$	$I4_1/acd$	*Ia-3d*
a (Å)	13.002(1) Å	13.122(3) Å	13.134(4) Å	12.9682(6) Å
c (Å)		12.672(3) Å	12.663(8) Å	
Reference	This Work	This Work	[17]	[16]

Table 4.1. Structural parameters of cubic-$Li_7La_3Zr_2O_{12}$ and tetragonal-$Li_7La_3Zr_2O_{12}$.

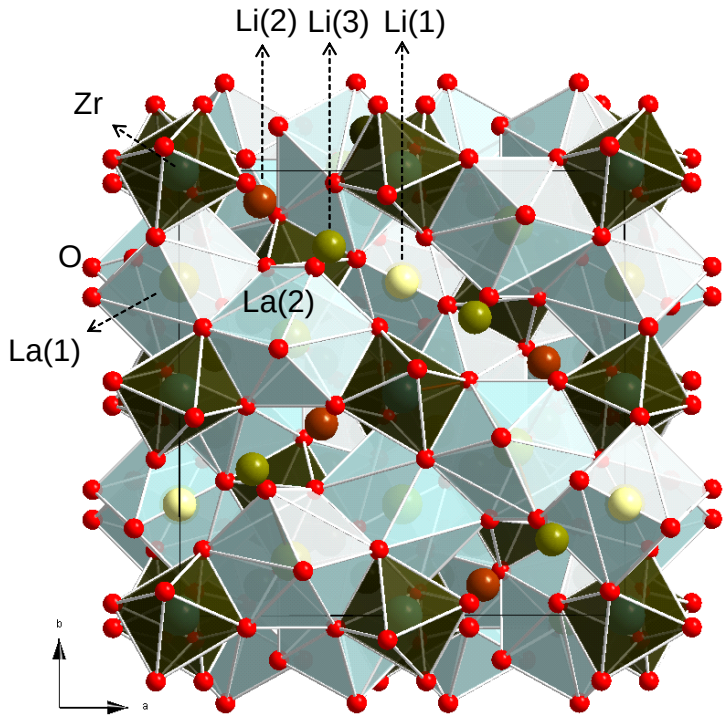

Figure 4.5. Crystal structure of tetragonal $Li_7La_3Zr_2O_{12}$ [17].

4.3.3. Powder Morphology

SEM micrographs of the LLZO sample calcined at different temperatures for 5 hours in air are shown in Figure 4.6. The intermediate phase at 923 K which is a mixture of $La_2Zr_2O_7$ and Li_2CO_3 shows very fine particles which are smaller than 100 nm (Figure 4.6a). The particle size of the LLZO calcined at 973 K is in the order of 300-500 nm (Figure 4.6b) appearing to be irregularly spherical or elliptical shaped. The grain size of the powders becomes larger as the calcination temperature is increased to 1073 and 1173 K. The particle sizes at 1073 K are ranging from 500 nm to 1 μm while those at 1173 K are in the order of 2 μm (Figure 4.6 c and d).

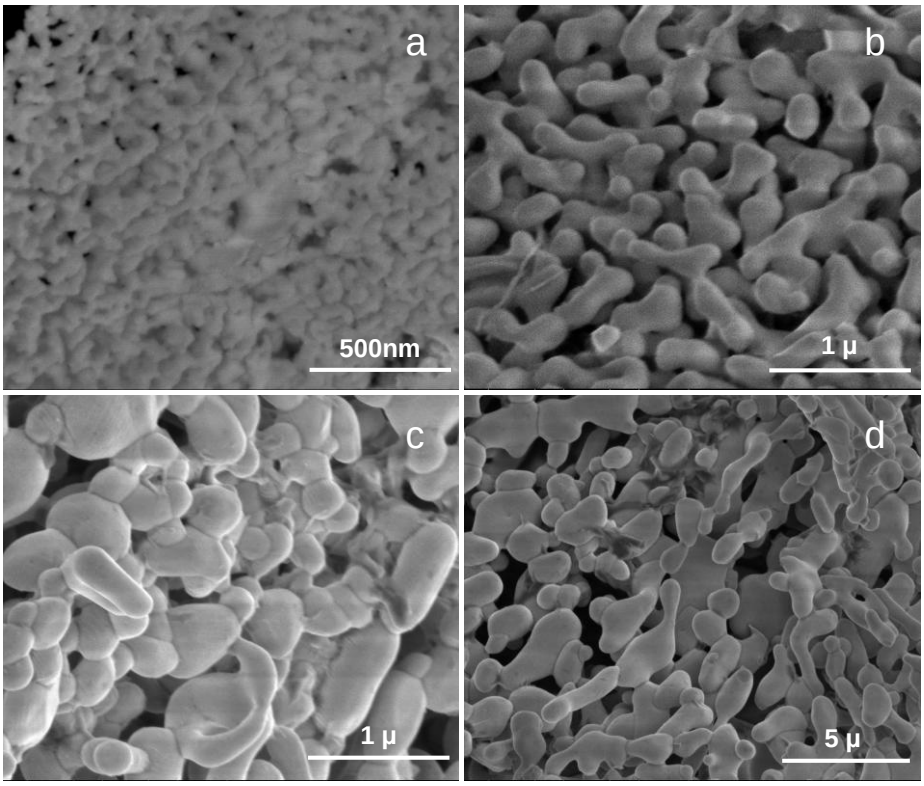

Figure 4.6. SEM micrographs of the LLZO powder precursors calcined at (a) 923 K, (b) 973 K, (c) 1073 K and (d) 1173 K in air atmosphere for 5h.

4.3.4. Lithium Ionic Conductivity

The lithium ionic conductivity of low temperature cubic garnet-related LLZO phase could not be investigated due to the phase transition to tetragonal modification at low temperatures (997 K) when sintering the pellet for densification. Later, this is also reported by Xie [19]. Typical Nyquist plot of the impedance spectrum for tetragonal $Li_7La_3Zr_2O_{12}$ with lithium ion blocking Au electrode at 290, 298, 343 K are shown in Figure 4.7. Each individual impedance spectra consists of pressed semicircle at high frequencies and a tail at low frequencies. The impedance plots were resolved in two different regions (high and low frequency) by Ivium Equivalent Circuit Analyzer. The compressed semicircles in the high frequency region can be attributed to the resistance of both bulk and grains boundaries which are not obviously separated from each other in every Nyquist spectrum, therefore the lithium ionic conduction properties of the sample

was evaluated by using the total conductivity. For every Nyquist spectrum at low frequency region, capacitative tail of the Au blocking electrode is observed and it indicates the ionic nature of the conduction in the studied compound. The solid lines in figure 4.7 represent the fitted data with an equivalent circuit ($R_{tot}Q_{tot}$)(Q_{el}) where R is the resistance, Q the constant phase element and the subscripts "tot" and "el" refer to total and electrode, respectively.

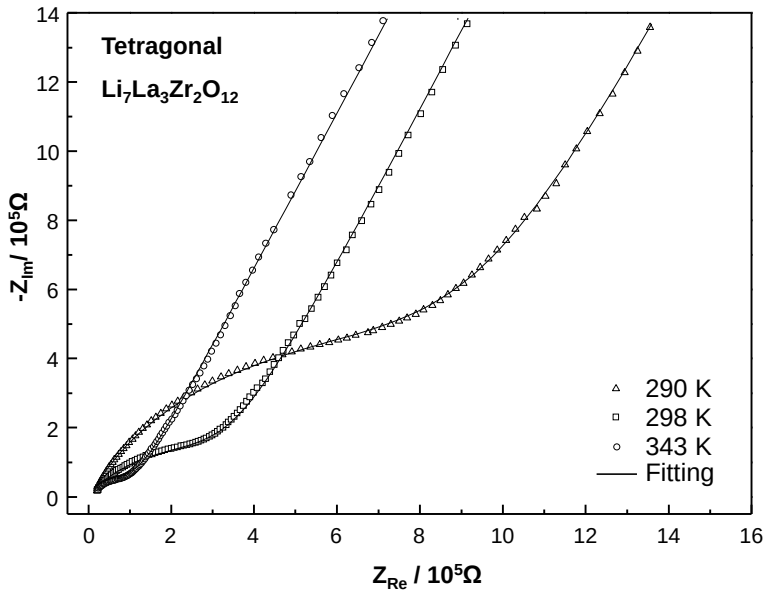

Figure 4.7. Nyquist plot (frequency range: 10Hz – 1MHz) of tetragonal LLZO prepared by sol – gel synthesis at 290, 298 and 343 K using lithium ion blocking Au electrodes. The solid lines were fitted with an equivalent circuit consisting of resistance-capacitance contribution of the solid electrolyte and capacitance contribution of the electrode ($R_{tot}Q_{tot}$)(Q_{el}) using Ivium Equivalent Circuit Analyzer.

The characteristic magnitudes of the bulk, grain boundary and total ion conduction of the tetragonal LLZO prepared by conventional solid-state method were found to be in the order of 10^{-6}, 10^{-7} and 10^{-7} S/cm, respectively, as reported by Awaka et al [17]. In our study, the magnitude of the ionic conductivity calculated from the fitting values is on the order of 10^{-7} S/cm, indicating that the grain boundary participates in the ionic

conduction with relatively high contribution to the total ionic conduction. The total ionic conductivity at 298 K obtained for sol-gel synthesized tetragonal LLZO is 3.12×10^{-7} S/cm, which is similar to the LLZO prepared by conventional solid-state reaction ($\sigma_{tot} \approx 4.16\times10^{-7}$ S/cm) [17].

The temperature dependence of the total ionic conductivity (Arrhenius plot) of tetragonal-LLZO prepared by sol-gel synthesis is shown in Figure 4.8 and can be expressed by an Arrhenius equation.

$$\sigma = \frac{A}{T}\exp\left(\frac{-E_a}{k_B T}\right) \qquad \textbf{4.1}$$

where σ is the ionic conductivity, T the absolute temperature, A the pre-exponential constant, k_B the Boltzmann constant and E_a is the activation energy for the ionic conductivity. E_a was determined from the slope of the log(σT) versus 1/T plot. The calculated E_a is 0.67 eV in the temperature range of 290-353 K.

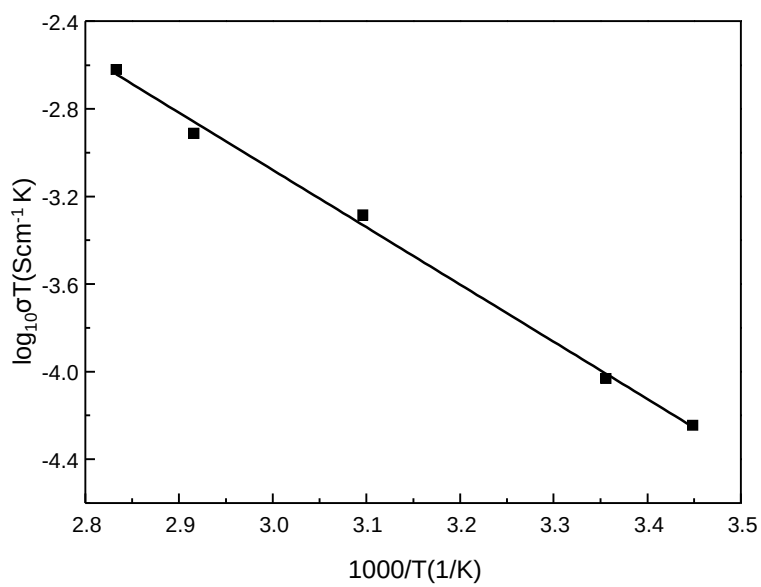

Figure 4.8. Arrhenius plot for total conductivity of tetragonal LLZO prepared by sol-gel synthesis

4.4. Conclusions

Polycrystalline powders of cubic and tetragonal modifications of $Li_7La_3Zr_2O_{12}$ with garnet-related type structure have been successfully synthesized by modified Pechini sol-gel processes in which citric acid was used as chelating agent and ethylene glycol as organic solvent. Cubic LLZO was prepared at very low temperature of 973 K and the unit cell parameter is a = 13.002Å (1) which is slightly higher than that of previously reported high temperature cubic garnet-related LLZO phase by Weppner et al. (a = 12.9682 (6) Å) [16]. The phase transition from cubic to tetragonal garnet-related type structure at about 997 K was confirmed by DTA analysis and XRPD measurements. The tetragonal LLZO was prepared at 1073 K which is comparatively lower than temperature conditions employed in conventional solid-state synthesis methods (1253 K) [17]. The unit cell parameters of the tetragonal phase are not significantly different from the bulk single crystal studies. The lithium ionic conductivity and the activation energy of the tetragonal garnet-related LLZO compound were calculated as $\sigma_{tot}=3.12 \times 10^{-7}$ S/cm at 298 K and $E_a=0.67$ eV in the temperature range 290-353 K. We believe that the presented LLZO synthesis by modified Pechini sol-gel route will open up new possibilities for the deposition of LLZO thin films with the desired crystal structure in solid-state lithium ion batteries.

4.5. References

[1] P.H.L. Notten, F. Roozeboom, R.A.H. Niessen, L. Baggetto, Adv. Mater. **2007**, 19, 4564.

[2] J.B. Bates, N.J. Dudney, D.C. Lubben, G.R. Gruzalski, B. S. Kwak, X. Yu, R. A. Zuhr, J. Power Sources **1995**, 54, 58.

[3] V. Thangadurai, W. Weppner, Ionics **2006**, 12, 81.

[4] A. R. J. West, Appl. Electrochem. **1973**, 3, 327.

[5] A. Kvist, A. Lunden, Z. Naturforsch. **1965**, 20a, 235.

[6] H. Y.-P. Hong, Mater. Res. Bull. **1978**, 13, 117.

[7] H. Aono, H. Imanaka, G. Y. Adachi, Acc. Chem. Res. **1994**, 27, 265.

[8] G. Y. Adachi, N. Imanaka, H. Aono, Adv. Mater. **1996**, 8, 127.

[9] H. Aono, E. Sugimoto, Y. Sadaoka, N. Imanaka, G. Adachi, J. Electrochem. Soc. **1989**, 136,

[10] G. C. Farrington, B. S. Dunn, J. L. Briant, Solid State Ionics **1981,** 3–4, 405.

[11] M. Itoh, Y. Inaguma, W. Jung, L. Chen, T. Nakamura, Solid State Ionics **1994**, 70, 203.

[12] V. Thangadurai, H. Kaack, W. Weppner, J. Am. Ceram. Soc. **2003**, 86, 437.

[13] V. Thangadurai, W. Weppner, Adv. Funct. Mater. **2005**, 15, 107.

[14] V. Thangadurai, W. Weppner, J. Am. Ceram. Soc. **2005**, 88, 411.

[15] V. Thangadurai, W. Weppner, J. Power Sources **2005**, 142, 339.

[16] R. Mrugan, V. Thangadurai, W. Weppner, Angew. Chem. Int. Ed. **2007**, 46, 7778.

[17] J. Awaka, N. Kijima, H. Hayakawa, J. Akimoto, J. Solid State Chem. **2009**, 182, 2046.

[18] J. Rodriguez-Carvajal, "FULLPROF", Laboratoire Le' on Brillouin (CEA-CNRS), France **2006.**

[19] H. Xie, Y. Li, J. B. Goodenough, Materials Research Bulletin **2012,** 47, 1229

Chapter 5.

Sol-Gel Synthesis and Lithium Ion Conduction Properties of Garnet-type $Li_5La_3Ta_2O_{12}$ and $Li_6BaLa_2Ta_2O_{12}$

Abstract

Highly lithium ion conductive garnet-type lanthanum lithium tantalite $Li_5La_3Ta_2O_{12}$ (LLTO) and barium lanthanum lithium tantalate, $Li_6BaLa_2Ta_2O_{12}$ (LLBTO), have been prepared by a modified sol-gel Pechini method from the appropriate mixtures of lithium carbonate, lanthanum oxide and tantalum ethoxide for LLTO and in addition to those barium carbonate was used for LLBTO. The thermal decomposition of the precursor powders were investigated by TG/DTA analysis. The LLTO and LLBTO precursor powders were annealed at various temperatures between 923 and 1123K for 6 hours in air. The transformation process from precursor powder to crystalline garnet-like phase was analyzed by X-ray powder diffraction (XRPD). The morphology of the powders annealed at various temperatures was investigated by Scanning Electron Microscopy (SEM). The resultant pelletized LLTO and LLBTO show a total Li-ion conductivity of 3.22×10^{-6} S/cm and 1.69×10^{-5} S/cm at 298 K respectively.

* The chapter has partially been published by I.Kokal, K.V. Ramanujachary, P.H.L. Notten, H.T. Hintzen, in Mater. Res. Bull. **2012**, 47, 1932

5.1. Introduction

Rechargeable lithium batteries with high energy density are required as power sources for portable electronic devices as well as for large-scale electrical power storage systems. One of the important problems is the safety due to the usage of flammable organic electrolytes in current batteries technologies. Solid-state-batteries with inorganic nonflammable solid lithium ion conductors used as electrolytes are one of the promising candidates to overcome safety problems [1-3]. Thus, solid lithium ion conductors have recently been under intense investigation with a wide range of chemical compositions and crystal structure types such as $Li_{10}GeP_2S_{12}$, Li_4SiO_4, Li_2SO_4, $Li_{14}ZnGe_4O_{16}$, $Li_{1+x}Ti_{2-x}M_x(PO_4)_3$ (M=Al, Sc, Y, La), Li–β–alumina and $Li_{0.34}La_{0.5}TiO_{2.98}$ with perovskite structure. Some of the reported ionic conductivities in these compounds are in the range of 10^{-2} and 10^{-7} S/cm [4-12].

In addition to the above mentioned compounds, new classes of compounds with garnet-type structure have attracted great interest as potential solid-state lithium ion conductors during the last few years. Compound series with the chemical formula $Li_5La_3M_2O_{12}$ (M=Nb, Ta), $Li_6ALa_2M_2O_{12}$ (A = Ca, Sr, Ba; M = Nb, Ta) and $Li_7La_3Zr_2O_{12}$ have been reported to exhibit high lithium ion conductivity ($\sigma_{bulk} \approx 10^{-4}$-$10^{-6}$ S/cm) among which $Li_6BaLa_2M_2O_{12}$ showed the highest bulk ionic conductivity of $4x10^{-5}$ S/cm at 298K [13-20]. In addition to their high ionic conductivities, garnet compounds show high stability against (electro) chemical reactions with commonly used intercalation materials for battery applications [21-22]. Recently, investigation on garnet type solid lithium ion conductors has been extended to the synthesis of nano–crystalline compounds at relatively low temperatures and reaction time with accurate control of the composition by sol-gel synthesis. The resultant small and uniform particle size powders enhance the sintering efficiency at relatively lower temperatures, thereby improving the bulk density of ceramics [23-26].

In this chapter, we investigated the possibility of the synthesis of the $Li_5La_3Ta_2O_{12}$ (LLTO) and $Li_6BaLa_2Ta_2O_{12}$ (LLBTO) with garnet type structure through the modified-Pechini method by using citric acid as chelating agent. These materials were investigated by means of X-ray diffraction studies, thermal analysis and ionic conductivity measurements and the results are discussed in detail.

5.2. Experimental Method

5.2.1. Synthesis of $Li_6BaLa_2Ta_2O_{12}$

Polycrystalline powders of $Li_5La_3Ta_2O_{12}$ and $Li_6BaLa_2Ta_2O_{12}$ were obtained by using Li_2CO_3 (Alfa, 99.9%), La_2O_3 (Alfa 99.9%, dried overnight at 1273K in air atmosphere), $BaCO_3$ only for LLBTO (Sigma Aldrich 99.9%), $Ta(OC_2H_5)_5$ (Sigma Aldrich 99.98%), citric acid as an organic complexing agent, and ethylene glycol as organic solvent. The stoichiometric ratios for LLTO and LLBTO are 5.5:3:4:28:14 and 6.6:2:2:4:28:14, respectively. A slight surplus (ca. 10%) of Li_2CO_3 is necessary for the synthesis of both compounds to compensate for losses due to the volatility of lithium. Oxides and carbonates were first dissolved in diluted HNO_3, then $Ta(OC_2H_5)_5$ was added and the pH value of the solution was adjusted below 3 by adding HNO_3 to avoid precipitation. Both solutions were mixed well and highly concentrated citric acid and ethylene glycol were then added. The obtained solutions were heated to 323 K and stirred vigorously for 3 hours in air. The mixtures were evaporated at 373 K until a yellowish transparent gel was obtained which was subsequently dried and decomposed at 473 K for 24 hours in air to yield a highly reactive black precursor powder for both LLTO and LLBTO. The precursor product was ground well and calcined at temperatures between 923 and 1123 K for 6 hours in air to obtain $Li_5La_3Ta_2O_{12}$ and $Li_5La_2BaTa_2O_{12}$ as white polycrystalline powders.

5.2.2. Characterization

Thermal analysis (TG/DTA) using a Mettler Toledo TGA/SDTA 851 instrument was carried out on precursor powders in 70 μl Al_2O_3 crucibles from 300 to 1300 K with a heating rate of 5 K/min in flowing air (50 ml/min). X-ray powder diffraction (XRPD) analysis was performed to investigate the phase-purity and crystal structure of the resulting powders. Data were collected at room temperature with a Bruker Enduar D4 diffractometer using CuKα radiation in the 2 theta range 5° to 90° with a step size of 0.01° and a counting time of 1 second. Structural refinements of the resulting compounds were performed with the FullProf software [27]. The morphology of the powder materials was investigated by scanning electron microscopy using a Quanta 3D FEG instrument (FEI Company). Ionic conductivity measurements of pelletized samples were conducted using a potentiostat with a frequency response analyzer (Ivium Stat) operating at 100 mV constant potential within the frequency range of 10 Hz to 1 MHz and at various temperatures in the range of 290-343 K in argon atmosphere. The pelletized samples were prepared by pressing the powder samples and sintering them at 1173 K for 4h. The sintered pellets were polished (≈0.1 cm in thickness with an area of ≈ 1.13 cm^2 for LLTO and ≈ 0.29 cm^2 for LLBTO) then coated with gold by applying a gold paste which was cured at 923 K in air to form the ionically blocking electrodes.

5.3. Results and Discussion

5.3.1. Thermal Analysis

Figure 5.1a and 1b show the TG/DTA curves for the precursor powder of LLTO and LLBTO dried at 473 K in flowing air atmosphere. The TG profiles for both materials are similar up to 900 K and indicated that weight loss occurs mainly between 500 and 900 K accompanied with different exothermic effects which were recorded at about 740 and 787 K for LLTO and 570, 750 and 815 K for LLBTO in the DTA profile. The broad

exothermic peaks and the almost 80 % weight loss in the TG can be ascribed to the degradation of residual organics and the decomposition of the precursor garnet-type LLTO with no further significant weight loss above 900 K. This is indicating that the transformation of the precursor to oxides starts above that temperature. The small exothermic peak at around 970 K is attributed to crystallization of the LLTO phase which is also confirmed by XRPD analyses.

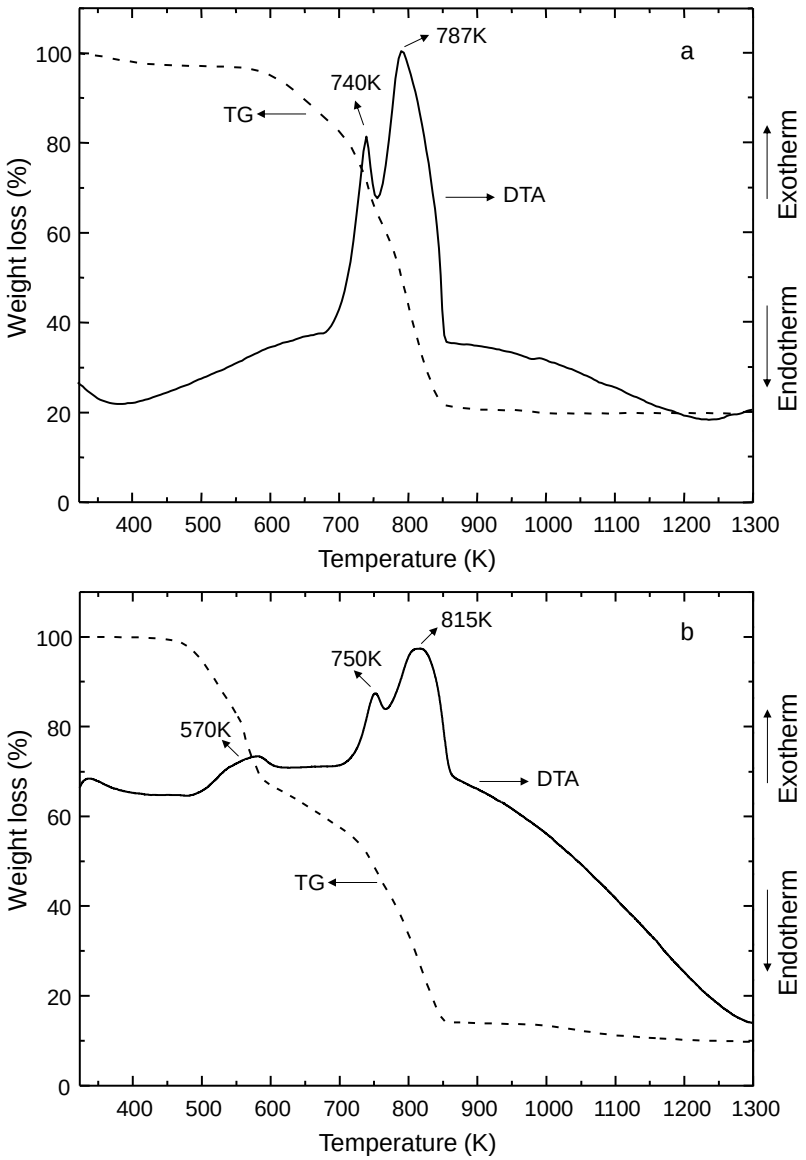

Figure 5.1. TG/DTA curves of the dried precursor LLTO **(a)** and LLBTO **(b)** powder obtained by sol-gel method.

Whereas in the case of LLBTO, 80 % weight loss in the TG can be ascribed to the degradation of residual organics and the decomposition of the precursor garnet-type $Li_5La_3Ta_2O_{12}$ and $BaCO_3$ is also supported by the XRPD analysis. It is discussed in detail in the next section. We observe a small weight loss between 1000 and 1100 K indicating that the decomposition of $BaCO_3$ followed by a reaction with garnet-type $Li_5La_3Ta_2O_{12}$ in the TG curve of LLBTO. The decomposition of $BaCO_3$ and crystallization of the LLBTO phase are also verified by XRPD analyses.

5.3.2. X-ray Diffraction

Figure 5.2 and 5.3 show the XRPD patterns after calcination of LLTO and LLBTO precursor powders respectively at 923, 973, 1073 and 1173 K temperatures for 6 hours reaction time. The diffraction peaks of the LLTO precursor powder calcined at 923K correspond to $LiLa_2TaO_6$ which is another phase in the lithium-lanthanum-tantalum system. The XRPD patterns at 973 K and higher exhibit the reflections belonging to the cubic garnet-type LLTO structure. Therefore the precursor is completely transformed into garnet-type LTO phases at ≥ 973 K. The diffraction patterns of the LLBTO precursor powders calcined at 923 and 973 K were indexed and it is found to support the presence of a mixture of cubic garnet type compound (with a lattice constant a = 12.812(3)Å) and $BaCO_3$. The corresponding reflections and lattice constants are very similar to $Li_5La_3Ta_2O_{12}$ which was previously studied and refined from single crystal x-ray analysis (a = 12.806 Å) [19]. According to our results in this chapter as well as the results of Gao et al. [24] the sol-gel synthesis of garnet-type $Li_5La_3Ta_2O_{12}$ could only be obtained at temperatures >≥ 973K and the products annealed below this temperature was correspond to $LiLa_2TaO_6$. This study on LLBTO however shows that the addition of barium to lithium-lanthanum-tantalum-oxide system facilitates the formation of the garnet phase $Li_5La_3Ta_2O_{12}$ at lower temperatures. The XRPD patterns of the precursors treated at temperature 1073K and higher, exhibit the reflections belonging to the cubic

garnet-type LLBTO structure. From these observations, we deduce that the precursor is transformed into garnet-type LLBTO phases at ≥1073 K. The XRPD patterns of compounds calcined at 1073 K were indexed by using fullprof software and they appear to match very well with that of known cubic garnet type $Li_6SrLa_2Ta_2O_{12}$ [17]. The difference between the experimental and calculated pattern are illustrated in Figure 5.4. The calculated lattice constant was determined a = 12.995(2) Å is in good agreement with the previously reported value (a = 13.001 Å) [20].

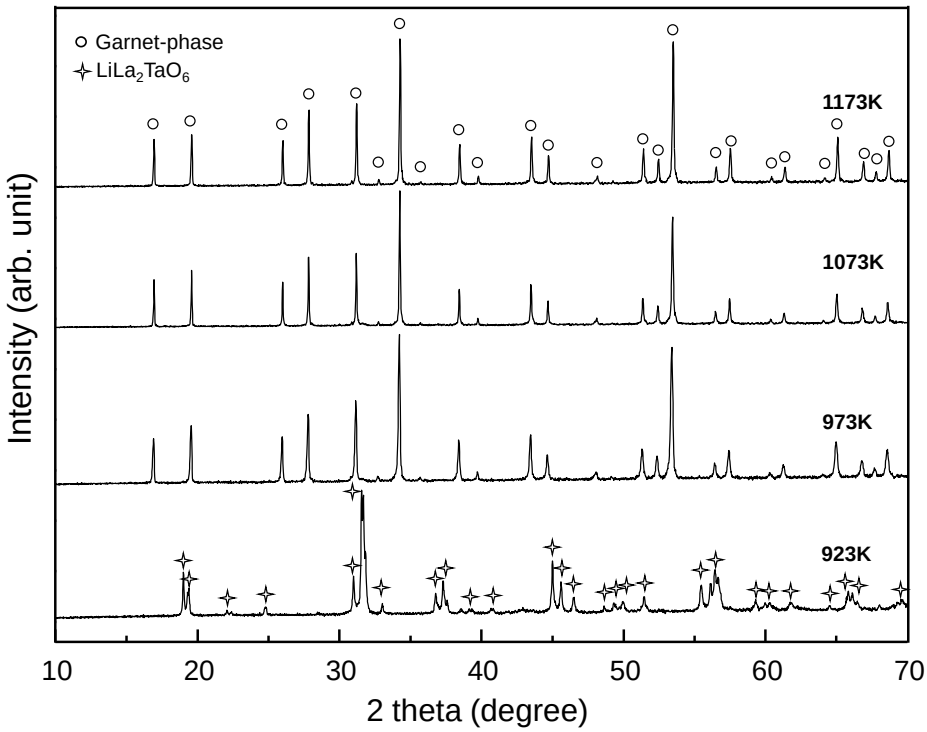

Figure 5.2. XRPD patterns of the LLTO precursors calcined at 923, 973, 1073 and 1173 K.

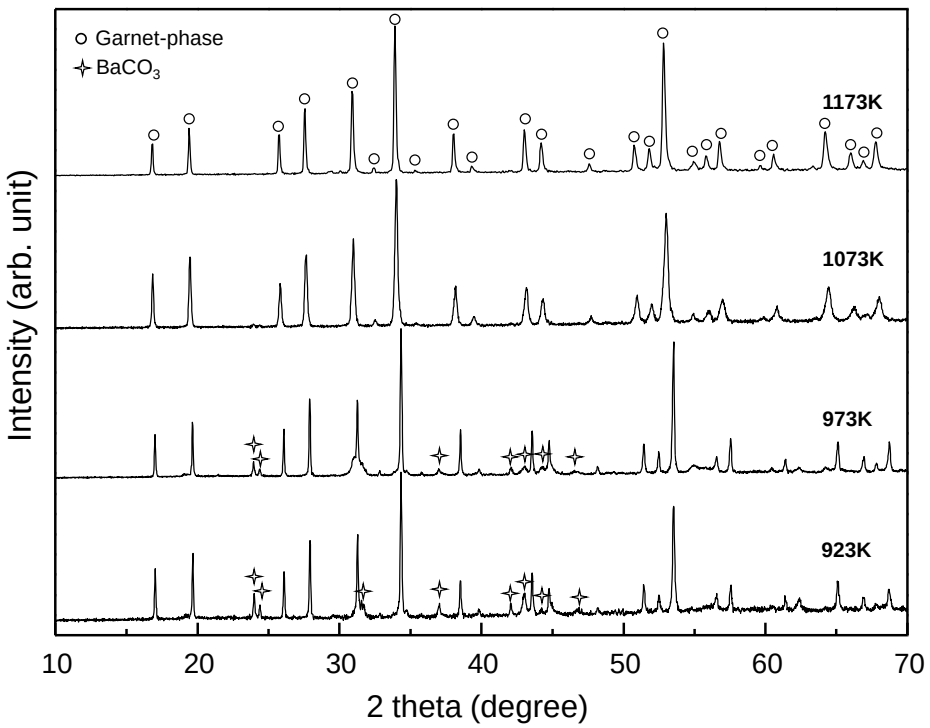

Figure 5.3. XRPD patterns of the LLBTO precursors calcined at 923, 973, 1073 and 1173 K.

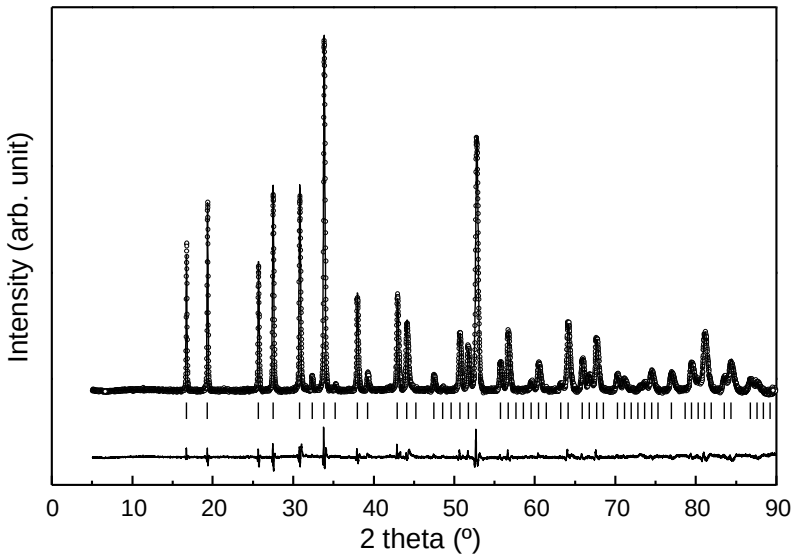

Figure 5.4. Observed (open circle), calculated (solid line), Bragg reflections (vertical lines) and difference (bottom patterns) for the calculated from X-ray powder diffraction data of LLBTO.

Furthermore our results show that a pure garnet-type LLBTO phase can be obtained at 1073 K in 6 hours for the material prepared by the modified Pechini method. The reaction temperatures as well as the calcination time of LLTO and LLBTO are substantially lower (200 K and 7 hours, respectively) compared to material made in the conventional solid-state synthesis route [20]. The preparation of LLTO and LLBTO powders by modified Pechini method showed the possibility of a pure phase formation using an organic and inorganic mixture precursor solution.

5.3.3. Morphology of $Li_5La_3Ta_2O_{12}$ and $Li_6BaLa_2Ta_2O_{12}$

Figure 5.5 and 5.6 shows the SEM micrographs of the LLTO and LLBTO powder sample calcined at different temperatures for 6 hours in air. The samples calcined at 923 K shows the presence of very fine particles which are in the order of 200 nm (Figure 5a and 6a). The particle size of the samples calcined at 973 K is in the order of micron and appears to be consistent with an inter-growth of originally smaller irregular spherical particles into elliptical particles as shown in Figure 5b and 6b. With this coalescence the grain size of the powders becomes larger as the calcination temperature has increased to 1073 and 1173 K. The particle sizes are around 2 micron at 1073 K for LLTO and they are in range from 2 - 5 μm for LLBTO while those sintered at 1173 K are in the order of 5 - 10 μm for LLBTO and slightly smaller particle were obtained for LLTO at that temperature (Figure 5.5c and 5.6c).

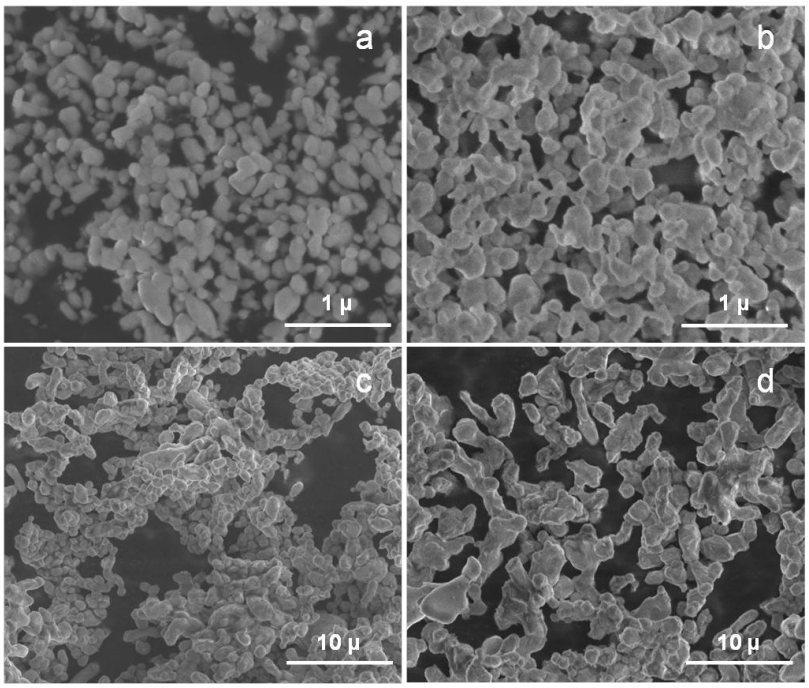

Figure 5.5. SEM micrographs of the LLTO powder precursors calcined at (a) 923K, (b) 973K, (c) 1073K, and (d) 1173K in air atmosphere for 6 hours.

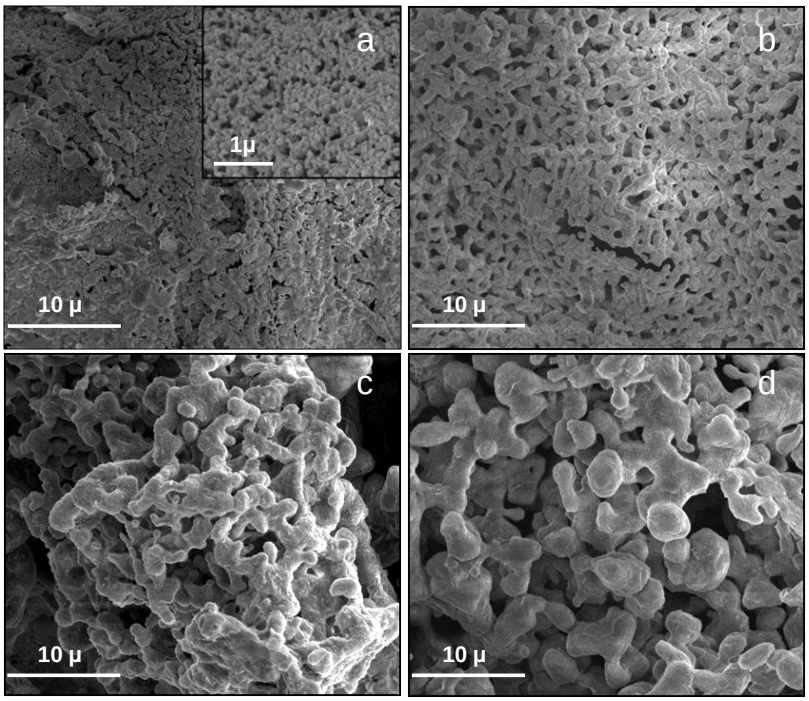

Figure 5.6. SEM micrographs of the LLBTO powder precursors calcined at (a) 923 K, (b) 973 K, (c) 1073 K, and (d) 1173 K in air atmosphere for 6 hours

5.3.4. Lithium ion conductivity of $Li_5La_2Ta_2O_{12}$ and $Li_6BaLa_2Ta_2O_{12}$

Figure 5.7 and 5.8 also demonstrates the total Li-ion conductivities of LLTO and LLBTO as a function of 1/T. The temperature dependency of the total ionic conductivities can be expressed by the Arrhenius equation $\sigma=A/T\exp(-E_a/(k_BT))$, where is A is the pre-exponential parameter, Ea the activation energy constant, k_B the Boltzmann constant and T the absolute temperature. The activation energies were estimated to be E_a=0.33 eV for LLTO and E_a=0.40 eV for LLBTO from the slope of log(σT) versus 1/T plot in the temperature range of 290-343 K.

The inset in figure 5.7 presents the Nyquist plot of the impedance spectrum for the pelletized sample of LLTO synthesized at 973 K with a Li blocking Au electrode at 298 K and the inset in figure 5.8 shows the Nyquist plot of the impedance spectrum for LLBTO synthesized at 1073 K with a Li blocking Au electrode at 298 K

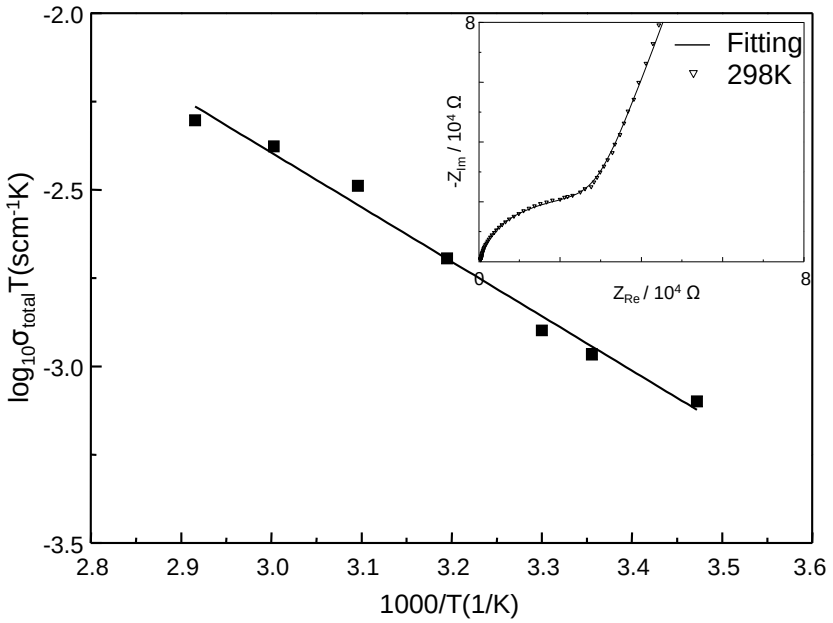

Figure 5.7. Arrhenius plot for total (bulk and grain boundry) lithium ion conductivity of LLTO prepared by sol-gel synthesis Inset: Nyquist plot (frequency range 10 Hz-1 MHz) of LLTO at 298 K using lithium ion blocking Au electrode.

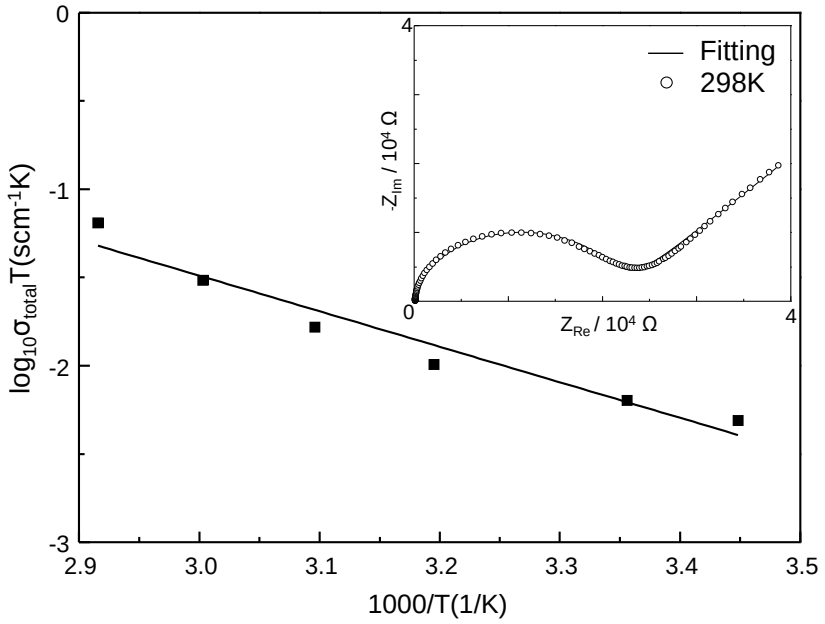

Figure 5.8. Arrhenius plot for total (bulk and grain boundry) lithium ion conductivity of LLBTO prepared by sol-gel synthesis. Inset: Nyquist plot (frequency range 10 Hz-1 MHz) of LLBTO at 298 K using lithium ion blocking Au electrode. The solid line was fitted with an equivalent circuit consisting of the resistance-capacitance contribution of solid electrolyte and the capacitance contribution of the electrode $(R_{tot}Q_{tot})(Q_{el})$ using Ivium Equivalent Analyzer.

5.4. Conclusions

Polycrystalline powders of $Li_5BaLa_2Ta_2O_{12}$ and $Li_5BaLa_2Ta_2O_{12}$ with garnet-related type structure have been successfully synthesized using a modified Pechini sol-gel processes in which citric acid was used as chelating agent and ethylene glycol as organic solvent. The formation temperature for pure garnet-type LLTO was found to be 973 K whereas LLBTO phase can only be synthesized at and above 1073 K as confirmed by TG\DTA analysis and XRPD measurements. Due to the finer particle size of the precursor materials, the reaction temperatures of the above mentioned compounds with the sol-gel synthesis route are substantially lower (≈ 200 K) than the conventional solid-state synthesis route. Our findings enable one to obtain pure as well as significantly smaller sized garnet phases at lower temperatures in those compounds with slightly higher

total lithium ion conductivity. We believe that both LLTO and LLBTO synthesis by a modified Pechini sol-gel route at low temperatures are promising in reducing the grain boundary contributions and hence higher sintering efficiency. Finally, wet chemical methods such as those reported here will open up new possibilities for the deposition of thin films of garnets for solid-state lithium ion batteries and designing novel electrolyte systems with three dimensionally ordered structures.

5.5. References

[1] P.H.L. Notten, F. Roozeboom, R.A.H. Niessen, L. Baggetto, Adv. Mater. **2007**, 19, 4564.

[2] L. Bagetto, R.A.H. Niessen, F. Roozeboom, P.H.L. Notten, Adv. Funct. Mater. **2008**, 19, 1057.

[3] V. Thangadurai, W. Weppner, Ionics **2006**, 12, 81.

[4] N.Kamaya, K. Homma, Y. Yamakawa, M. Hirayama, R. Kanno, M. Yonemura, T. Kamayima, Y. Kato, S. Hama, K. Kawamoto, A. Mitsui, Nature Materials **2011**, 10, 682.

[5] A. R. J. West, Appl. Electrochem. **1973**, 3, 327.

[6] A. Kvist, A.Lunden, Z. Naturforsch. **1965**, 20a, 235.

[7] H. Y.-P. Hong, Mater. Res. Bull. **1978**, 13, 117.

[8] H. Aono, H. Imanaka, G. Y. Adachi, Acc. Chem. Res. **1994**, 27, 265.

[9] G. Y. Adachi, N. Imanaka, H. Aono, Adv. Mater. **1996**, 8, 127.

[10] H. Aono, E. Sugimoto, Y. Sadaoka, N. Imanaka, G. Adachi, J. Electrochem. Soc. **1989**, 136, L590.

[11] G. C. Farrington, B. S. Dunn, J. L. Briant, Solid State Ionics **1981**, 3–4, 405.

[12] M. Itoh, Y. Inaguma, W. Jung, L. Chen, T. Nakamura, Solid State Ionics **1994**, 70, 203.

[13] V. Thangadurai, H. Kaack, W. Weppner, J. Am. Ceram. Soc. **2003**, 86, 437.

[14] V. Thangadurai, W. Weppner, Adv. Funct. Mater. **2005**, 15, 107.

[15] V. Thangadurai, W. Weppner, J. Am. Ceram. Soc. **2005**, 88, 411.

[16] J. Percival, P. R. Slater, Solid State Commun. **2007**, 142, 335.

[17] R. Mrugan, V. Thangadurai, W. Weppner, Angew. Chem. Int. Ed. **2007**, 46, 7778.

[18] J. Awaka, N. Kijima, H. Hayakawa, J. Akimoto, J. Solid State Chem. **2009**, 182, 2046.

[19] E.J. Cussen, Chem. Comm. **2006**, 4, 437.

[20] J. Awaka, N. Kijima, Y. Takahashi, H. Hayakawa, J. Akimoto, Solid State Ionics **2009**, 180, 602.

[21] V. Thangadurai, W. Weppner, J. Power Sources **2005**, 142, 339.

[22] M. Kotobuki, K. Kanamura, Y. Sato, T. Yoshida, J. Power Sources, **2011**, 196, 7750.

[23] I. Kokal, M. Somer, P.H.L. Notten, H.T. Hintzen, Solid State Ionics **2011**, 185, 42.

[24] Y. X. Gao, X. P. Wang, W. G. Wang, Q. F. Fang, Solid State Ionics **2010**, 181, 33.

[25] Y. X. Gao, X. P. Wang, W. G. Wang, Q. F. Fang, Solid State Ionics **2010**, 181, 1415.

[26] N. Janani, S. Ramakumar, L. Dhivya, C. Deviannapoorani, K. Saranya, R. Murugan, Ionics. (online available)

[27] J. Rodriguez-Carvaial, FULLPROF, Laboratoire Le' on Brillouin(CEA-CNRS), France **2006**.

Chapter 6.

Preparation and Characterization of Three Dimensionally Ordered Macroporous $Li_5La_3Ta_2O_{12}$ by Colloidal Crystal Templating for All-Solid-State Lithium-ion Batteries

Abstract

Three dimensionally ordered macroporous (3DOM) membranes of $Li_5La_3Ta_2O_{12}$ (LLTO) for all-solid-state lithium ion batteries were prepared by using colloidal crystal templating of mono dispersed polystyrene (PS) spheres combined with sol-gel synthesis of LLTO precursor. During the sol-gel synthesis, the appropriate mixtures of lithium acetate, lanthanum nitrate hexahydrate and tanthalum ethoxide were dissolved in two different solvents to prepare garnet-type lithium lanthanum tantalate, $Li_5La_3Ta_2O_{12}$ (LLTO). Various sizes of mono dispersed (1, 3 and 5 μm) PS beads were used as a template to investigate the size effect of the template on the network formation of LLTO membranes. The thermal decomposition of the precursor solutions was investigated by TG analysis and the transformation process from precursor solutions, which are added onto the PS template, to crystalline garnet-related phase, were analyzed by X-ray powder diffraction (XRPD). The morphology of the PS templates as well as the 3DOM garnet membranes were investigated by Scanning Electron Microscopy (SEM). The templates made from 5 μm PS spheres were found to be the most suitable template to obtain 3DOM membranes of garnet-type lithium lanthanum tantalate.

6.1. Introduction

Rechargeable lithium ion batteries are nowadays widely used as energy power supplies in various electronic devices due to their high energy density [1]. However, the conventional rechargeable batteries contain hazardous and flammable organic liquid electrolytes, making them potentially unsafe and reducing the cycle life due to formation of an irreversible solid electrolyte interface [2]. For these reasons, replacement of the liquid electrolyte with a safer and stable solid electrolyte is necessary to improve the safety by preventing the risk of liquid electrolyte leakage and improving the cycling stability. Research efforts were directed towards finding suitable solid electrolytes for lithium ion batteries with high lithium ion conductivity as well as good chemical stability with commonly used intercalation materials for battery applications [3]. A wide range of compounds with different crystal structure types has been investigated, such as Li_4SiO_4, Li_2SO_4, $Li_{14}ZnGe_4O_{16}$, $Li_{1+x}Ti_{2-x}M_x(PO_4)_3$ (M = Al, Sc, Y, La), Li–β–alumina and $Li_{0.34}La_{0.5}TiO_{2.98}$ with perovskite crystal structure. Some of the reported ionic conductivities are in between 10^{-3} and 10^{-7} S/cm [4-10]. In addition to the above mentioned compounds, new classes of compounds with garnet-type structure have attracted great interest as potential solid-state lithium ion conductors in the last few years. Compound series with the chemical formula $Li_5La_3M_2O_{12}$ (M = Nb, Ta), $Li_6ALa_2M_2O_{12}$ (A = Ca, Sr, Ba; M = Nb, Ta) and $Li_7La_3Zr_2O_{12}$ have been reported with high lithium ion conductivity ($\sigma_{bulk} \approx 10^{-4}$-$10^{-6}$ S/cm) and good chemical stability towards electrode materials, especially metallic lithium electrodes compare with perovskite and NASICON-type electrolytes [11-15].

On the other hand, using ceramic electrolytes in solid-state lithium ion batteries causes a problem due to the poor contact between the solid electrolyte and the active electrode material which causes a high internal resistance [16]. Recently, we have investigated the synthesis of nanocrystalline garnet compounds at relatively low temperatures by sol-gel

synthesis to reduce the internal resistance in those materials [17, 18]. Dokko et al. proposed and reported the $Li_{0.35}La_{0.55}TiO_3$ (LLT) perovskite-type solid electrolyte with three dimensionally ordered macroporous (3DOM) structure to enlarge the contact area between the solid electrolyte and electrode material [19]. One of the short comings of this study was that LLT undergoes a reduction of Ti^{4+} to Ti^{3+} during the contact with lithium metal and since LLT has 3D lithium ion mobility only above 400 K [20], perovskite-type lithium ion conductor is not favorable in those 3DOM networks.

In the study reported in this chapter, we investigated the preparation of 3DOM garnet-type LLTO by PS colloidal crystal templating using two different precursor solutions. Absolute ethanol (EtOH) was used as a solvent in the preparation of the first precursor solution and the other contains acetic acid (HAc) and ethylene glycol mixture as solvent. Those two precursor solutions were employed on three types of template prepared with different sizes mono-dispersed spherical colloidal PS particles (1, 3, 5 μm). The decomposition behavior of the solutions added on PS templates was characterized by TG analysis. The effect of the precursor solution and the PS templates on the 3DOM garnet-type LLTO morphology was characterized by SEM analysis and the crystal structure of the electrolyte materials were characterized by XRD analysis.

6.2. Experimental Method

6.2.1. Preparation of Polystyrene (PS) Colloidal Crystal Templates

Colloidal crystal templates of PS spheres were formed using gravitational settling in combination with evaporation to prepare the 3DOM $Li_5La_3Ta_2O_{12}$ solid electrolyte combined with the sol-gel method. For gravitational settling in combination with evaporation, 2 ml water suspensions of 50 mg PS/ml (Sigma Aldrich) with various mono-dispersed PS bead sizes (1, 3, 5 μm) were prepared and placed inside a syringe (20 ml PE/PP BD Biscardit II) that was cut in half. Those were left to dry overnight at

333 K under atmospheric conditions. Finally, the PS templates were removed by pushing the plunger of the syringe.

6.2.2. Preparation of 3DOM $Li_5La_3Ta_2O_{12}$

Sol-gel synthesis of $Li_5La_3Ta_2O_{12}$ was done using two different solvents. In the first solution, lithium(I) acetate (99.95%, trace metal basis Aldrich Chemistry) was dissolved in ethanol (99.9%, Technisolve) whereas in the second solution it is dissolved in ethylene glycol (EG) (99% Merck KGaA) and glacial acetic acid (HAc) (100% Merck KGaA) used as chelating agent while stirring and heating at 343 K for 1 hour under reflux conditions. Lanthanum(III) nitrate hexahydrate (99.999%, trace metal basis, Aldrich Chemistry) and tantalum(V) ethoxide (99.999%, Alfa Aesar) were added with molar ratio of (Li:La:Ta) 6:3:2 in both solutions. A 10% excess amount of lithium was used to compensate for lithium evaporation. The whole mixture was stirred and heated at 343 K for 1h under reflux conditions. Solvent evaporation was induced by heating the mixture to 393 K without refluxing. The concentration of the solutions was approximately 0.1 molar upon evaporating of the solvents, the mixture was left to cool at room temperature, yielding a low viscosity transparent precursor solution. The precursor solution were added to the previously obtained PS templates using vacuum impregnation. Four drops of solution were added to the PS deposits after which the sample was heated to 303 K for 15 minutes under vacuum. This was repeated three times. Finally, the samples were heated at 973 K for 1 hour under static air atmosphere to decompose the PS particles and to form the solid electrolyte.

6.2.3. Characterization

Thermogravimetric analysis (TGA) using a Mettler Toledo TGA/SDTA 851 instrument was carried out on PS template filled with precursor solution in 70 μl Al_2O_3 crucibles from 300 to 1273 K with a heating rate of 5 K/min in flowing air (50 ml/min). X-ray

powder diffraction (XRPD) analysis was performed to investigate the phase purity and crystal structure of the resulting porous membranes. Data were collected at room temperature with a Bruker Enduar D4 diffractometer using CuK_{α} radiation in the 2 theta range 5° to 90° with a step size of 0.01° and a counting time of 1 second. The morphology of the PS templates as well as the porous membranes was investigated by Scanning Electron microscopy (SEM) using a Quanta 3D FEG instrument (FEI Company).

6.3. Results and discussion

6.3.1. Formation of Colloidal Crystal Templates

Mono-dispersed polystyrene spheres with 1, 3 and 5 μm bead size were used to form the crystal templates by using gravitational settling in combination with evaporation to prepare the 3DOM $Li_5La_3Ta_2O_{12}$ solid. Figure 6.1 shows the SEM pictures of the templates prepared by using various PS sphere sizes. It can be seen in the SEM micrographs that long range ordered templates with some stacking faults was prepared for further manipulations.

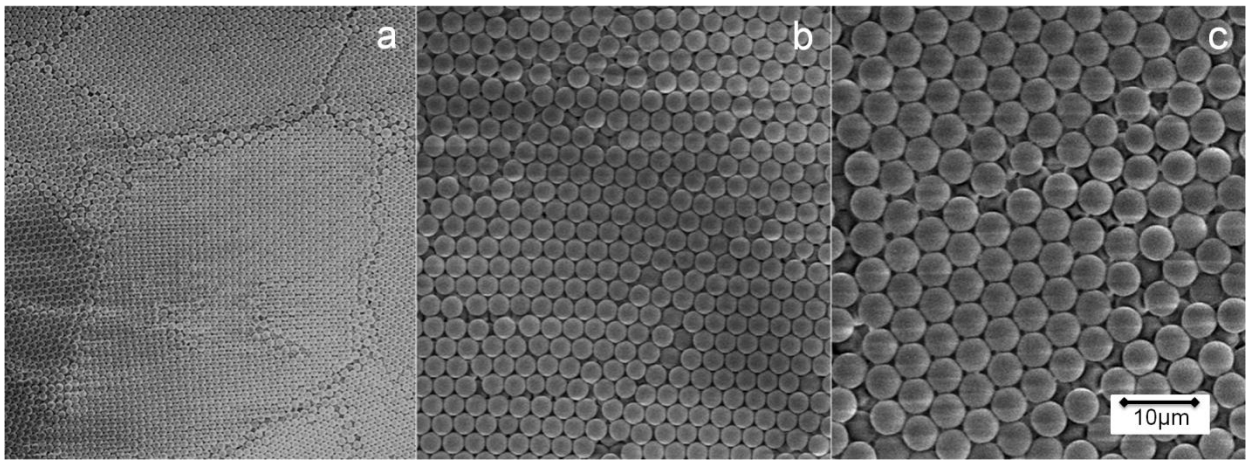

Figure 6.1. SEM image of mono-dispersed PS templates **(a)** 1 μm, **(b)** 3 μm and **(c)** 5 μm prepared by gravitational settling in combination with evaporation.

6.3.2. Decomposition of PS templates filled with precursor solution

PS templates were filled with garnet sol-gel precursors and dried at room temperature in a vacuum chamber. The dried samples were annealed under flowing air from room temperature to 1200 K at a rate of 5K/min. During the removal of polystyrene templates and the crystallization of the garnet phase, the reaction mixtures undergo several processes, such as combustion of the PS template, decomposition of precursor solution, and oxidation. After the addition of precursor solutions onto the templates, the removal of PS and the formation of garnet compound were monitored by thermal analysis (TG/DTA) which is shown in figure 6.2. On the basis of thermal analysis of the sample prepared using HAc/EG as a solvent, the weight decrease between 300-400 K and that between 450-600K are assigned to loss of residual solvents, HAc and EG, respectively. While, when PS is impregnated with EtOH containing precursor, the solvent evaporation is minor due to the low temperature evaporation of EtOH. At around 600K, the weight loss accelerates for both precursor solutions, till it reaches 650K due to combustion of the polystyrene. A slow and steady weight loss from 650 K to 950 K can be attributed to decomposition and oxidation of residual organics from the sol-gel precursors. There is no significant weight loss higher than 950 K for both types of precursors which is indicating that the transformation of the precursor to oxides starts above this temperature followed by crystallization of pure LLTO phase. This has also been verified by XRPD analyses.

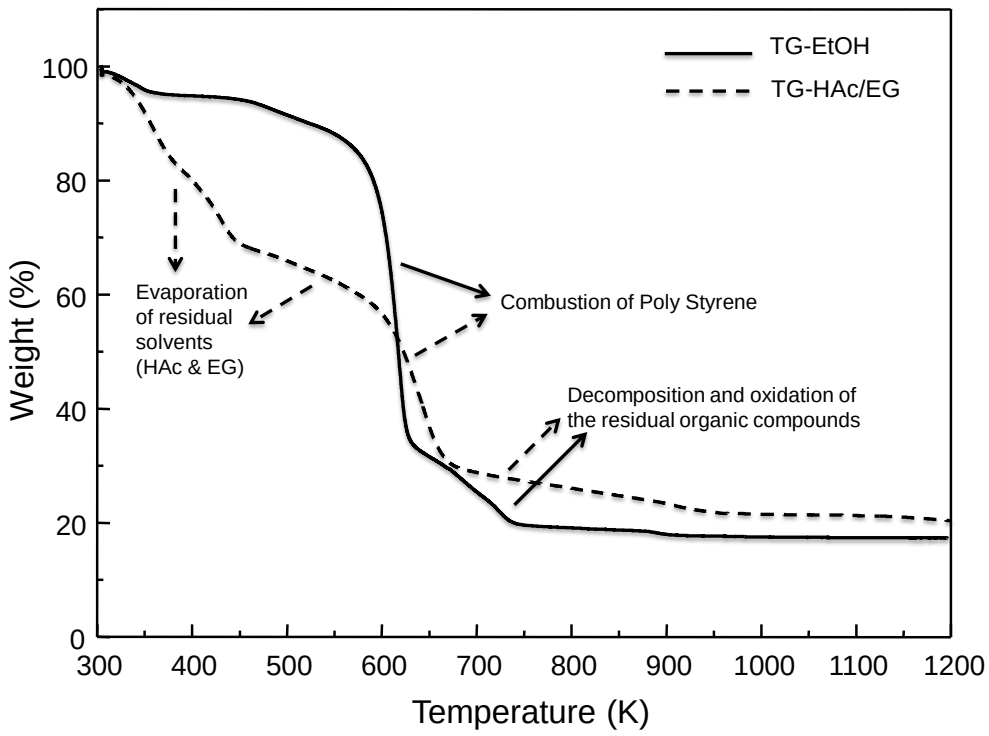

Figure 6.2 TGA curve of PS template combined with garnet precursor solution based on EtOH (solid line) and HAc/EG mixture (dashed line) in flowing air atmosphere.

6.3.3. Phase Formation

Figure 6.3 shows the XRPD patterns of calcined 3DOM LLTO prepared with two different solutions at 973 K. The PS template was filled with precursor solutions separately and they are annealed at 973 K for 1 hour reaction time. The diffraction peaks of the 3DOM LLTO samples at 973 K match very well with those of the corresponding garnet phase $Li_5La_3Ta_2O_{12}$ without any other additional peaks. The 3DOM LLTO prepared using HAc/EG have better crystallinity and larger crystallite size than the EtOH used sample as can be seen from the sharper X-ray diffraction peaks. These results show that the precursor solutions are completely transformed into garnet-type LLTO phases at 973 K.

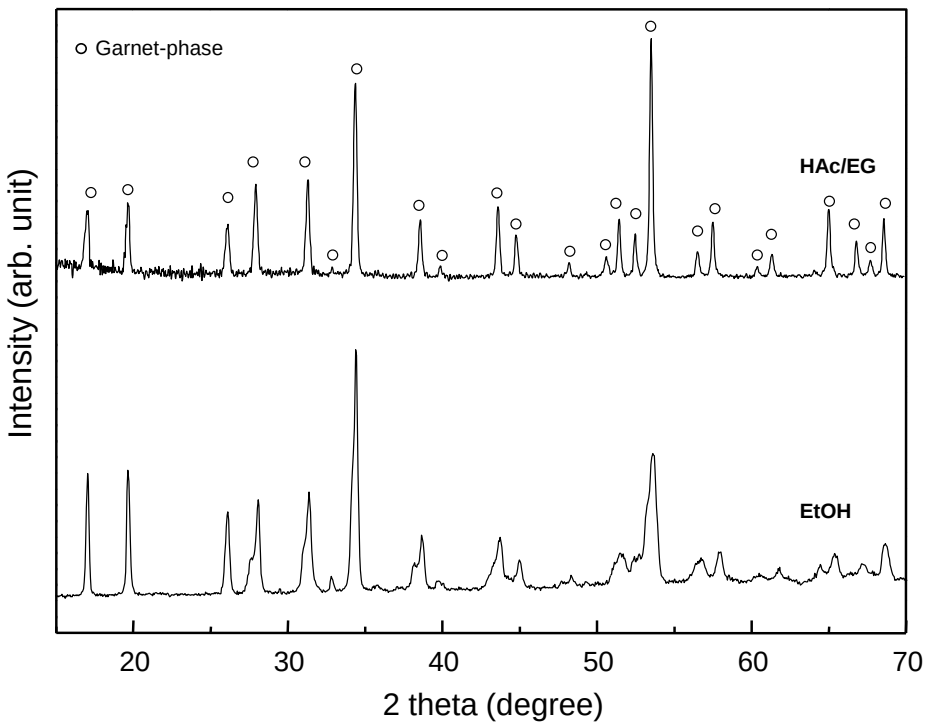

Figure 6.3. XRPD patterns of the PS template impregnated with LLTO precursors and calcined at 973 K for 1 hour.

6.3.4. Morphology of 3DOM LLTO

Figure 6.4 and 6.5 show several SEM images of 3DOM LLTO with various colloidal crystal templates sizes (1, 3, 5 μm) by addition of EtOH based or HAc&EG mixture based precursor solutions, respectively. All differently sized PS templates were very well aligned as discussed in section 3.1 in detail. As can be seen in figure 6.4a and 6.5a, starting with very well aligned 1 μm PS template is yielding very dense LLTO materials. This can be explained by the fact that the grains of the garnet compound are growing too fast and large so they destroy the interstitial space of the 1μm PS template, which further prevents the formation of the porous network. In addition to these, Gao et al. showed that the HAc/EG mixture based solutions first decompose to the $LiLa_2TaO_6$ phase with a crystal structure different than garnet at 923 K while above 973 K it is fully transformed into the garnet phase in the sol-gel synthesis of $Li_5La_3Ta_2O_{12}$

[21]. So the coalition and phase transformation to garnet compound of the intermediate phase above 923 K could lead agglomeration and result in large grains for garnet phase LLTO. For 3DOM garnet-type LLTO originating from 3 μm PS template, a higher porosity is observed as shown in figure 6.4b and 5b but there is some irregularity in the long range order and there are break downs in the network due to the shrinkage during calcinations. Significantly improved network formation is obtained with the 5 μm PS template compared to the other template sizes (figure 6.4c and 6.5c).

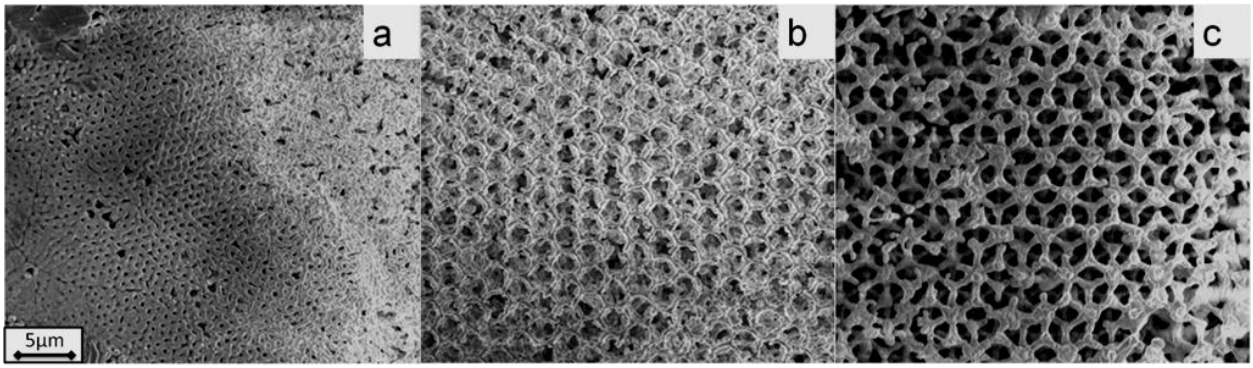

Figure 6.4. SEM image of 3DOM LLTO prepared using mono-dispersed PS templates **(a)** 1 μm, **(b)** 3 μm and **(c)** 5 μm combined with EtOH based precursor solution and annealed at 973 K for 1h.

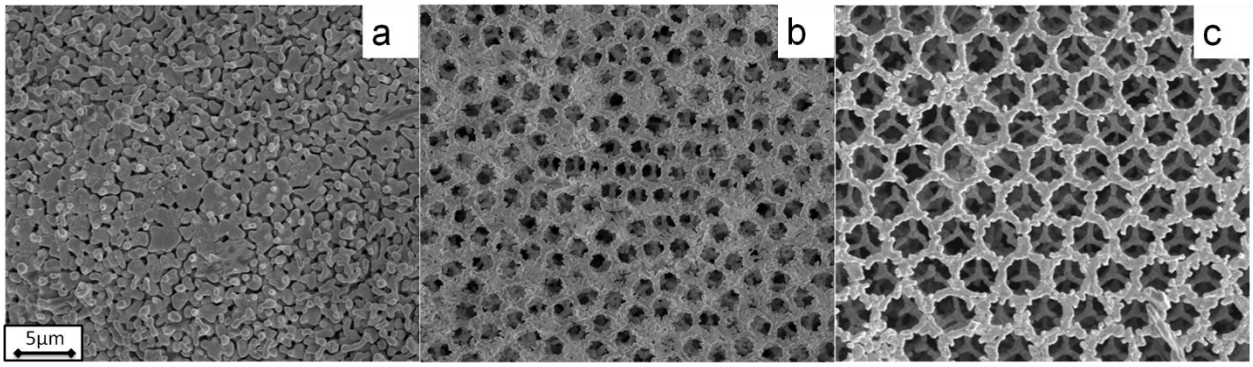

Figure 6.5. SEM image of 3DOM LLTO prepared using mono-dispersed PS templates **(a)** 1 μm, **(b)** 3 μm and **(c)** 5 μm combined with HAc/EG based precursor solution and annealed at 973 K for 1h.

Moreover, it can be clearly seen in figure 6.4c and 6.5c, that when HAc/EG mixture is used for the precursor solution the network formation is further improved compare to the EtOH based precursor. The alternating layers as well as the long range order were obtained with combination of 5μm PS template and HAc/EG based LLTO precursor solution (figure 6.6). In general, using a HAc/EG as solvent has a positive effect by increasing the grain size which enhances the interconnectivity of the network.

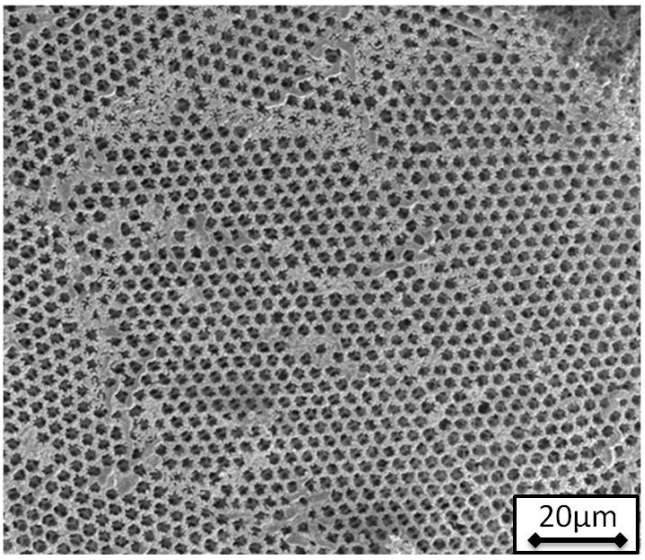

Figure 6.6. SEM image of 3DOM LLTO prepared using mono-dispersed 5 μm PS template combined with HAc/EG precursor solution and annealed at 973 K for 1h.

6.4. Conclusions

Three dimensionally ordered $Li_5La_3Ta_2O_{12}$ membranes with garnet-type structure were prepared by the colloidal crystal templating method using various sizes of mono-dispersed PS spheres, combined with two different sol-gel synthesis methods. Experiments were performed with both ethanol based LLTO precursor solutions as well as an acetic acid and ethylene glycol mixed-base solution. All of above mentioned different PS size templates yielded pure and crystalline garnet phase when they are annealed at 973 K. Using 1 μm mono-dispersed PS templates yielded an undesired dense LLTO membrane which is due to the large grains of the LLTO garnet phase.

Porous 3DOM LLTO membranes were obtained with 3μm spheres with absence of long range order and many defects. Our findings also showed that PS template with 5 μm beads is the optimum size for highly ordered and porous membranes. Further improvement in terms of long range order in network formation is also possible when the ethanol-based precursor solution is replaced with acetic acid and ethylene glycol mixture-based LLTO precursor solution. Unfortunately the mechanical properties of the 3DOM garnet-type LLTO membranes are poor and the membranes are very fragile which currently prevents us to perform the lithium ion conductivity measurements.

6.5. References

[1] P.H.L. Notten, F. Roozeboom, R.A.H. Niessen, L. Baggetto, Adv. Mater. **2007**, 19, 4564.

[2] L. Baggetto, R.A.H. Niessen, F. Roozeboom, P.H.L. Notten, Adv. Funct. Mater. **2008**, 19, 1057.

[3] M. Itoh, Y. Inaguma, W. Jung, L. Chen, T. Nakamura, Solid State Ionics **1994**, 70, 203.

[4] A. R. J. West, Appl. Electrochem. **1973**, 3, 327.

[5] A. Kvist, A. Lunden, Z. Naturforsch. **1965**, 20a, 235.

[6] H. Y.-P. Hong, Mater. Res. Bull. **1978**, 13, 117.

[7] H. Aono, N. Imanaka, G. Y. Adachi, Acc. Chem, Res. **1994**, 27, 265.

[8] G. Y. Adachi, N. Imanaka, H. Aono, Adv. Mater. **1996**, 8, 127.

[9] H. Aono, E. Sugimoto, Y. Sadaoka, N. Imanaka, G. Adachi, J. Electrochem. Soc. **1989**, 136, L590.

[10] G. C. Farrington, B. S. Dunn, J. L. Briant, Solid State Ionics **1981**, 3–4, 405.

[11] V. Thangadurai, H. Kaack, W. Weppner, J. Am. Ceram. Soc. **2003**, 86, 437.

[12] V. Thangadurai, W. Weppner, Adv. Funct. Mater. **2005**, 15, 107.

[13] V. Thangadurai, W. Weppner, J. Am. Ceram. Soc. **2005**, 88, 411.

[14] V. Thangadurai, W. Weppner, J. Power Sources **2005**, 142, 339.

[15] R. Mrugan, V. Thangadurai, W. Weppner, Angew. Chem. Int. Ed. **2007**, 46, 7778.

[16] J. Awaka, N. Kijima, H. Hayakawa, J. Akimoto, J. Solid State Chem. **2009**, 182, 2046.

[17] I. Kokal, M. Somer, P.H.L. Notten, H.T. Hintzen, Solid State Ionics **2011**, 185, 42.

[18] Y. X. Gao, X. P. Wang, W. G. Wang, Q. F. Fang, Solid State Ionics **2010**, 181, 33.

[19] K. Dokko, N. Akutagawa, Y. Isshiki, K. Hoshina, K. Kanamura, Solid State Ionics **2005**, 176, 2345.

[20] V. Thangadurai, W. Weppner, Ionics **2006**, 12, 81.

[21] Y.X. Gao, X.P. Wang, W.G. Wang, Q.F. Fang, Solid State Ionics **2010**, 181, 33.

Chapter 7.

3D Patterning of thin Films of Lithium Lanthanum Titanium Oxide by Soft Lithography

Abstract

Two different (line and pit) types of 3D patterned thin films of $Li_{0.35}La_{0.55}TiO_3$ (LLT) with perovskite-type structure were fabricated from precursor solution prepared using sol-gel synthesis method by a low-cost soft lithography technique on two different substrates, Si and Pt coated Si substrates. Micro molding was used to pattern thin films with subsequent drying and pyrolysis processes of precursor solution at elevated temperatures. The thermal evolution of the precursor solutions were investigated in detail by thermal analysis (TG/DTA) and the morphology of the obtained thin films were investigated by scanning electron microscopy (SEM) and atomic force microscopy (AFM) measurements based on the solution and substrate choice. To measure the ionic conductivity of the layers, special type of specimens were prepared by focused ion beam (FIB) lithography. The results of this study show that the LLT solid electrolyte for all-solid-state lithium ion batteries can easily be deposited in to the patterned and desired3D structure by soft lithography.

7.1. Introduction

Electronic devices play an important role in our daily life and rechargeable lithium ion batteries are widely used as power supplies in those devices [1]. However, the conventional rechargeable lithium ion batteries do have their shortcomings in terms of safety, cycle life and performance [2]. One of the important issues is the use of hazardous and flammable organic liquid electrolyte in lithium ion batteries which leads to safety problems such as leakage and risk of explosion [3]. In addition to safety problems, the liquid electrolyte reduces the cycle life of the battery due to the formation of a solid electrolyte interface (SEI) between the liquid electrolyte and the electrode material during charging/discharging cycles which blocks the lithium ion current and decreases the battery's performance [4-5].

Another shortcoming is related to the power and energy the battery can supply. If the electrode-electrolyte interface area is not large enough, an increase in the energy density would limit the power output of the battery due to charge transfer limitations. Regarding the safety and life time of lithium ion batteries, these can greatly be enhanced using solid electrolytes [6]. However, increasing the energy density and /or higher power output performance of the battery will require higher current densities, leading to a voltage drop. This voltage drop can be prevented by enlarging the electrode-electrolyte interface area which reduces the current density. Thus combining solid electrolyte with 3D architectures may provide a promising combination to improve the performance of lithium ion batteries [7].

There are several 3D structured solid-state lithium-ion battery designs, such as the honeycomb type, all-solid-state integrated array structures and 3D ordered macroporous structures (3DOM) [8-12] have been proposed and reported to enhance the interfacial area between the electrode and electrolyte as well as the performance of the solid-state battery. However, some of these approaches need several etching and

deposition steps and some of them are suffering from low mechanical properties. In this study, we demonstrate new and low-cost techniques to prepare 3D structures by soft lithography, micro-patterning of LLT electrolyte which is one of the best lithium ion conductors with a bulk conductivity of $\sigma = 10^{-3}$S/cm at room temperature [13]. The patterned thin films of LLT were fabricated from a precursor solution prepared by a modified-Pechini sol-gel method which was micro-molded with a relief-patterned PDMS on a bare Si or Pt-coated Si substrate and solidified at 353 K before removing the mould. The solidified patterned precursor film was pyrolized at 973 K for 1 hour in air atmosphere. The phase and elemental composition as well as morphology of the LLT patterns were determined by XRD, AFM and SEM-EDAX measurements. The possibility of obtaining 3D-patterned electrolyte thin films with micron scale precision may offer many interesting opportunities in all-solid-state lithium ion batteries especially when their application is combined with electrode depositions.

7.2. Experimental Methods

7.2.1. Preparation of Precursor Solution

$Li_{0.35}La_{0.55}TiO_3$ precursor solution was prepared by sol-gel synthesis. Lithium acetate (99.99 % Sigma Aldrich) and lanthanum acetate (Sigma Aldrich 99.99%) were dissolved in 10 ml of a 2-propanol (Sigma Aldrich) and water mixture 1:1 (v/v). Next, 2.5 gr of HAc was added as a chelating agent with a molar ratio of 1:5 with respect to total the metal ions, then stoichiometic amounts of Ti butoxide (99.99 %Sigma Aldrich) was added to the solution. The solution was heated up to 303 K and stirred well for two hours to obtain a clear solution. Then the precursor solution was separated into two batches. One batch was used for micro-molding experiments and the second batch solution was slowly evaporated and concentrated at 343 K until a yellowish transparent gel was obtained. The gel was then dried at 373 K for 12 hours in air to yield highly

reactive black precursor powders and it was ground well and calcined at temperatures 973 K for 5 hours in air atmosphere to obtain LLT polycrystalline powders.

7.2.2. Micro-molding Experiments

The PDMS stamps were fabricated by casting the PDMS polymer, a 10:1 (v/v) mixture of Sylgard silicone elastomer 184, and its curing agent over a relief master prepared by photolithography. The elastomer was degassed for 30 minutes at room temperature and cured at 338 K for 4 hours, then peeled gently from the master. In this way PDMS stamps with micro wells were obtained. The silicon (Si) and platinum coated silicon (Pt/Si) substrates were cleaned by immersing in EtOH and acetone 1:1 (v/v) mixture in sonar bath. A drop of LLT precursor solution was placed onto the Si or Pt coated Si substrate and the PDMS mold was pressed on to it (figure 7.1). The sample and mold were placed on a hot stage set at 323 K for 3 hours to allow the solvent to diffuse into the mold as described in previous studies [14]. After the film fabrication, the sample was subjected to a high-temperature treatment at 973 K in air atmosphere for 1 hour to degrade the polymer and to oxidize and crystallize the ceramic phase

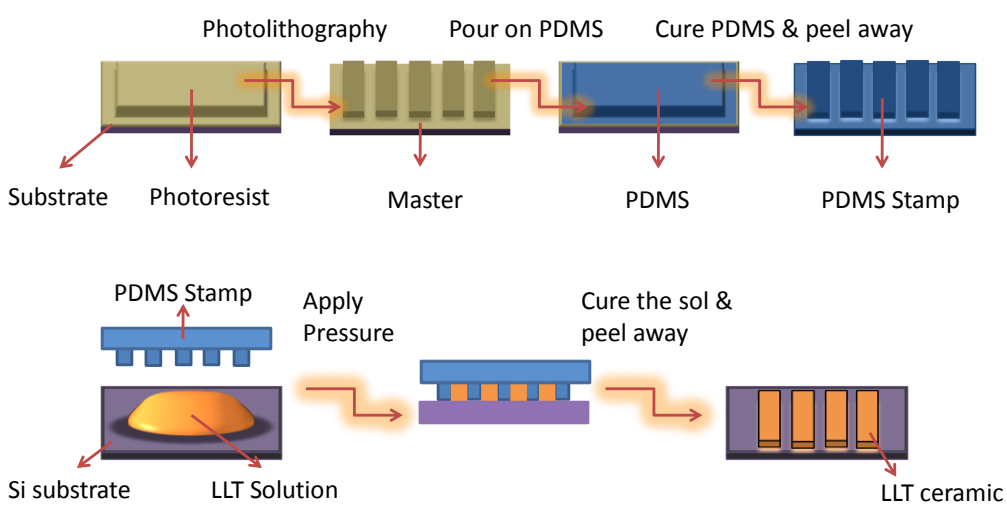

Figure 7.1. Schematic diagram of the micro-molding experiments used for the preparation of patterned thin films.

7.2.3. Characterization

Thermal analysis (TG/DTA) of the precursor solution dried at 373 K was conducted by using a Mettler Toledo TGA/SDTA 851 instrument. The thermal effects were investigated in 70 μl Al_2O_3 crucibles from 300 to 1273 K with a heating rate of 5 K/min in flowing air atmosphere (50 ml/min). Phase characterization of resulting compounds and patterned thin films were performed by X-ray powder diffraction (XRPD) analysis with a Bruker Enduar D4 diffractometer using CuK_α radiation at room temperature in the 2 theta ranges from 5° to 90° with a step size of 0.01° and counting time per step of 1 second. The morphology of the patterned LLT films were investigated by scanning electron microscopy using a Quanta 3D FEG instrument (FEI Company) and atomic force microscopy (AFM) using a Solver P47 of NT-MDT, Russia in a non-contact tapping mode with NT-MDT NSC11 cantilever at a resonant frequency of 155 KHz. Ionic conductivity measurements of polycrystalline powders were performed on double side gold coated pelletized sample with 12 mm diameter and 1 mm thickness at room temperature using a potentiostat with a frequency response analyzer (Ivium Stat) operating at 100 mV constant potential within the frequency range of 1 MHz to 5 Hz in air atmosphere.

7.3. Results and discussion

7.3.1. Thermal Analysis

Figure 7.2 illustrated the TG-DTA curves obtained from the dried powder precursor annealed in air, with a heating rate of 5 K min^{-1}, in the temperature range from 303 to 1373 K. According the TG signal, most of the weight loss (≈40%) was observed in the temperature range from 500 to 850 K within two steps. 40% weight loss, associated with an exothermic DTA peak which is due to the degradation of the polymer, converting the organic component into CO_2 and H_2O. At higher temperatures 850 K, chemical

reactions between the precursors occurs so there is no significant loss above 850 K. It also indicates that the precursor is fully transformed into oxide. XRPD results also confirmed that the sample annealed at 973 K crystallizes very well in the perovskite phase.

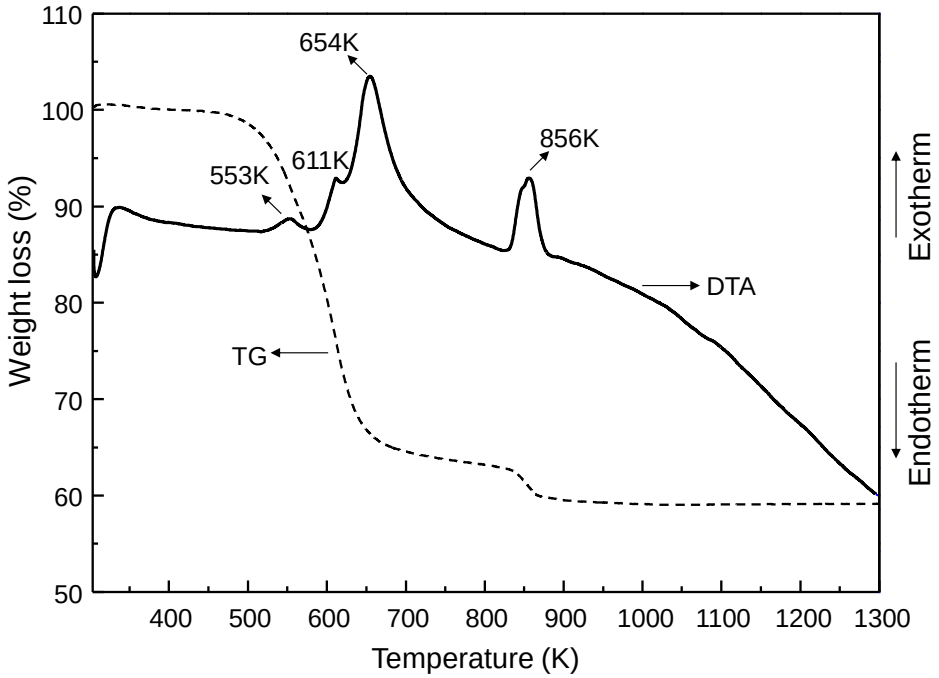

Figure 7.2. TG/DTA curves of the dried LLT precursor powder obtained by sol-gel method.

7.3.2. SEM/EDAX and AFM Characterization of LLT pattern films

The size of the pattern area of the PDMS stamps was 10x10 mm^2. Figure 7.3 shows a patterned film on silicon substrates, obtained with a stamping time of 3 hours. It can be seen from the image that almost the entire area of the stamp pattern is reproduced onto the substrate. During the patterning experiments a line and pit patterned mold was used to replicate the structures.

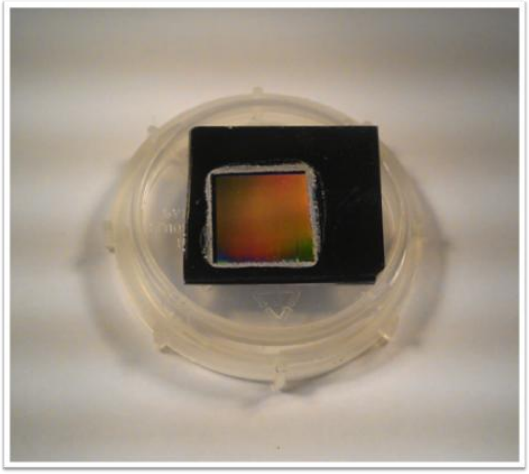

Figure 7.3. The patterned film (10 mm x 10 mm) on silicon substrates, obtained with a stamping time of 3 hours and annealed at 973 K for 1 hour.

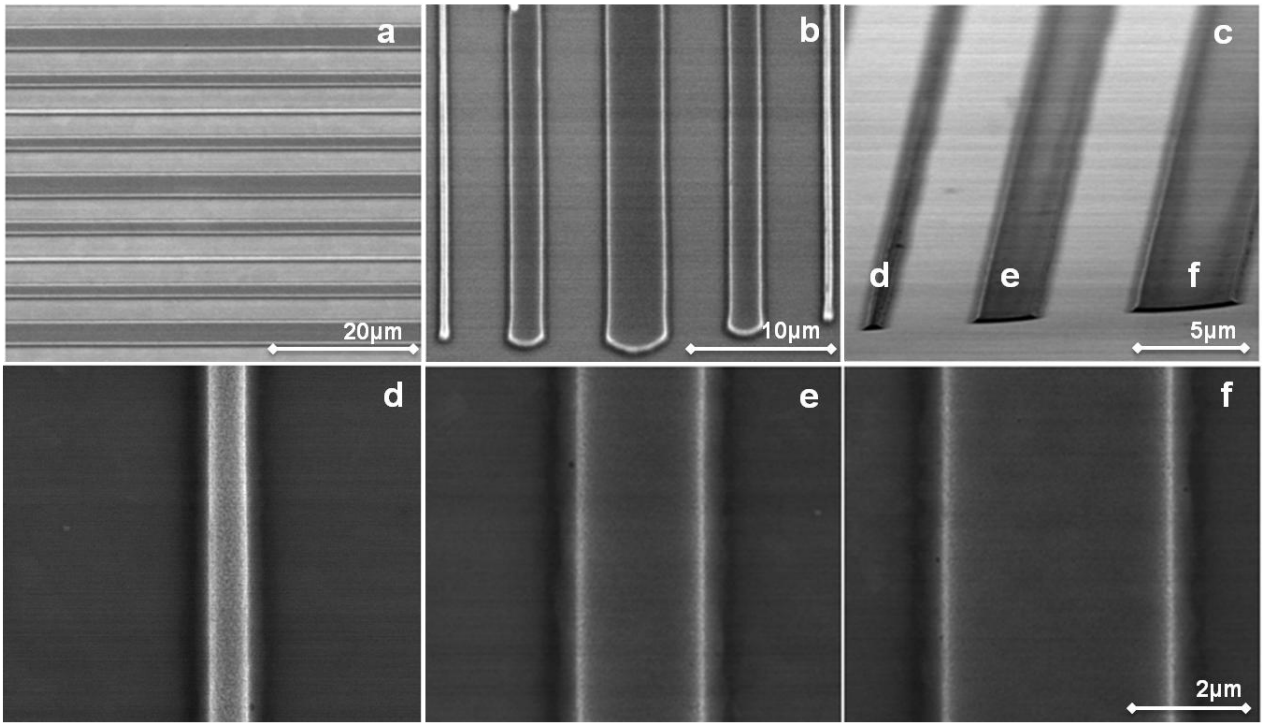

Figure 7.4. SEM images of line-patterned LLT. Horizontal view **(a)**, edges in vertical view **(b),** tilted view **(c)** individual zoomed view of lines with different thickness **(d)** 500 nm, **(e)** 2 µm, **(f)** 4 µm.

Figure 7.4 shows SEM images of the line patterns on Si substrate which are fully separated from each other, i.e. no residual layer of film material has spread between the lines. SEM images reveal that it is possible to pattern almost smaller than micron size straight line depending on the structure of the PDMS mold with a thickness of a few hundred nanometers (figure 7.4d).

We have also investigated the pit shape of the ceramic patterns on Si substrates. Figure 7.5 shows the top and tilted view SEM images of the pit patterns. The pit patterns have a pit-diameter (P_d) of 4 μm and a thickness around 500 nm as shown also in AFM height measurements (figure 7.6). The pit patterns as well as the line patterns do not contain any other residual film layer or unwanted structures on the substrate. This is also confirmed by EDAX mapping measurements.

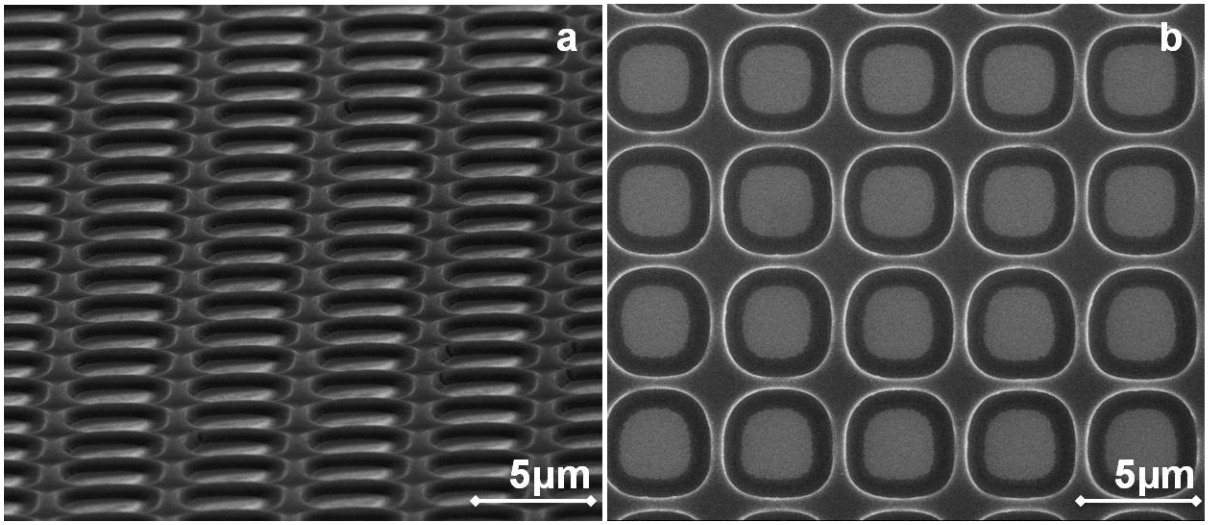

Figure 7.5. SEM images of the pit patterned LLT, tilted view **(a)**, top view **(b)**

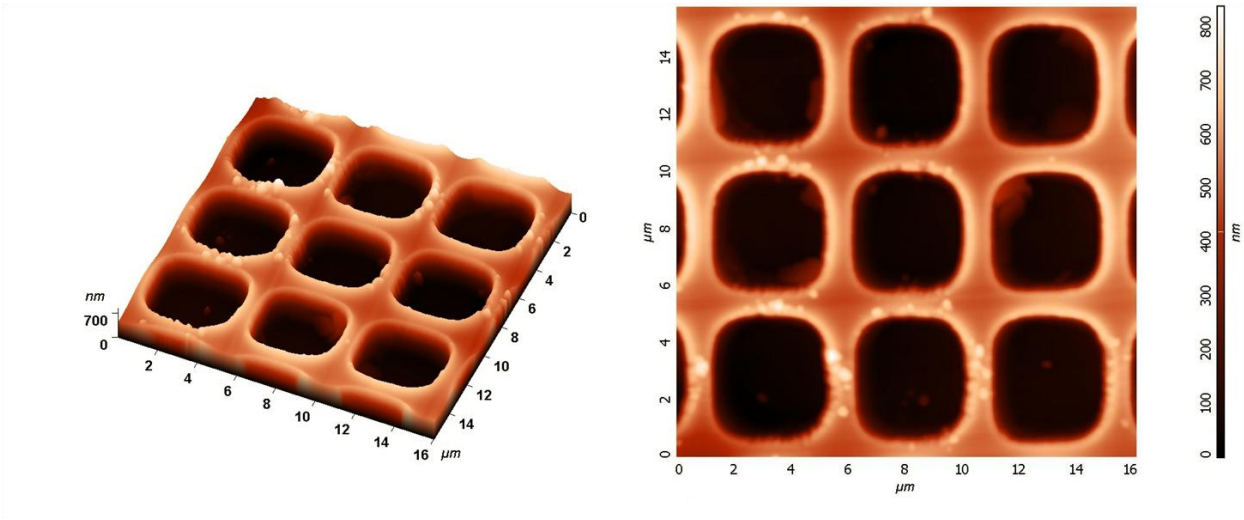

Figure 7.6. AFM images of the pit-patterned LLT, tilted view **(a)**, top view **(b)**

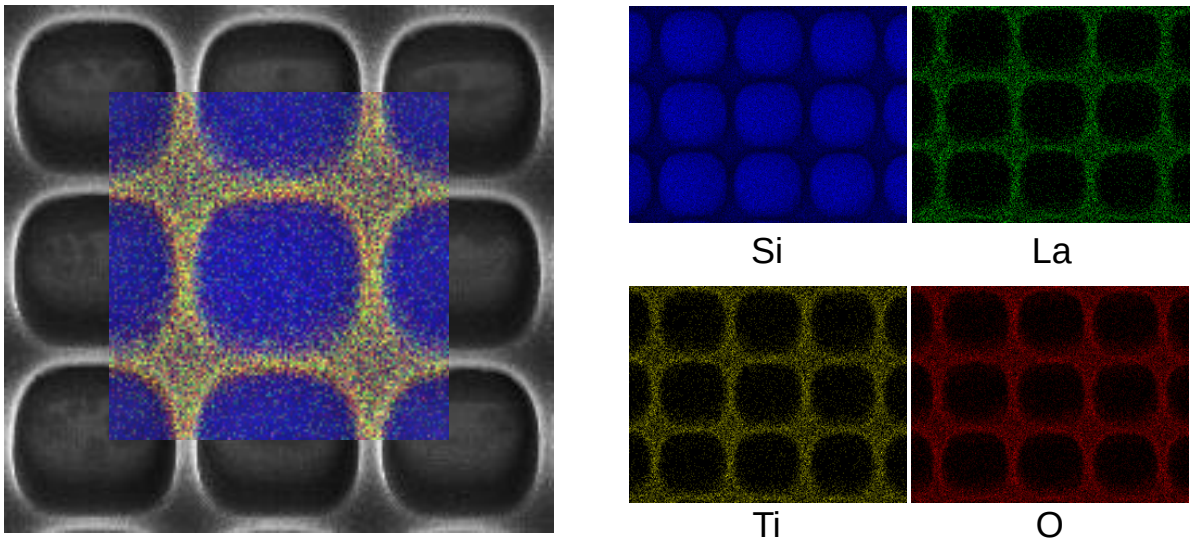

Figure 7.7. SEM image of pit patterned LLT with EDAX mapping overlay **(a)** and EDAX mapping of Si, La, Ti, O **(b)**

Figure 7.7 shows the Sem micrograph and EDAX mapping of pit patterns with the elemental mapping of Si, La, Ti and O. As can been from the Si signal, the bottom of the pit patterns gives only Si signal whereas, the pattern contains of La, Ti and O. Since lithium is below the detection limits of EDAX, the chemical composition of the patterns was calculated based on the La, Ti and O signal only and is calculated to have $Li_{0.29}La_{0.57}TiO_3$ as chemical composition. The overlap of the La, Ti, O and Si EDAX

mapping images is shown in the SEM picture of the pit pattern and shows that La, Ti and O are mainly concentrated in the 3D structure and strong Si (substrate) signal was mostly obtained from inside the structure.

We have also studied Pt-coated Si substrates to investigate the possibility of LLT deposition by micro molding on different substrates. Figure 7.8 shows the SEM pictures of patterned thin films on Pt-coated Si substrate. The pit patterns and line patterns can easily be identified with a pit diameter P_d of around 4μm and the line with a thickness of around 2 μm. In addition to the well structured patterns, residual layers are also formed inside the pit patterns and in between the lines. The residual layer may be the result of the different wetting properties of the solution in contact with the substrate. It is also possible that during the high temperature annealing, the Pt-layer on Si substrate decomposes and induces roughness. The contrast difference between the patterned layer and the residual layer in the SEM pictures suggests that, the residual layer has a different composition than the patterned layer.

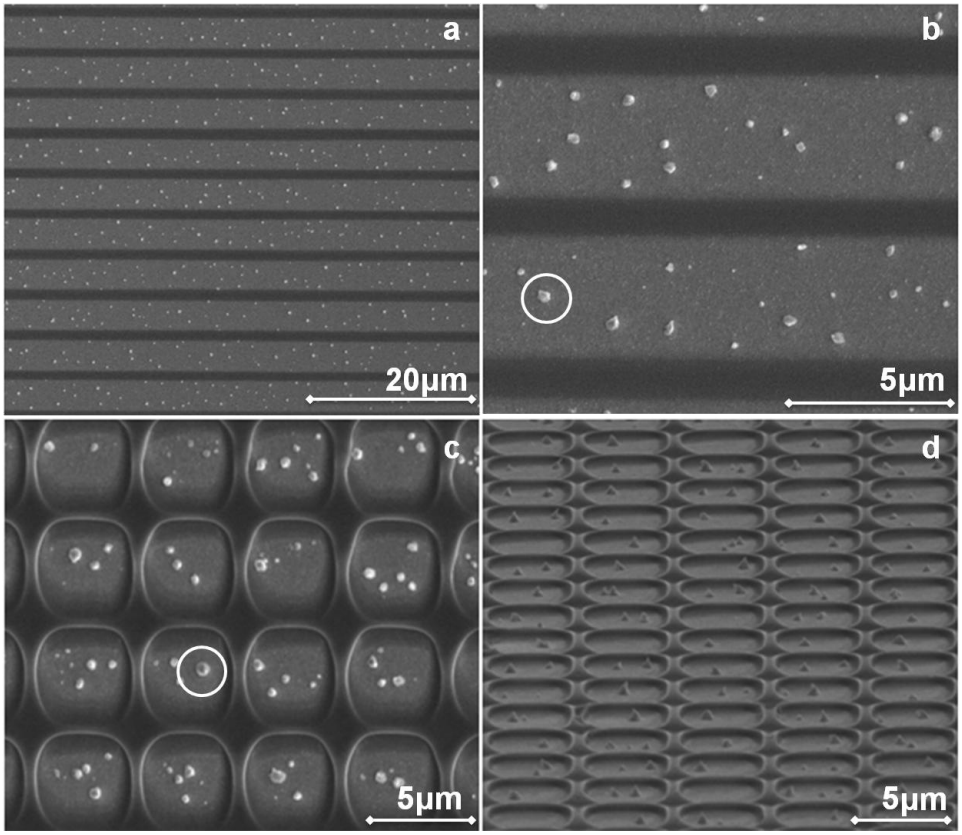

Figure 7.8. SEM images of line patterned LLT **(a-b)** and pit patterned LLT **(c)** top view and tilted view **(d)** on Pt deposited Si substrate. Residual layers are shown in circle.

7.3.3. XRPD Analysis

Figure 7.9a shows the XRPD of the dried precursor solution at 373 K for 12 hours and consequently annealed at 973 K for 5 hours in air atmosphere. The XRPD pattern matches well with perovskite type tetragonal (*P*4/ *mmm*) $Li_{0.35}La_{0.55}TiO_3$ without revealing any other minor reflections. The lattice constants are calculated by indexing the reflections and are a = 3.910(4) Å and c = 3.902(5) Å. So it can be concluded that a single phase perovskite compound can easily be obtained starting with a sol-gel precursor solution at relatively low temperatures compared to conventional solid-state reactions. Figure 7.9b shows the XRD pattern of the patterned thin film on Si substrate by soft lithography using the same precursor solution and annealed at 973 K for just 1 hour. A strong Si (004) reflection was observed at around two theta 70°. The strongest

perovskite peak at around 32° and the remaining reflections matches well with the perovskite phase.

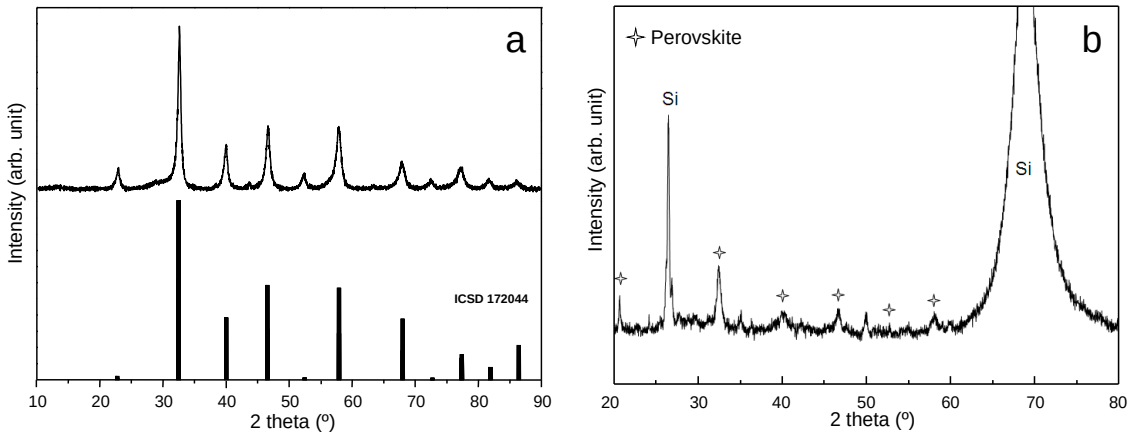

Figure 7.9. X-Ray powder diffraction pattern of annealed precursor at 973 K for 5 h in air atmosphere **(a)** and X-ray diffraction of Si(001) substrate with LLT micro patterned films **(b)**.

7.3.4. Ionic Conductivity

A typical impedance plot of a pellet composed of LLT, synthesized at 973 K by sol-gel synthesis and contacted with Au electrodes from both sides is shown in figure 7.10. It shows one compressed semicircle at high frequencies indicating a combination of the resistance of both bulk and grain boundary contribution and a tail at low frequencies. Such a tail is characteristic for a blocking of ionic charge carriers at the electrode-sample interface.

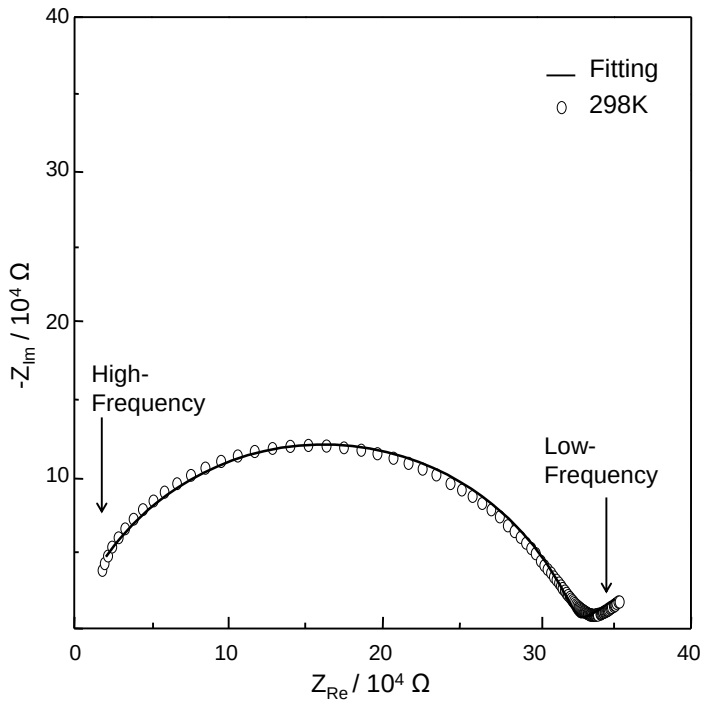

Figure 7.10. Nyquist plot (1MHz – 5Hz) of LLT prepared by sol-gel synthesis at 298 K using lithium ion blocking Au electrodes. The solid line was fitted with an equivalent circuit consisting of a resistance-capacitance contribution of the solid electrolyte and a capacitance contribution of the electrode ($R_{tot}Q_{tot}$)(Q_{el}) by the Ivium Equivalent Circuit Analyzer.

The impedance spectrum was resolved using an equivalent circuit ($R_{tot}Q_{tot}$)(Q_{el}) model where R is the resistance, Q the constant phase element and the subscripts "tot" and "el" refer the total and electrode, respectively. The lithium ionic conductivity properties of the specimen was evaluated by using the total (bulk plus grain boundary) Li-ion conductivity which is calculated to be $\sigma_{total} = 2.68 \times 10^{-6}$ Scm^{-1} at 298 K. This is lower than those reported for samples prepared by conventional solid-state synthesis ($\sigma_{total} = 2 \times 10^{-5}$ Scm^{-1} at 298 K) [15]. This slightly lower ionic conductivity in LLT synthesized by sol-gel synthesis compared to the conventional solid-state case could be explained to cation ordering in the crystal structure which can be tuned by the temperature program. In the literature, the samples prepared by the solid-state synthesis method were annealed above 1423 K combined with cooling down rapidly by quenching method to obtain

disordered material with high lithium ion conductivity [16]. The samples in this study prepared by sol-gel synthesis were prepared at 450 K lower temperature without any quenching step.

We have also prepared samples for the ionic conductivity measurements of patterned layers. Instead of sandwiching the ceramic electrolyte horizontally in between Li ion blocking layers (i.e Pt, Au), the platinum deposition was performed on the line patterns to sandwich the line vertically by Focused Ion Beam lithography (FIB) as shown in figure 7.11.

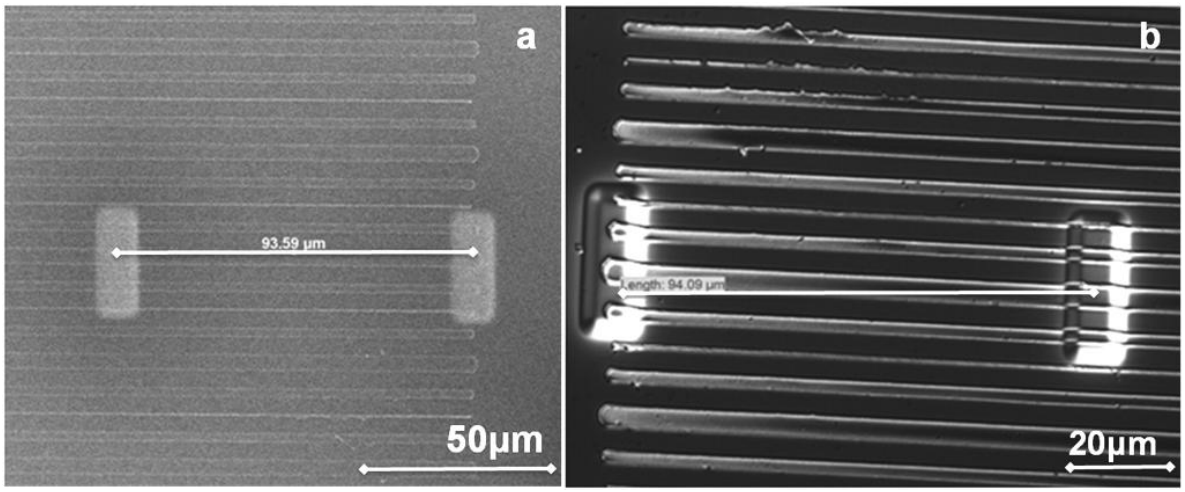

Figure 7.11 SEM **(a)** and optical images **(b)** of deposited Pt line as an ion blocking electrode by FIB top of a line patterned LLT on Si substrate.

However, all the attempts to measure the ionic conductivity of LLT pattern has failed due to a wire connection problem to the deposited electrode. Even though the impedance measurements have failed, the preparation of the specimen is promising and unique but it needs to be improved in such a way to enable us the proper connection between the electrodes and the probe.

7.4. Conclusions

Polycrystalline powders of perovskite type LLT have been successfully prepared at 973 K by a modified sol-gel preparation method. The crystal structure of the obtained powders was characterized by XRD. The powders have crystallized in a tetragonal symmetry (P4/mmm) with unit cell parameters: a = 3.910(4) Å and c = 3.902(5) Å. These are in good agreement with the previously reported results [17]. The ionic conductivity of the obtained powders was 2.68 x 10^{-6} Scm^{-1} at 298 K which is lower than previously reported results. The significant achievement was obtained in the micro molding experiments. For the first time ceramic electrolyte materials were deposited with 3 dimensional structures starting with simple sol-gel synthesis combined with micro molding experiments by soft lithography. We have performed micro molding experiments on two different substrates (Si and Pt coated Si). Deposition on Si substrate results remarkably good results. The pit patterns as well as the line patterns do not contain any other residual film layer or unwanted structures on the substrate as can be seen in the SEM images and EDAX mapping measurements. By EDAX mapping measurements, the chemical composition of ceramic was determined to be $Li_{0.29}La_{0.57}TiO_3$. The samples for ionic conductivity measurements were prepared by vertical deposition of Pt electrodes on horizontal line patterns by FIB lithography. The sample preparation was achieved with desired structure, unfortunately due to the misconnection of contact between the Pt electrode and the measurements probes, the measurements could not be performed. Pt-coated Si substrates were also studied due to their wide use in micro-battery applications and also their suitability for ionic conductivity measurements. Unfortunately, the deposition experiments resulted with unwanted residual layers in both line and pit pattern deposition experiments.

In conclusion, the thin-film LLT deposition with desired 3-dimensional structures on Si substrate has been achieved by micro molding experiments. We believe, these

promising results may open up a new approach for the preparation of fully integrated 3-dimensional all-solid-state micro-batteries in the near future.

7.5. References

[1] J.-M. Tarascon, M. Armand, Nature **2001**, 414, 359.

[2] L. Baggetto, R. A. H. Nissen, F. Roozeboom, P.H.L. Notten, Adv. Funct. Mater. **2008**, 18, 1057.

[3] V. Thangadurai, W. Weppner, Ionics **2006,** 12, 81.

[4]J. Vetter, P. Novak, M.R. Wagner, C. Veit, K. C. Moller, J. O. Besenhard, M. Winter, M. Wohlfahrt-Mehrens, C. Vogler, A. Hammouche, J. Powder Soruces **2005**, 147, 269.

[5] L. Baggetto, J.F.M Oudenhoven, T. van Dongen, J.H. Klootwijk, M. Mulder, R.A.H. Niessen, M.H.J.M. de Croon, P.H.L. Notten, J. Power Sources **2009,** 189, 402.

[6] N. Kamaya, K. Homma, Y. Yamakawa, M. Hirayama, R. Kanno, M. Yonemura, T. Kamiyama, Y. Kato, S. Hama, K. Kawamoto, A. Mitsui, Nature Materials 10 (2011) 682.

[7] J. W. Long, B. Dunn, D. R. Rolison, H. S. White, Chem. Rev. **2004**, 104, 4463.

[8] L. Baggetto, D. Danilov, P.H.L. Notten, Adv. Mater. **2011**, 23, 1563.

[9] P. H. L. Notten, F. Roozeboom, R. A. H. Niessen, L. Baggetto, Adv. Mater. **2007**, 19, 4564.

[10] L. Baggetto, H.C.M. Knoops, R. A. H. Niessen, W. M. M. Kessels, P.H.L. Notten, J. Mater. Chem. **2010**, 20, 3703.

[11] K. Kanamura, N. Akutagawa, K. Dokko, J. Power Sources, **2005**, 146, 86.

[12] I. Kokal, E.J. van den Ham, A. C. A Delsing, P. H. L. Notten, H.T. Hintzen [13] M. Itoh, Y. Inaguma, W. Jung, L. Chen, T. Nakamura, Solid State Ionics **1994**, 70, 196.

[14]O. F. Gobel, M. Nedelcu, U. Steiner, Adv. Func. Mater. **2007**, 17, 1131

[15] Y. Inaguma, L. Chen, M. Itoh, T. Nakamura, T. Uchida, M. Ikuta, M. Wakihara, Solid State Commun. **1993**, 86, 689.

[16] Y. Harada, Y. Hirakoso, H. Kawai, J. Kuwano, Solid State Ionics, **1999**, 121, 245.

[17] M. Sommariva, M. Catti, Chem. Mater. **2006**, 18, 2411.

Summary

The focus of this Ph.D. thesis is to understand the lithium ion motion and to enhance the Li-ionic conductivities in commonly known solid-state lithium ion conductors by changing the structural properties and preparation methods. In addition, the feasibility for practical utilization of several studied solid electrolyte materials in 3D all-solid-state lithium ion batteries was investigated.

Several inorganic compounds with high ionic conductivity for all-solid-state lithium ion batteries have been proposed in recent literatures. These are discussed in Chapter 2 in terms of the relationship with the structural features and the lithium ion mobility. The key criteria of high lithium ion mobility in any solid lithium ion conductor are the concentration of the charge carriers and vacancies, the "bottleneck size" which is the cross sectional area that lithium ion has to pass through, the connectivity of the sites where lithium ions are mobile and the polarizability of the anions.

Based on the structural features, the very well known $Li_{0.50}L_{0.50}TiO_3$ (LLT) compound with perovskite-type structure was modified to increase the bottleneck size by anionic substitution of oxygen by the relatively larger anion, nitrogen, in Chapter 3. The resulting oxynitride compound contains 0.58 atoms of nitrogen in the formula unit and has a higher lattice volume up to 4.4 %. Although it is expected that lithium ions can move more easily in this structure, impedance measurements show that the ionic conductivity is decreasing with increase in nitrogen content. This has been explained by the distortion in TiO_6 polyhedra which is slowing down the lithium ion motion. In addition we observed anionic vacancies which are also changing the chemical environment of the lithium. The anionic vacancies which are formed during the substitution can be prevented by cationic substitution of Ti^{4+} with Ta^{5+} to combine with

anionic substitution in oxygen positions. This type of approach will not only prevent anionic vacancies but will also increase the electro chemical stability of this compound towards possible reduction when in contact with lithium.

$Li_7La_3Zr_2O_{12}$ (LLZO) with garnet type structure has recently become of high interest due to its potential as a solid-state lithium ion conductor. It has a high ionic conductivity (10^{-4} S/cm for the cubic phase at room temperature) as well as a good stability against lithium and moisture. However, LLZO crystallizes in three different phases; low and high temperature cubic and tetragonal. The high temperature cubic phase is preferred because it has a 2 orders of magnitude higher ionic conductivity than the tetragonal phase whereas the synthesis of the cubic phase needs a high calcination temperature which makes it difficult to control the stoichiometry. Recently it has also been found that due to the high calcination temperature, the aluminum contamination from the reaction crucible (Al_2O_3) enables and stabilizes the cubic phase formation. To have a better control on the chemical composition and prevent contamination, low temperature synthesis by a sol-gel method was investigated in Chapter 4. The tetragonal phase was successfully synthesized at 1073 K. This is 200 K lower than any previously reported results and a new low temperature (973 K) cubic phase was reported for the first time. The ionic conductivities of the tetragonal phase were determined and to be in the same order of magnitude with those of the materials synthesized by conventional solid-state synthesis. Unfortunately, the ionic conductivity of the new cubic phase could not be determined due to the temperature limitation during the densification process which leads porous specimens.

$Li_5La_3Ta_2O_{12}$ (LLTO) and $Li_6BaLa_2Ta_2O_{12}$ (LLBTO) with garnet type structure are yet other promising candidates as solid lithium ion conductors. They are chemically stabile against lithium and moisture due to the presence of Ta^{5+} in the garnet compound series. LLTO has a lithium ionic conductivity of 10^{-6} S/cm, whereas LLBTO exhibits a conductivity of 10^{-5} S/cm at room temperature due to its larger unit cell and higher

lithium ion concentration. The sol-gel synthesis of garnet compounds was investigated in Chapter 5. It is found that nano-sized compounds have better sintering ability and the ionic conductivities are found in the same order magnitude with a slightly increase compared to the compounds synthesized by conventional solid-state methods. The sol-gel synthesis of garnet compounds opened up a new approach in the preparation of solid-state lithium ion conductors with 3D structure. This is discussed in detail in Chapter 6 for the preparation of 3 dimensional ordered macraporous (3DOM) materials. LLTO was investigated for 3DOM material preparation experiments due to the relatively lower synthesis temperature resulting in smaller grain sized compounds compared to other members of garnet compounds. 3DOM membranes of $Li_5La_3Ta_2O_{12}$ (LLTO) for all-solid-state lithium ion batteries were prepared by using colloidal crystal templating of mono dispersed polystyrene (PS) spheres combined with sol-gel synthesis of LLTO precursor. Two different types of solvent (EtOH and HAc/EG) and 3 different sizes of PS spheres (1, 3 and 5 μm) were used for the preparation of 3DOM membranes. The effect of the solvent type and the PS sphere size on the morphology of the 3DOM membranes was investigated. Our investigations show that using a HAc/EG based solution with the template prepared by using 5 μm PS spheres results in the most interconnected and long range ordered membranes. The 3DOM membranes can be used to fabricate all-solid-state lithium ion batteries using a "sandwich structure" which is composed of a dense LLTO layer having the 3DOM layer on both sides. Then by immersing the electrode material in the pores of the 3DOM layer, the all-solid-state battery can easily be fabricated.

As an alternative 3D structuring method, nano printing by soft lithography is described in Chapter 7. The sol-gel synthesis of $Li_{0.29}La_{0.54}TiO_3$ (LLT) with perovskite structure and its patterning by soft lithography was studied. A 3D patterned LLT structure was obtained in the micro molding experiments and for the first time ceramic electrolyte materials were deposited with 3 dimensional structures (line and pit patterns) starting

with simple sol-gel synthesis were combined with micro molding experiments by soft lithography. The patterning experiments conducted on Si substrates and\or Pt coated Si substrate. The Si substrate was found to be more suitable and yielded better patterns compared to Pt coated Si substrate because the deposition performed on Pt coated Si substrate yielded unwanted residual layers in both line and pit pattern deposition experiments. This may be explained due to the wetting properties of the Pt surface and the durability of Pt coated Si substrates at 973 K. AFM and SEM measurements were done to investigate the morphology of the patterns deposited by soft lithography and it shows that by using the different type of mold it is possible to replicate the desired structure.

In conclusion, sol-gel synthesis is a successful method to prepare various lithium-ion battery electrolyte materials at low temperature and it makes use of inexpensive precursors of metal salts (nitrates, acetates or oxides) combined with metal alkoxides. Using sol-gel precursor solutions, we demonstrated the successful preparation of 3D structured electrolyte materials by soft lithography and crystal templating for 3D all solid-state lithium ion batteries. We found that the soft lithography is a very accurate technique (sub-micrometer precision) and it can easily be applicable to larger scales. In contrast, the accuracy and the applicability of crystal templating is dependent on the template sphere size and the precursor material.

As a follow up research, the studied preparation techniques (such as crystal templating and micro patterning) can be combined with impregnation of the electrode material by previously investigated deposition techniques such as; spin-coating, atomic layer deposition (ALD) or chemical vapor deposition (CVD). The micro patterning experiments can easily be used for any type of material which can be prepared by sol-gel synthesis. Since the sol-gel synthesis of active electrode materials was established in literature, 3D all-solid-state lithium-ion battery can be easily prepared by deposition of different array of compounds separately on the same substrate. It is also possible with

non-oxidic compounds which could be generated by changing from an air atmosphere to different (N_2, NH_3, H_2, etc.) atmospheres during the high-temperature step of the synthesis. Overall, the combination of rather low tech and low-cost processes (sol-gel combined with soft-lithography or crystal templating) using simple starting materials and equipment (vacuum pump and heater plate) makes it possible to create sub-micrometer structures of electrolyte materials in the normal lab environment. It is likely that this manufacturing route can be applied to various other battery materials as well as large scales.

Curriculum Vitae

Ilkin Kokal was born on 28-08-1983 in Balikesir, Turkey. After finishing secondary education in 2001 at Sirri Yircali Anadolu Lisesi in Balikesir, he obtained B.Sc. degree in Chemistry at Koc University, Istanbul in 2006. He completed his master's program in the same university on Material Science and Engineering in 2008. During his master research, he studied on Novel Nitrido Borates: Synthesis, Crystal structure and Physical Properties under the supervision of prof. dr. Mehmet Somer. In October 2008, he started a PhD project at Energy Materials and Devices group in Eindhoven University of Technology, The Netherlands under the supervision of prof. dr. Peter Notten. The results obtained during this period are presented in this dissertation. The PhD. position was funded by STW within the project "Second Generation of Integrated Batteries" (07796)

List of Publications

S.S. Ozturk, **I. Kokal**, M. Somer, Z. Kristallogr. NSC **2005**, 220, 303.

M. Somer, S. Acar, C. Koz, **I. Kokal**, P. Höhn, R. Cardoso-Gil, U. Aydemir, L. Akselrud, Journal of Alloys and Compounds. **2009**, 491, 98.

P. Höhn, Y. Prots, **I. Kokal**, M. Somer, Z. Kristallogr. NSC **2009,** 224, 379.

I. Kokal, M. Somer, L. Akselrud, P. Höhn, W. Carillo-Cabrera, Z. Anorg. Allg. Chem. **2011**, 637, 8, 915.

I. Kokal, Y. Prots, U. Aydemir, W. Schnelle, L. Akselrud, P. Höhn, M. Somer, Z. Kristallogr. **2011**, 226, 633.

I. Kokal, M. Somer, P.H.L. Notten, H. T. Hintzen, Solid State Ionics. **2011**, 185, 42.

I. Kokal, K.V. Ramanujachary, P.H.L. Notten, H. T. Hintzen, Materials Research Bulletin **2012**, 47, 1932.

S.Celebi, **I. Kokal**, T.A. Nijhuis, J. van der Schaaf, F.A. Bruijn, J.C. Schouten App. Catal. A: Gen **2012**, submitted/in press.

(to be) submitted

I. Kokal, J. van Ham, P.H.L. Notten, H. T. Hintzen "3D ordered Macraporous $Li_5La_3Ta_2O_{12}$ with garnet type structure for all solid state batteries"

I. Kokal, B. Karabiyik, M. Somer, P.H.L. Notten, H. T. Hintzen "Sol-gel synthesis and Photoluminescence properties of Eu^{3+} activated garnet-type $Li_6La_2BaTa_2O_{12}$".

I. Kokal, O.F. Göbel, J.E. ten Elshof, P.H.L Notten, H.T. Hintzen "3D Patterning of thin Films of Lithium Lanthanum Titanium Oxide by Soft Lithography" (in preparation).

Acknowledgements

First and foremost, I would like to start with thanking my supervisor Peter H. L. Notten for giving me the opportunity to perform my PhD study. I have learned and achieved more than I ever dreamed by his precious guiding and help. I also would like thank my co-supervisor Bert Hintzen for helping me to find my way and fruitful scientific discussions.

Particular thanks are given to Prof. Somer, Prof. Ramanujachary, Prof. ten Elshof and Dr. Gobel for their nice collaboration. It was honor for me to work together with you. I also would like to thank the core committee members Prof. Van Bael and Prof. Roozeboom for their valuable comments.

I would like to thank all the members of SKE for their support and friendship. Obviously, my office mates and life-long friends Kamil Kiraz and Thiru are very well acknowledged for their awesomeness.

Friends were also supportive during my stay in Netherlands. Since I have infinitely many Turkish friends in Eindhoven, I just would like to thank them all for their valuable friendship and for all the fun and good time we shared together.
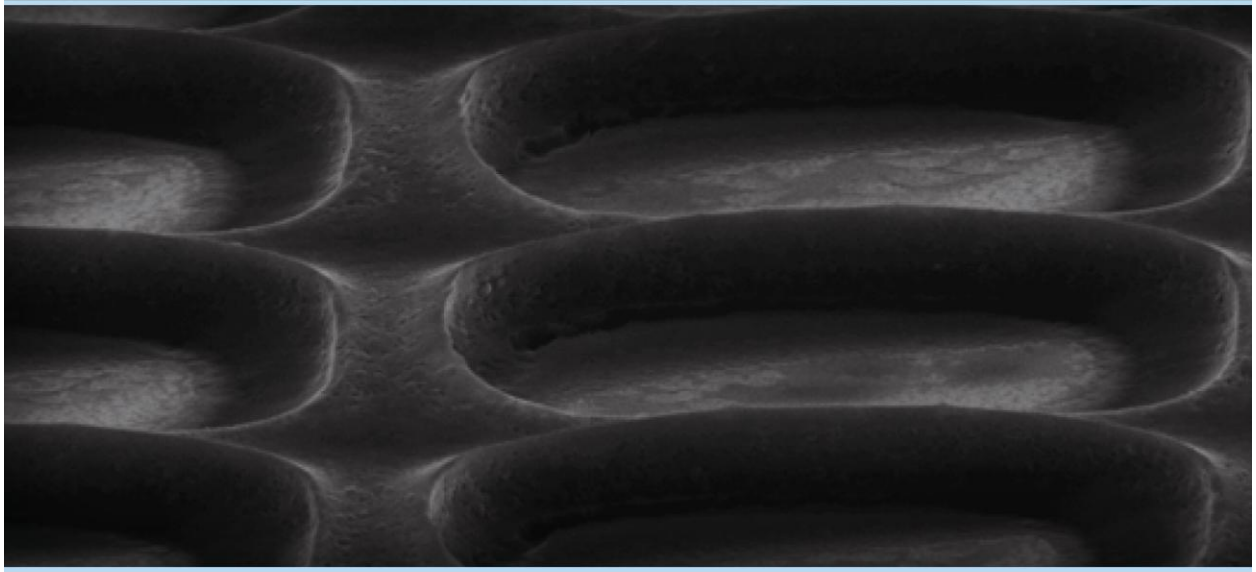
The last but not least, I thank my parents, my sister and my wife for believing in me and trusting me at every step I have taken so far. I am very lucky to be part of such a wonderful family.